

Contributions to the Development of Novel Thermoelectric Materials and Systems

Dissertation

Benjamin Geppert

Contributions to the Development of Novel Thermoelectric Materials and Systems

VON DER NATURWISSENSCHAFTLICHEN FAKULTÄT
DER GOTTFRIED WILHELM LEIBNIZ UNIVERSITÄT HANNOVER

ZUR ERLANGUNG DES GRADES

Doktor der Naturwissenschaften
(Dr. rer. nat.)

genehmigte Dissertation

von

Benjamin Geppert, M. Sc.

geboren am 29.07.1985

2017

Referent: Prof. Dr. rer. nat. Armin Feldhoff

Korreferent: Prof. Dr. rer. nat. Jürgen Caro

Tag der Promotion: 14.02.2017

Preface

The presented results were carried out during my doctoral studies during which I was employed as scientific assistant at the Institute of Physical Chemistry and Electrochemistry at the Gottfried Wilhelm Leibniz Universität Hannover under the supervision of Prof. Dr. Armin Feldhoff.

Six research articles are represented within this thesis. The measurements as well as data interpretation were done by myself, except one article, that was prepared by M. Sc. Michael Bittner (section 3.2). Prof. Dr. Armin Feldhoff taught me the art of manuscript preparation. The manuscripts were prepared by myself with great help of my supervisor. Furthermore I acknowledge helpful discussions from M. Sc. Michael Bittner. In the last three years he and myself developed measurement setups for thermoelectric material and generator characterisation.

The first two articles comprehend the synthesis and characterisation of novel oxide-based thermoelectric composite materials. The article *Experimental and theoretical thermoelectric investigations of n-type composite oxide materials* contains the investigations of an n-type Zincite-Perovskite composite material and the theoretical descriptions for thermoelectric coupling of composite materials. The resulting equations were validated by thermoelectric characterisation and X-ray diffraction measurements for determination of fractional compositions. In the second article, *Enhanced flexible thermoelectric generators based on oxide-metal composite materials*, oxide-metal composites were synthesised. P-type $\text{Ca}_3\text{Co}_4\text{O}_9$ -based composite materials were synthesised, characterised and applied in flexible thermoelectric generators. The results of those investigations were interpreted in the framework of the postulations published by Dario Narducci. In terms of thermoelectric material modification the role of the heat conductivity is contradictory. It is all about the decision of creating materials with high thermoelectric conversion efficiency or high electrical power output.

Chapter 3 represents two articles that comprehend the application of thermoelectric materials in generators. The rigid design with chess board geometry exhibited advantageous properties for high temperature application. In the article *Oxide – Based Thermoelectric Generator for High – Temperature Application Using p – Type $\text{Ca}_3\text{Co}_4\text{O}_9$ and n – Type $\text{In}_{1.95}\text{Sn}_{0.05}\text{O}_3$ Legs* such a generator is presented. The article *An Approach to Flexible Thermoelectric Generator Fabricated Using Bulk Materials* presents flexible thermoelectric generator stripes that were constructed with bulk materials. In contrast to the state of the art elaborated techniques as sputtering or printing were avoided. However, mechanical flexibility and stability are provided by those devices.

Furthermore, finite-element simulations (FEM) were performed in order to develop a tool to predict the performance of thermoelectric generators and to get a closer view into the distributions of determining quantities inside the generator's materials. At this point I have to thank Dennis Groeneveld who was involved in the development of the simulation tool during his bachelor thesis. The article *Finite-Element Simulations of a Thermoelectric Generator and Their Experimental Validation* presents the experimental validation of the tool using a commercial Bi-Sb-Te-based device. The script-based FEM tool was applied to a home-made thermoelectric generator that is presented in the article *Experimental Characterisation and Finite – Element Simulations of a Thermoelectric Generator with Ceramic p – type $\text{Ca}_3\text{Co}_4\text{O}_{10}$ and Metallic n – type $\text{Cu}_{0.57}\text{Ni}_{0.42}\text{Mn}_{0.01}$ Legs*.

Acknowledgment

First, I would like to express my thanks to my main supervisor Prof. Dr. Armin Feldhoff. He was always supporting the investigations with his great expertise in terms of electron microscopic research. We had fruitful discussions related to practical and to theoretical contents related to the field of termoelectricity. I am grateful for receiving the opportunity to work on the field of solid state chemistry and physics, especially related to the transport properties of oxide-based materials in the framework of thermoelectric research. Furthermore, I am grateful to Prof. Dr. Jürgen Caro, who has provided scientific knowledge and great working conditions for all Ph.D. students in the working group.

Furthermore, I want to express my thanks to my colleagues M. Sc. Michael Bittner and B. Sc. Dennis Groeneveld. I thank Prof. Dr. Alexander Korotkov and Dr. Vera Loboda for cooperation in the framework of the DAAD-partnership (St. Petersburg-Hannover). I also want to express my thanks to M. Sc. Sebastian Friebe for the possibility to support him with electronic measurement setup during his gas-separation investigations.

Additionally I give special thanks to my mother Birgit Geppert, my brother Julian Geppert and my aunt Monica Riechers, who always supported me in general matter of life.

Abstract

The thermoelectric effect leads to the possibility to construct energy conversion systems, that convert directly heat to electricity. They are handy (or even portable), free of movable mechanics, noiseless and maintenance free. The field of research is highly interdisciplinary and ranges from solid state chemistry for material synthesis, including physical measurement techniques, to fabrication engineering regarding entire thermoelectric systems as thermoelectric generators (TEG).

The (Bi,Sb)-Te based materials are those showing the best thermoelectric performance in terms of energy conversion from a thermal energy current to an electric energy current. But those semimetallic compounds are expensive, toxic and thermomechanically and thermochemically unstable. The most problematic property is the oxidation of the tellurides, starting at temperatures of approximately 473 K (200°C). For temperatures above this temperature other material classes as ceramics (synthetic oxides) exhibit beneficial behavior.

In the present work oxide phases were synthesised and the thermoelectric transport properties were measured. Furthermore, the structures of synthesised compounds were studied using X-ray diffraction methods and electron microscopy measurements including the energy dispersive X-ray spectroscopy. The studied phases are p-type and n-type semiconductors. ZnO-based phases were investigated with the result that the charge carrier concentration is hard to increase by doping. Due to the isolating behavior of fully oxidised ZnO-based compounds they were prepared by mixing it with perovskite-based phases, in order to receive ceramic composite material with beneficial thermoelectric properties and cost reduction by using the cheap ZnO phase. Perovskite phases as CaMnO₃-based systems were also studied as single phase compounds.

As p-type semiconductor the Ca₃Co₄O₉-based compounds were synthesised and studied. Aforementioned materials show a high charge carrier concentration even at low temperatures compared to other oxide phases. Furthermore the Seebeck coefficient (thermopower) of those layered cobaltite systems is very high and the thermal conductivity is very low. These properties make cobaltite ceramics the most efficient thermoelectric oxide-compounds. The Ca-Co-O system was also prepared as composite phase, including ceramic Cu-O and metallic Ag phases.

From synthesised materials thermoelectric generators for high- and low-temperature application were constructed. There were two approaches to assemble the materials to form a thermoelectric energy conversion system. The first one is the conventional rigid design fixing the electrical series connection of material legs between Al₂O₃-plates. The second design is a flexible one where the materials were assembled on a flexible fiber band. These strip-TEGs are constructed as open systems that are

compacted by coiling after fabrication. Related to both designs materials were exchanged to match the TEG's properties to certain temperature conditions.

To predict a generator's performance and get to know about the distributions of determining quantities inside the generator's materials a finite element (FEM) simulation tool was developed. The model was validated with experimental data of a commercially available thermoelectric generator and then used to simulate house-made generator systems.

Keywords:

Thermoelectric, Materials, Generators

Zusammenfassung

Der thermoelektrische Effekt eröffnet die Möglichkeit Energie-Konversionssysteme zu konstruieren, die einen thermischen Energiestrom direkt in einen elektrischen Energiestrom umwandeln. Diese thermoelektrischen Generatoren sind handlich (oder sogar tragbar), frei von mechanisch beweglichen Teilen, geräuschlos und wartungsfrei. Das Forschungsgebiet der Thermoelektrik ist höchst interdisziplinär und reicht von Festkörperchemie für die Materialsynthese, physikalische Messmethoden beinhaltend, bis hin zur Konstruktion kompletter thermoelektrischer Systeme wie thermoelektrischer Generatoren (TEG).

Die (Bi,Sb)-Te basierten Materialien zeigen die beste Performance in Bezug auf die Konversionseffizienz. Diese intermetallischen Verbindungen sind jedoch teuer, giftig und thermomechanisch und thermochemisch instabil. Die problematischste Eigenschaft ist die Oxidation des Tellurids, die bei etwa 473 K (200°C) eintritt. Oberhalb dieser Oxidationstemperatur zeigen andere Materialien wie Keramiken vorteilhafte Eigenschaften.

In der vorliegenden Arbeit wurden verschiedenartige Oxid-Verbindungen synthetisiert und deren Transporteigenschaften gemessen. Weiterhin wurden die Strukturen der synthetisierten Phasen mithilfe von Röntgen-Strukturuntersuchungen bestätigt und die Daten mit der Rietveld Methode analysiert. Die Strukturen wurden weiterhin mit elektronen-mikroskopischen und energie-dispersiven Techniken untersucht. Die synthetisierten und analysierten Verbindungen beinhalten sowohl n- als auch p-Halbleiter. ZnO basierte Phasen wurden untersucht, mit dem Ergebnis, dass die Ladungsträgerkonzentration mit Bezug auf die elektrische Leitfähigkeit durch Dotierung kaum modifiziert werden kann. Aus diesem Grund wurden die ZnO basierten Verbindungen in Komposit-Keramiken verwendet, indem sie mit Perovkit Verbindungen gemischt wurden. Die Perovkite wurden ebenfalls als separate Phasen untersucht. Die CaMnO_3 basierten Verbindungen zeigen, wie auch ZnO, einen elektronischen n-Typ Leitungsmechanismus.

Als Basis p-Halbleiter wurde $\text{Ca}_3\text{Co}_4\text{O}_9$ verwendet. Dieses Material weist, verglichen mit anderen thermoelektrischen Oxiden, eine moderate Ladungsträgerkonzentration auch bei tieferen Temperaturen nahe der Raumtemperatur auf. Dieses System zeigt weiterhin einen hohen Wert des Seebeck Koeffizienten (Thermokraft) und eine geringe thermische Leitfähigkeit. Diese Eigenschaften machen die Cobaltit Keramiken zu den effizientesten thermoelektrischen Oxid-Verbindungen, die heute bekannt sind. Das Ca-Co-O System wurde ebenfalls als Kompositmaterial hergestellt, die neben der Hauptphase auch Cu-O Phasen und metallische Ag Einschlüsse beinhalten.

Die synthetisierten Materialien wurden in thermoelektrischen hoch- und tieftemper-

atur Generatoren verbaut. Für das Design der Generatoren wurden zwei Ansätze verfolgt. Ein Ansatz zielt auf den konventionellen starren Aufbau ab, bei dem die elektrische Reihenschaltung der thermoelektrischen Material Schenkel zwischen zwei keramischen Al_2O_3 Platten realisiert wurde. Der zweite Ansatz beinhaltet eine mechanisch flexible Lösung, bei der die thermoelektrischen Materialien auf einem flexiblen Substratband aufgebracht wurden. Die flexiblen Streifengeneratoren werden als offene Systeme konstruiert und im Nachhinein mittels Aufwickeln kompaktiert. Bezüglich beider Bauweisen wurden Materialien ausgetauscht, um die Eigenschaften der Generatoren zu variieren und an verschiedene Temperaturbedingungen anzupassen.

Um die Leistungseigenschaften der Generatoren vorherzusagen und die Verteilung der bestimmenden Größen innerhalb der eingebauten Materialien zu bestimmen, wurden Finite-Elemente-Simulationen (FEM) durchgeführt. Das Modell wurde mithilfe experimenteller Daten des vermessenen kommerziell erhältlichen thermoelektrischen Generators validiert und anschließend auf einen hausgemachten Prototypen angewendet.

Schlagwörter:

Thermoelektrik, Materialien, Generatoren

Abbreviations

CCO	$\text{Ca}_3\text{Co}_4\text{O}_9$
EDTA	Ethylendiaminetetraacetic acid
EDXS	Energy Dispersive X-ray Spectroscopy
EELS	Electron Energy Loss Spectroscopy
FEM	Finite-Element Simulation Method
HRTEM	High Resolution Transmission Electron Microscopy
ITO	$\text{In}_{2-x}\text{Sn}_x\text{O}_3$
LCMO	(Ca, La) MnO_3 perovskite
SAED	Selected Area Electron Diffraction
SEM	Scanning Electron Microscopy
TE	Thermoelectric
TEG	Thermoelectric Generator
TEM	Transmission Electron Microscopy
XRD	X-ray Diffraction

Contents

Preface	v
Acknowledgment	vii
Abstract	ix
Zusammenfassung	xi
Abbreviations	xiii
1 Introduction	1
1.1 Development of thermoelectric research	1
1.2 Uncoupled transport of entropy and charge	2
1.2.1 Isothermal electronic conduction	2
1.2.2 Isoelectrical thermal conduction	5
1.3 Coupling of entropy and charge	6
1.4 Conversion efficiency and electrical power	8
1.5 Thermoelectric materials	10
1.5.1 Material synthesis via sol-gel method	12
1.5.2 Composite materials	13
1.6 Thermoelectric generators	14
List of Figures	17
Bibliography	22
2 Thermoelectric materials research	23
2.1 Summary	23
2.2 Experimental and Theoretical Thermoelectric Investigations of n-type Composite Oxide Materials	24
2.3 Enhanced Flexible Thermoelectric Generators based on Oxide-Metal Composite Materials	35
3 Thermoelectric generators research	47
3.1 Summary	47
3.2 Oxide-Based Thermoelectric Generator for High-Temperature Appli- cation Using p-Type $\text{Ca}_3\text{Co}_4\text{O}_9$ and n-Type $\text{In}_{1.95}\text{Sn}_{0.05}\text{O}_3$ Legs	48

3.3	An Approach to a Flexible Thermoelectric Generator Fabricated using Bulk Materials	59
3.4	Finite-Element Simulations of a Thermoelectric Generator and Their Experimental Validation	71
3.5	Experimental Characterisation and Finite-Element Simulations of a Thermoelectric Generator with Ceramic p-type $\text{Ca}_3\text{Co}_4\text{O}_9$ and Metallic $\text{Cu}_{0.57}\text{Ni}_{0.42}\text{Mn}_{0.01}$ legs	82
4	Conclusions	91
	Publications and Conferences	I

1 Introduction

1.1 Development of thermoelectric research

The thermoelectric effect was primarily obtained by Thomas Johann Seebeck in 1895 [1]. Related effects as the Peltier effect and the Thomson effect were discovered by Jean Charles Athanase Peltier and William Thomson, respectively. The combination of thermodynamics (dynamics of heat) and electrodynamics (dynamics of charge) leads to the physical descriptions of thermoelectric observations. That means, that on the one hand the transport of heat at non-isoelectric conditions and on the other hand the transport of charge at non-isothermal conditions were started to be investigated in detail. The isoelectric material-specific heat conductivity λ was described by Jean Baptiste Joseph Fourier [2]. The isothermal material-specific electric conductivity σ was investigated by Georg Simon Ohm [3]. The entropy current I_S and the electric current I_q inside the regarded material with cross-sectional area A and length L of the specimen are generated by differences of the thermal potential ΔT and of the electric potential $\Delta\varphi$. Such approaches give a linear dependance of the generated currents and the driving forces exhibited by differences of mentioned potentials. The coupling of bosonic (phonons) and fermionic (electrons, defect-electrons) interactions inside the regarded matter leads to direct conversion of thermal energy density (entropy) to electric energy density (charge) without transformation by kinetic mechanism of macroscopic devices (e.g. turbine, Stirling engine, etc). The resulting material specific coefficients that describe the interaction of mentioned quantities are the Seebeck coefficient α (related to thermovoltage $\Delta\varphi_{th}$) and the Peltier coefficient Π . The coefficients are linked via the Thomson relation concerning the Joule heat that was found by William Thomson, later known as Lord Kelvin.

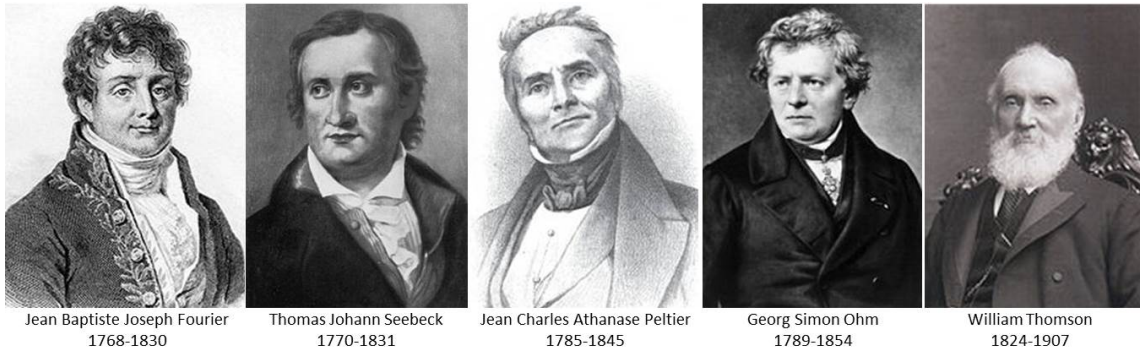


Figure 1: Scientists that developed the base for thermoelectric research.

1.2 Uncoupled transport of entropy and charge

Describing the thermoelectric transport properties of a certain material needs to know the characteristic transport coefficients for the uncoupled transported species of fermions and bosons [4, 5]. At high charge carrier concentration in the regarded material the thermoelectric effect in the sense of Seebeck, the possibility of counter ionic transport and related changes in the chemical potential are negligible. The dominant transported charged species q are electrons e^- and/or defect-electrons (holes) h^+ and the determining potential is the electrical potential φ . The entropy potential is the absolute Temperature T . In the following sections the isothermal electronic transport and the isoelectric thermal transport will be elucidated before explaining the coupling phenomenon of illustrated transported species. For a linear dependance of the potential gradients ∇ and the sample length L the local change in the potentials can be expressed as differences Δ .

1.2.1 Isothermal electronic conduction

In the framework of the theory of electronic structures of solid-state matter the electronic conductivity is described using the periodicity of atomic or ionic lattices of certain material crystals [5, 6]. The crystal orbitals are received as a linear combination of structure building atom orbitals which form energy-bands in dependance of the wave vectors. These bands are filled with electrons applying the exclusion principle of Pauli. The electronic structure depends on the kind and number of valence electrons referring to the regarded many-body system. By combining multiple bodies (charge carriers) to wave-packages quasi-classical descriptions can be used. Regarding the wave-packages the mobility μ can be described using the respective group velocity. Equation 3 illustrates the correlation of the mobility and the group velocity \bar{v} of electrons (n) and defect-electrons (p) applying an electric field \vec{E} .

$$\mu_n = \frac{\bar{v}_n}{|\vec{E}|}, \quad \mu_p = \frac{\bar{v}_p}{|\vec{E}|} \quad (1)$$

The group velocity is a function of the effective mass m^* which is the parameter describing the curvature of the energy-band. In Equation 2 the dependance of the mobility on the effective mass and the median flight time τ is shown.

$$\mu = \frac{e \cdot \tau}{m^*} \quad (2)$$

If the dominant scattering process is phonon scattering the temperature dependance of charge carriers mobility is received as shown in Equation 3 [5, 7].

$$\mu \propto T^{-\frac{3}{2}} \quad (3)$$

The scattering mechanism of charge carriers effects the thermopower of a certain material dramatically and influences the temperature dependance of the Seebeck coefficient [7].

The concentration of charge carriers n at the Fermi level is the second parameter determining the electric conductivity of a certain material. The temperature dependence of the charge carrier concentration is then obtained as shown in Equation 4 for n-type materials (left Equation) and for p-type materials (right Equation).

$$n_n = N_C \cdot \exp\left(-\frac{E_C - E_F}{k_B \cdot T}\right), \quad n_p = N_V \cdot \exp\left(-\frac{E_F - E_V}{k_B \cdot T}\right) \quad (4)$$

N_C is the density of states (DOS) for the conduction band (electron conduction) and N_V is the density of states for the valance band (hole conduction). E_C and E_V are the energies of the charge carriers in the conduction and valance band, respectively. If no other inserted states are generated by doping, the conduction mechanism is called intrinsic. Doping differently charged ions into the material causes additional states in the electronic band structure of the entire material phase. If such additional states are formed, the conduction mechanism is called extrinsic. In n-type materials, the additional states act as donor-states. The additional state is shown in Equation 5 exhibiting the density of states N_D with a charge carrier concentration n_D^+ and the energy E_D .

$$n_n = n_p + n_D^+ = N_V \cdot \exp\left(-\frac{E_F - E_V}{k_B \cdot T}\right) + \frac{N_D}{1 + 2\exp\left(\frac{E_F - E_D}{k_B \cdot T}\right)} \quad (5)$$

Concerning extrinsic hole conduction the additional charge carrier concentration n_A^+ of the additional states N_A exhibiting the energy E_A . The description for p-type conduction is shown in Equation 6.

$$n_p = n_n + n_A^+ = N_L \cdot \exp\left(-\frac{E_L - E_F}{k_B \cdot T}\right) + \frac{N_A}{1 + 2\exp\left(\frac{E_A - E_F}{k_B \cdot T}\right)} \quad (6)$$

The specific isothermal electric conductivity σ is obtained as the product of the charge carrier mobility and the charge carrier concentration multiplied by the elemental charge e .

$$\sigma = (n_n \cdot \mu_n + n_p \cdot \mu_p) \cdot e \quad (7)$$

The specific isothermal electric conductivity is the proportionality factor for the relation of electric potential $\Delta\varphi$ and the electric current density j_q . Considering the sample geometry with cross-sectional area A and length L , the entire electric current I_q in the material sample is obtained by Ohm's law.

$$I_q = -\left(\frac{A}{L}\right) \sigma \cdot \Delta\varphi \quad \text{with} \quad \nabla\varphi \approx \frac{\Delta\varphi}{L} \quad (8)$$

The potential difference $\Delta\varphi$ is commonly expressed as voltage U . The current density and the entire electric current are linked by the cross-sectional area A of the sample.

$$I_q = A \cdot j_q \quad (9)$$

Using Equation 8, the material specific isothermal electric conductivity of a certain sample can be estimated. The temperature dependence of intrinsic and extrinsic conduction mechanism is shown in the illustration of Figure 2.

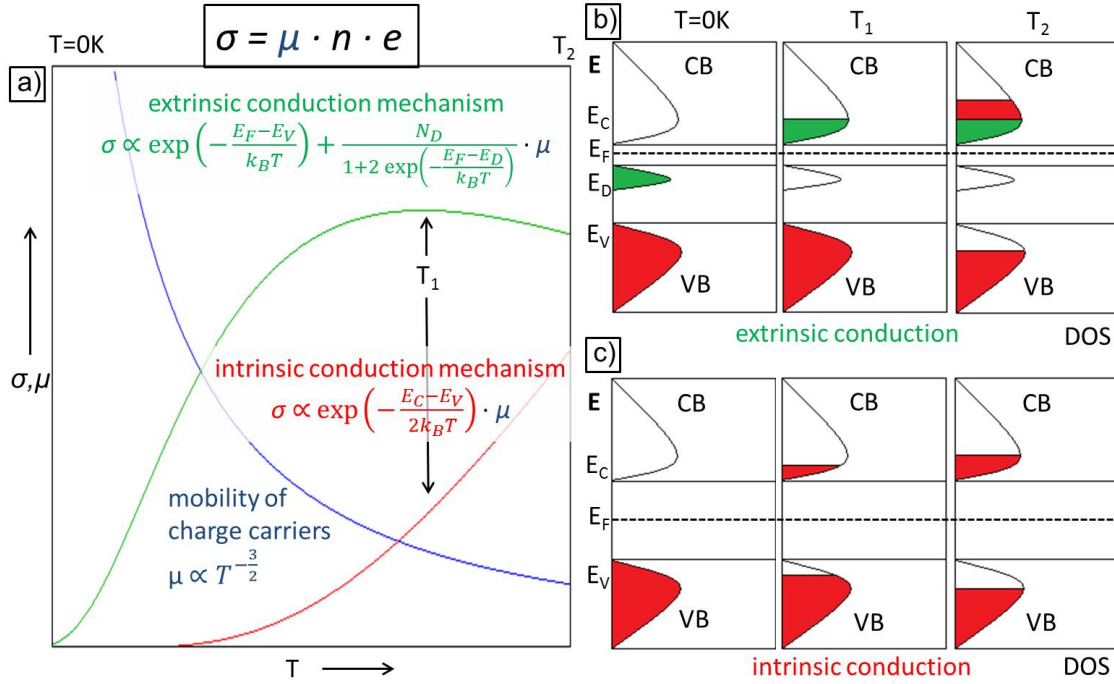


Figure 2: Illustration of the temperature dependence of the isothermal electric conductivity for intrinsic conduction (green) and for extrinsic conduction (red) and the charge carrier mobility (blue); a) temperature dependence of the electric conductivity σ and charge carrier mobility μ , b) schematic density of states (DOS) for extrinsic conduction mechanism, c) schematic density of states (DOS) for intrinsic conduction mechanism.

1.2.2 Isoelectrical thermal conduction

Isoelectric means, that there is no difference in the electric potential regarding the thermal conduction through the material. The thermal conduction without considering changes in the electric potential leads to the description of heat conduction by Fourier's law as given by Equation 10 [8, 9], that do not especially consider the amount of entropy transported by charge carriers. The thermal energy is transported by bosonic lattice force carriers, namely phonons. For ideal lattice heat conduction the electronic system of the regarded material is not influenced by changes of the thermal potential. If the change in the electronic structure of the sample is negligible, the relation of the thermal energy flux P_{th} related to the entropy current I_S can be described as follows. The difference in entropy potential ΔT is obtained in the same way the electric phenomenon is described by Ohm's law [3].

$$P_{th} = - \left(\frac{A}{L} \right) \lambda \cdot \Delta T \quad \text{with} \quad \nabla T \approx \frac{\Delta T}{L} \quad (10)$$

The proportionality factor for thermal conduction is the heat conductivity λ . The heat conductivity λ is related to the entropy conductivity Λ via the absolute working temperature T .

$$\lambda = \Lambda \cdot T \quad (11)$$

The transported quantity of entropy is then obtained by the transport equation for entropy conduction that is presented in Equation 12.

$$I_S = - \left(\frac{A}{L} \right) \Lambda \cdot \Delta T \quad (12)$$

The heat conductivity λ is the product received by three contributions: the heat capacity C_P , the mass density ρ and the thermal diffusivity D_{th} . The relation is presented in Equation 13.

$$\lambda = C_P \cdot \rho \cdot D_{th} \quad \text{and} \quad \Lambda = \frac{C_P \cdot \rho \cdot D_{th}}{T} \quad (13)$$

The entropy current density j_S and the entire entropy current I_S are linked by the cross-sectional area of the sample A in the analog way as for electric quantities.

$$I_S = A \cdot j_S \quad (14)$$

1.3 Coupling of entropy and charge

If a (semi-)conductive solid state material is placed in a temperature gradient an electrical gradient will build up due to the thermodiffusion of charge carriers. The displacement of charge carriers in the temperature gradient is caused by the dependence on the position of the velocity vectors. The median velocity vector points from the hot side to the cold side of the (semi-)conductor. The Seebeck coefficient α is determined for the electrical open-circuit case ($I_q = 0$) [10–12].

For the entire algebraic description of the thermoelectric coupling phenomenon for all possible cases it is advantageous to use a matrix illustration. The material-specific tensor contains the material-specific coefficients that relate the differences of regarded physical potentials to the generated fluxes. Considering the geometry of the material sample the absolute fluxes are obtained. The entire transport-equation, that considers each thermal and electrical situation of a regarded material sample, is presented in Equation 15.

$$\begin{pmatrix} I_S \\ I_q \end{pmatrix} = -\frac{A_{leg}}{L_{leg}} \cdot \begin{pmatrix} \sigma \cdot \alpha^2 + \Lambda & \sigma \cdot \alpha \\ \sigma \cdot \alpha & \sigma \end{pmatrix} \cdot \begin{pmatrix} \Delta T \\ \Delta \varphi \end{pmatrix} \quad (15)$$

One part of the material tensor is the power factor $\sigma\alpha^2$ describing the charge carrier related entropy conductivity with addition of the electric open-circuit entropy conductivity Λ . The combined parameter $\sigma\alpha$ is the coupling parameter. The isothermal specific electric conductivity σ is the determining parameter for vanishing temperature difference ($\Delta T = 0$) resulting in the isothermal description of Ohm's law (Equation 8). For vanishing difference in the electric potential ($\Delta \varphi = 0$) the electric current I_q is determined by the coupling factor $\sigma\alpha$.

For determining the Seebeck coefficient α of a certain material the measurement setup is in electrical open-circuit condition ($I_q = 0$). The resulting relation for this case is shown in Equation 16.

$$\Delta \varphi = -\alpha \cdot \Delta T \quad (16)$$

The short-circuit electric current ($\Delta \varphi = 0$) is obtained as another special case, represented in Equation 17.

$$I_q = -\left(\frac{A}{L}\right) \sigma\alpha \cdot \Delta T \quad (17)$$

In Figure 3a the special case for electric open-circuit and in Figure 3b for the electric short-circuit case are illustrated. Figure 3c presents the electrical characteristics for varying the external load resistance R_{load} in the thermoelectric circuit, ranging from electric open-circuit voltage ($R_{load} = \infty$ and $I_q = 0$) to electric short-circuit conditions ($R_{load} = 0$ and $\Delta \varphi = 0$).

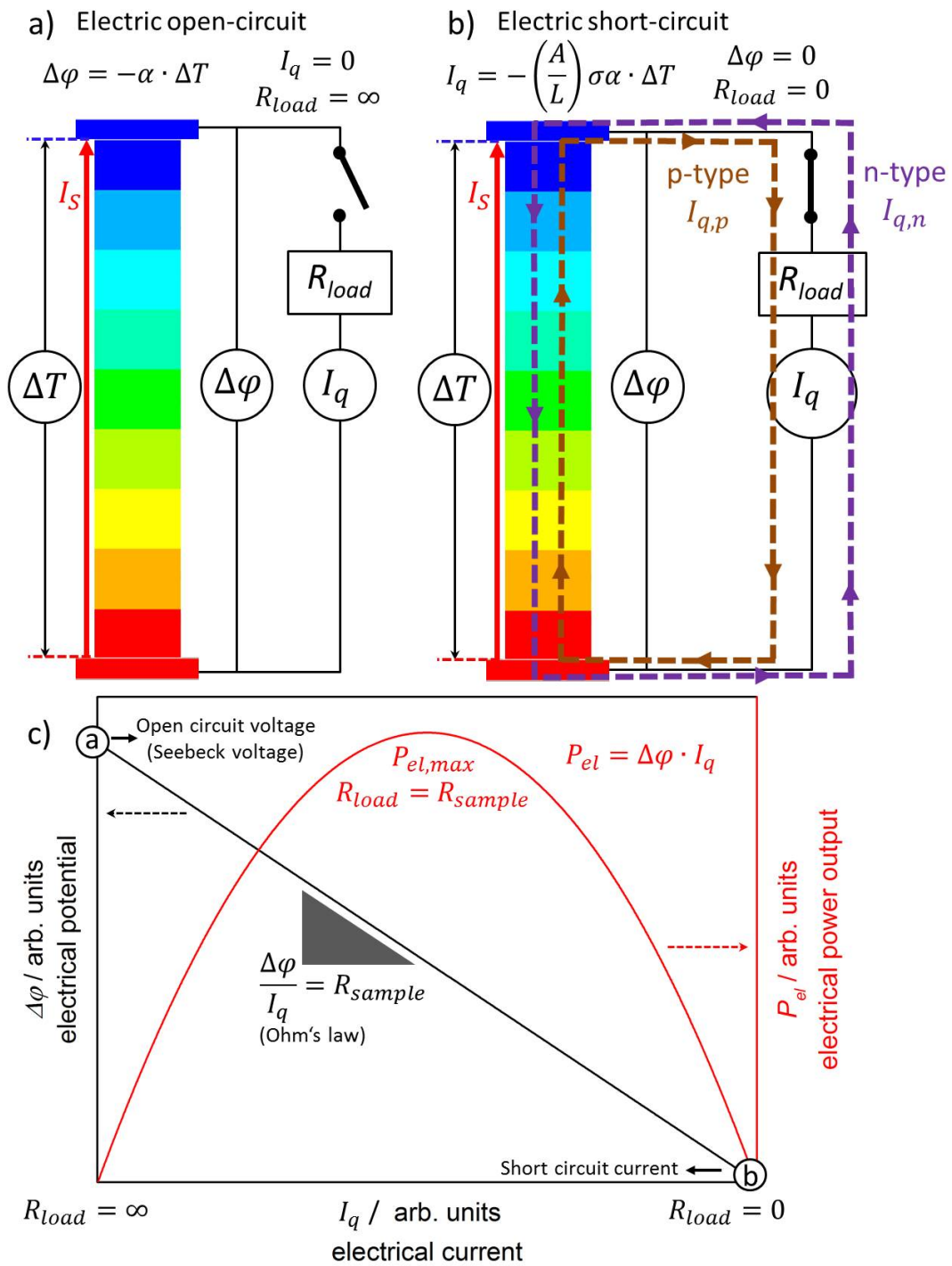


Figure 3: Schematic illustration for the thermoelectric coupling phenomenon. a) Electric open-circuit situation, b) Electric short-circuit situation with displayed thermal induced electric ring-current, c) Voltage-electric current and electric power-electric current characteristics with relation to subfigures a and b).

1.4 Conversion efficiency and electrical power

The figure of merit ZT_{TE} for thermoelectric materials gives a relation to the conversion efficiency and can be expressed by the parameters thermovoltage (electric open-circuit) $\Delta\varphi_{OC}$, the short-circuit electric current $I_{q,SC}$ and the entire electric resistivity R that is related to the geometry of the regarded sample, according to the following descriptions [13].

$$ZT = \frac{\Delta\varphi_{OC}}{I_{q,SC} \cdot R} - 1 = \frac{\sigma \cdot \alpha^2}{\lambda} \cdot T = \frac{\sigma \cdot \alpha^2}{\Lambda} \quad (18)$$

The first term can directly be used to estimate the figure of merit for an entire generator ZT_{TEG} . The figure of merit is related to the conversion efficiency η_{el} that increases with increasing power factor $\sigma\alpha^2$ and decreases with increasing heat conductivity λ . The conversion efficiency η is an important parameter if the thermoelectric generator is applied in a thermal potential gradient exhibiting a finite heat-source working at low thermal currents.

In order to maximize the electric output power P_{el} of a certain TEG, it is disadvantage to decrease the thermal conductivity of the integrated thermoelectric materials. Narducci published a remarkable work that gives an insight in thermoelectric power generation using infinite heat-sources with high thermal energy input. He postulates that the materials then needs to reach a threshold value for the thermal conductivity (not a minimized value for the thermal conductivity) to receive the maximum electric power output [14].

$$P_{el} = -\eta_{el} \cdot P_{th} = -\eta_{el} \cdot \frac{A_{leg}}{L_{leg}} \cdot \lambda \cdot \Delta T \quad (19)$$

Hence, for infinite heat-sources the heat conductivity λ must not have to exhibit too low values to harvest the maximum electric power output. The amount of generated electric power is limited by the thermal power P_{th} fed into the TEG at the hot side. Regarding lower thermal resistances of the thermoelectric materials in the generator leads to an increase of the electric power output at suboptimal conversion efficiency. The efficiency at electric maximum power ($R_{TEG} = R_{load}$) η_{el} is obtained as shown in Equation 20.

$$\eta_{el} = \frac{1}{2} \cdot \frac{T_h - T_c}{T_h} \cdot \left(1 + \frac{2}{Z \cdot T_h} - \frac{\Delta T}{4 \cdot T_h} \right)^{-1} \quad (20)$$

The term in front of the bracket is the Carnot efficiency $\eta_c = \frac{T_h - T_c}{T_h}$. Therefore it is important to think about the intended application of a certain thermoelectric material. In Figure 4 the relation of the conversion efficiency η_{el} and the electrical power output P_{el} correlated to the heat conductivity λ and the thermal power P_{th} is presented. For too high heat conductivities the thermal short-cut results in a decreasing temperature difference ΔT over the sample length L .

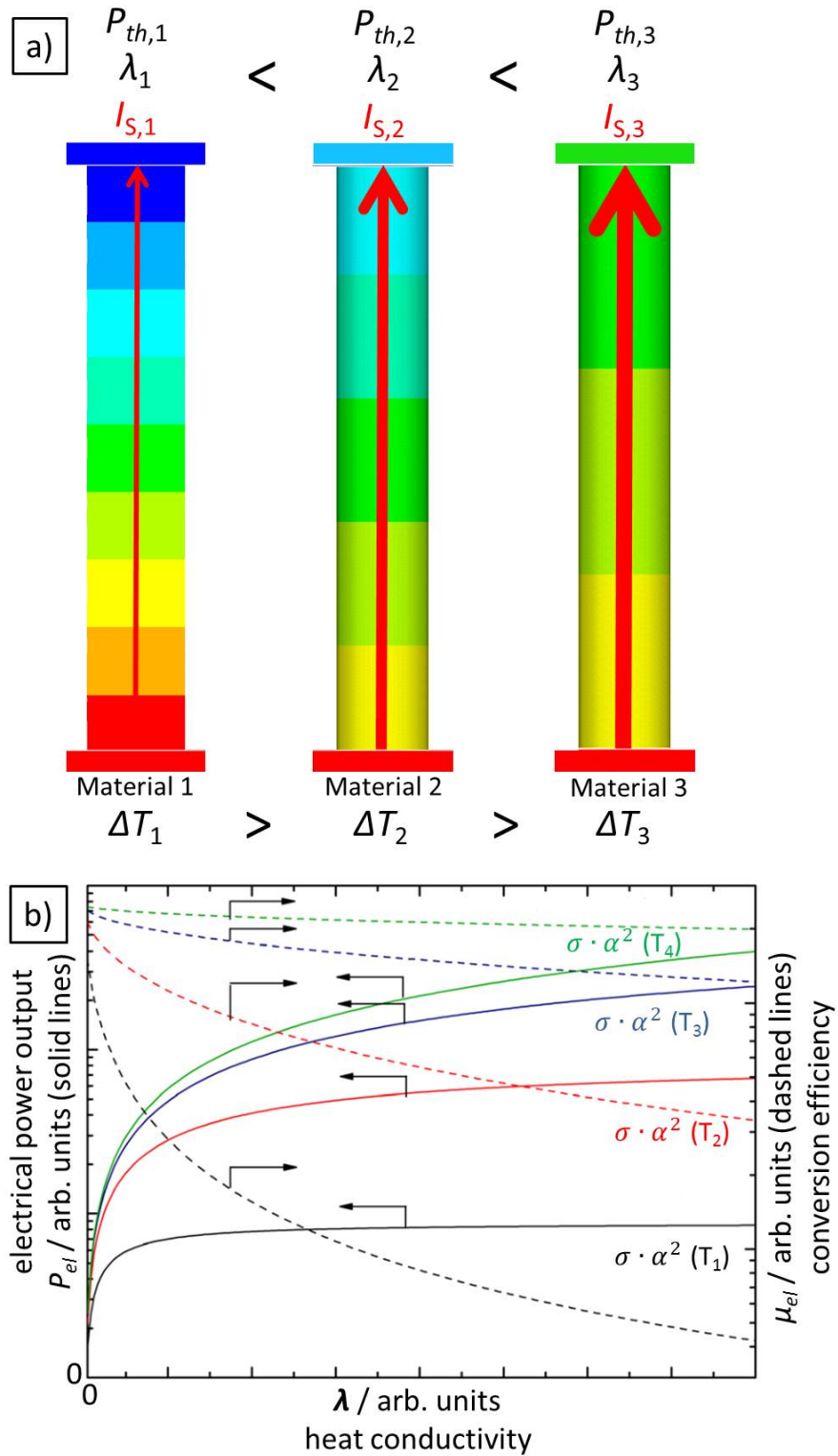


Figure 4: Dependence of the electric power output P_{el} and conversion efficiency η_{el} to the heat conductivity λ and the thermal power P_{th} . a) Schematic illustration of three different material legs with increasing heat conductivity: thickness of red arrows are related to the amount of transported entropy, b) Narducci-Plot [14] for different power factors $\sigma \cdot \alpha^2$ showing the increase of the electric power P_{el} and the decrease of the efficiency η_{el} with increasing heat conductivity λ .

1.5 Thermoelectric materials

In the present work different material classes with very different thermoelectric properties were used.

- The ZnO zincite is hard to dope and the most effective modification is the integration of Al^{3+} at the Zn^{2+} -sites [15–18]. However, this compound exhibits a large value for the Seebeck coefficient and a low charge carrier concentration. From all investigated thermoelectric materials the ZnO-based compounds showed the most isolating character. ZnO-based composites are presented in section 2.2
- The $\text{Ca}_3\text{Co}_4\text{O}_9$ exhibits the highest power factor of all synthesised and characterised oxide-based materials. The high Seebeck coefficient and the moderate charge carrier concentration (even at room temperature) make this compound the most effective ceramic thermoelectric material [19–23]. Enhanced $\text{Ca}_3\text{Co}_4\text{O}_9$ -based composite phases are presented in section 2.3.
- Perovskite type ceramic materials were also investigated. These compounds are easy to dope. Therefore the thermoelectric properties can be adjusted in terms of charge carrier concentration. Co-based Perovskites exhibit a p-type conduction mechanism while the Mn-based Perovskites exhibit an n-type conduction mechanism [24, 25]. (Ca, La)MnO₃-based composites are presented in section 2.2.
- Beyond the oxide-based materials commercially available semiconductor materials, namely Bi_2Te_3 and Sb_2Te_3 based compounds, were analysed. These materials exhibit the highest figure of merit ZT of all known thermoelectric compounds. In terms of the conversion efficiency these tellurids show the best performance [26–30]. A (Bi, Sb)₂Te₃-based generator was analysed in section 3.4.
- Alloys exhibit the highest values of the power factor. Therefore it is advantageous to apply alloys like Cu-Ni in thermoelectric generators in order to increase the electric power output [31]. In section 3.3 and 3.5 the application of a Cu-Ni-Mn alloy is presented.

In Figure 5 the crystallographic structures of studied materials are assembled.

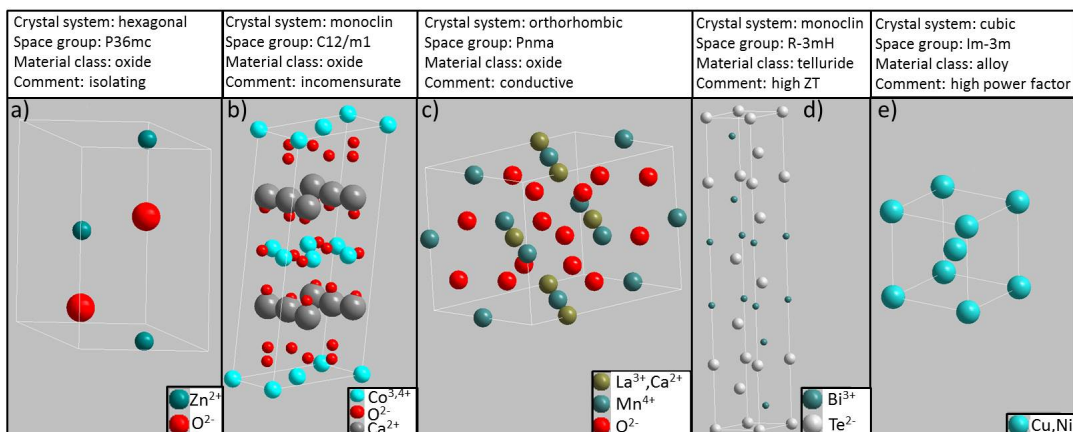


Figure 5: Schematic basic structures of synthesised, investigated and characterised thermoelectric compounds; a) ZnO Zincite, b) $\text{Ca}_3\text{Co}_4\text{O}_9$, c) (Ca, La)MnO₃ Perovskite, d) Bi_2Te_3 , e) Cu-Ni alloy.

In Figure 6 the determined thermoelectric properties of investigated materials are summarised. The data of Bi, Fe and Cu were taken from the literature [32].

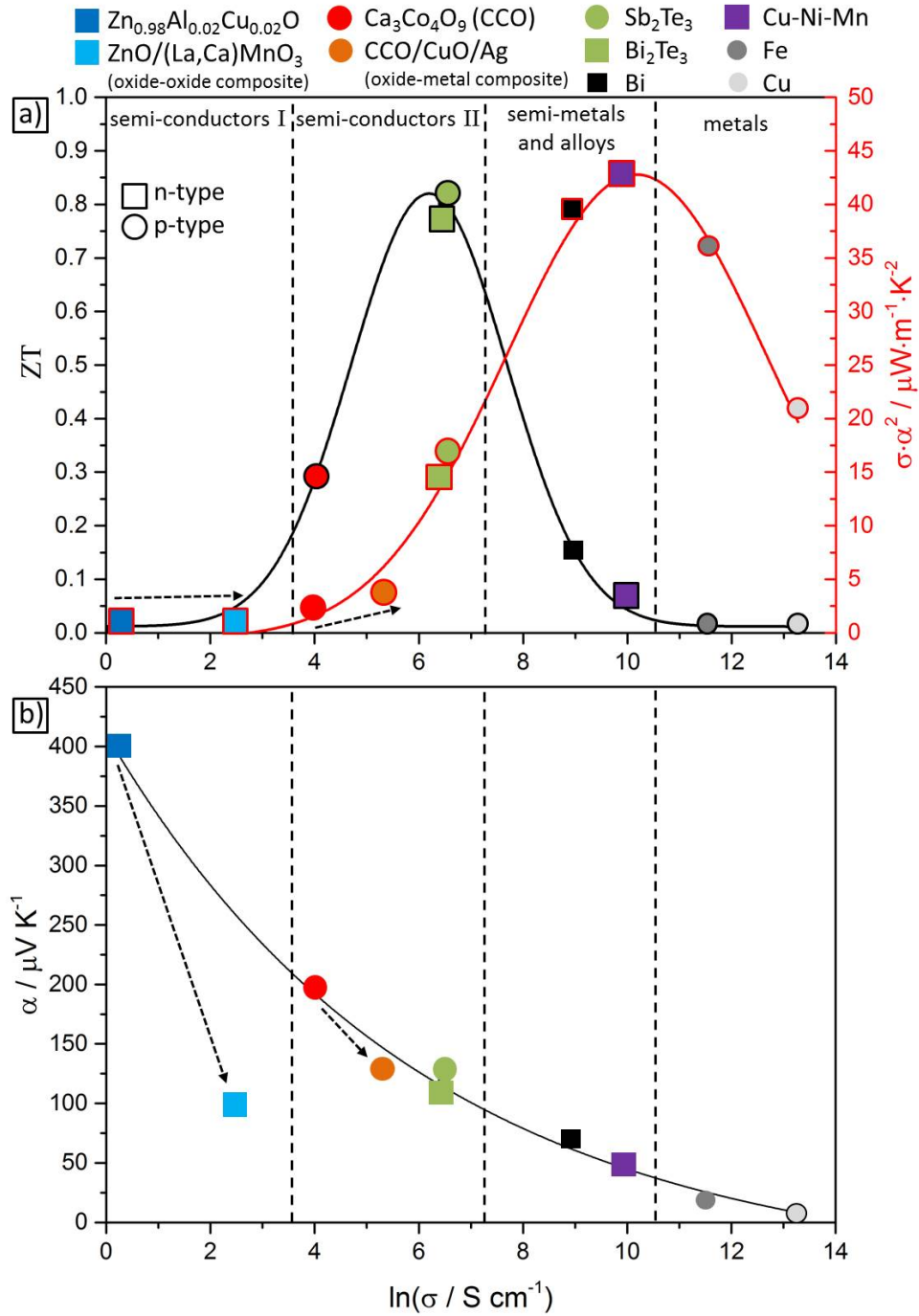


Figure 6: Determined thermoelectric parameters of materials investigated in this thesis plotted versus the logarithmic isothermal electric conductivity $\ln(\sigma)$ with dashed arrows that mark the changes in thermoelectric properties of correlated single-phase and composite materials; a) Figure of merit ZT (left, black axis) and power factor $\sigma \cdot \alpha^2$ (right, red axis), b) Seebeck coefficient α .

1.5.1 Material synthesis via sol-gel method

Ceramic materials are advantageous for applications at high temperatures because of their large binding energies and therefore of their high melting points. Ceramics are versatile materials, and nowadays, they exhibit a major technological importance [9]. Due to defect chemistry and physics, especially non-stoichiometric oxides aroused interest [33].

In the framework of the presented doctor thesis the thermoelectric oxide materials were synthesized using the sol-gel method [34, 35]. Nitrates of structure building cations were stoichiometrically added to an aqueous ammonia solution of pH = 9 containing citric acid and ethylenediaminetetraacetic acid (EDTA) for complexing the solvated metal ions. The solution was stirred about 12 h at 373 K until the gelation of the batch. The gel was transferred into a heater in order to dry and roast the aqueous batch to a solid state intermediate. In the next step the intermediate was calcined to a powder product providing already the aspired stoichiometry. Finally, the powder was cold pressed and sintered to a ceramic bulk material. In Figure 7 the schematic sol-gel process is illustrated using the example of the process for the synthesis of the $\text{Ca}_3\text{Co}_4\text{O}_9$ ceramic.

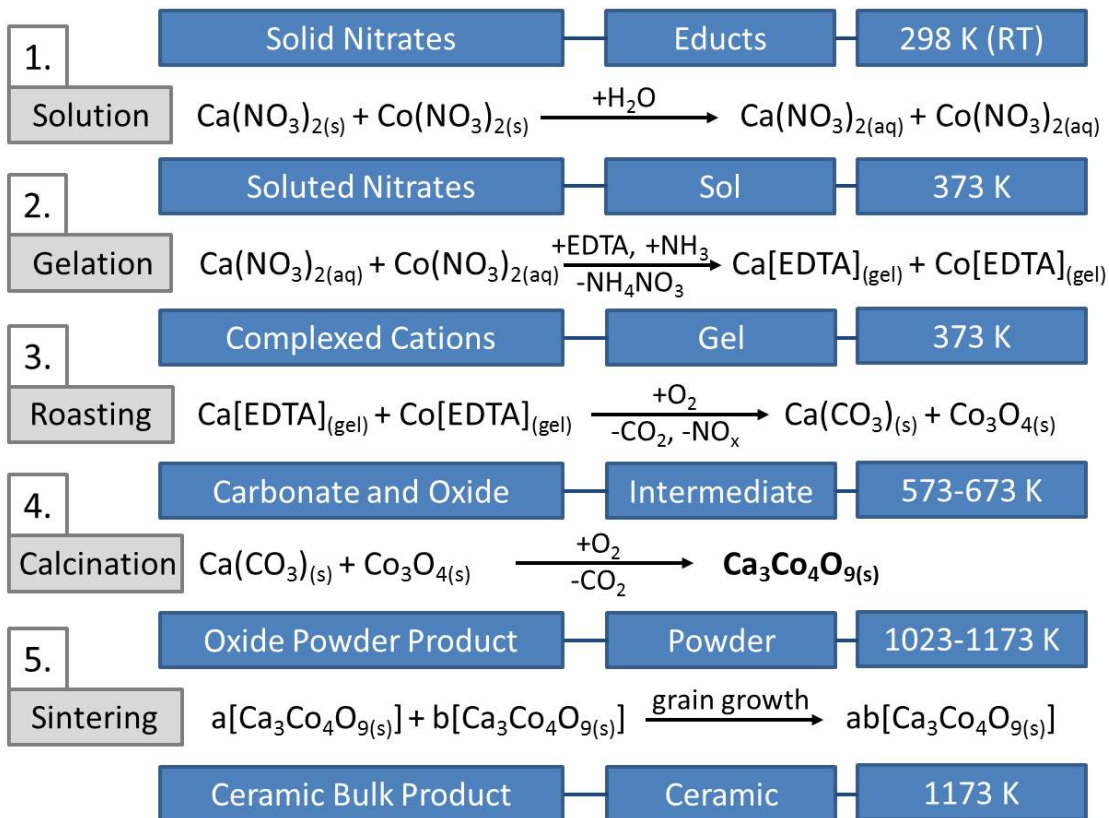


Figure 7: Schematic illustration of the synthesis process via sol-gel route using the example of the $\text{Ca}_3\text{Co}_4\text{O}_9$ ceramic.

1.5.2 Composite materials

The material synthesis that is described in the previous section can be modified to produce composite materials. If a composite material is aspired there are two possibilities to realise the production.

The first one is called the one-pot synthesis. Using this method the cations are batched stoichiometrically for more than one single phase. The different structures are build next to each other. If the radii of structure building cations in the different structures are very different, the composite material can be obtained with a minimum of additional intergrown phases. If the radii are similar, the phases interpenetrate each other and form additional phases resulting in multicomponent systems [9]. For the case of similar ionic radii and charge of added cations the composite material is better produced by the two-pot synthesis route.

Using the two-pot synthesis, the single phases are synthesised as separated powder products. These powders are mixed up (e.g. sonification in a dispersion medium). After homogenisation the powder mixture is dried and cold pressed. The pressed body is then sintered for an adequate period of time to realise sintering but suppress intergrowing of the different phases.

The thermoelectric transport Equation 15 can be extended for description of thermoelectric composite materials, considering the fractions f_i of composite building single phases ($i = 1, 2, \dots$). The isothermal specific electronic composite conductivity σ_{comp} for a dual-phase material can be expressed as shown in Equation 21.

$$\sigma_{comp} = f_1\sigma_1 + f_2\sigma_2 = (f\sigma)_1 + (f\sigma)_2 \quad (21)$$

This result is based on the model of parallel plates of the materials in direction of electric current [36]. The entire thermoelectric transport equation is then obtained as shown in Equation 22 for a dual-phase composite including material 1 and 2 (see section 2.2).

$$\begin{aligned} \begin{pmatrix} j_{S,comp} \\ j_{q,comp} \end{pmatrix} &= f_1 \begin{pmatrix} j_{S,1} \\ j_{q,1} \end{pmatrix} + f_2 \begin{pmatrix} j_{S,2} \\ j_{q,2} \end{pmatrix} \\ &= - \begin{pmatrix} (f\sigma\alpha^2)_1 + (f\sigma\alpha^2)_2 + (f\Lambda)_1 + (f\Lambda)_2 & (f\sigma\alpha)_1 + (f\sigma\alpha)_2 \\ (f\sigma\alpha)_1 + (f\sigma\alpha)_2 & (f\sigma)_1 + (f\sigma)_2 \end{pmatrix} \cdot \begin{pmatrix} \nabla T \\ \nabla\varphi \end{pmatrix} \end{aligned} \quad (22)$$

For the electrical open-circuit case ($j_q = 0$) the relation for the Seebeck coefficient can be extracted in the same way it was done for single phase materials, see Equation 16. The Seebeck coefficient for a dual-phase thermoelectric material is then obtained as presented in Equation 23.

$$\alpha_{comp} = \frac{f_1\sigma_1\alpha_1 + f_2\sigma_2\alpha_2}{f_1\sigma_1 + f_2\sigma_2} = \frac{(f\sigma\alpha)_1 + (f\sigma\alpha)_2}{(f\sigma)_1 + (f\sigma)_2} \quad (23)$$

Hence, the determining parameters are the isothermal electric conductivities σ_i , the Seebeck coefficients α_i and the fractions f_i of each contributing single phase.

1.6 Thermoelectric generators

The construction of a thermoelectric generator (TEG) requires an electric series connection of a defect-electron (hole) conductor ($\alpha > 0$), where the motions of thermal and electric currents are directed in the same direction and an electron conductor ($\alpha < 0$), where the thermal and electric currents are directed in the opposite directions [37]. The material legs assembled in electric series are commonly connected using metallic (e.g., copper, gold, silver) connectors. If the device is placed in a drop of thermal potential ΔT , a difference in the electric potential $\Delta\varphi = U$ builds up, and, according to Equation 15, coupled currents I_S and I_q are generated. The direct conversion of thermal energy to electric energy is unique for thermoelectric systems. Hence, a TEG is a device that transfers energy from an entropy current directly to an electric current [37–39]. These properties make a thermoelectric generator useful for recovering (waste) heat in different processes.

The design were realized for rigid devices with chess board geometry. Flexible devices were also constructed assembling the thermoelectric materials on a flexible substrate band. Schematic illustrations for both designs are presented in Figure 8.

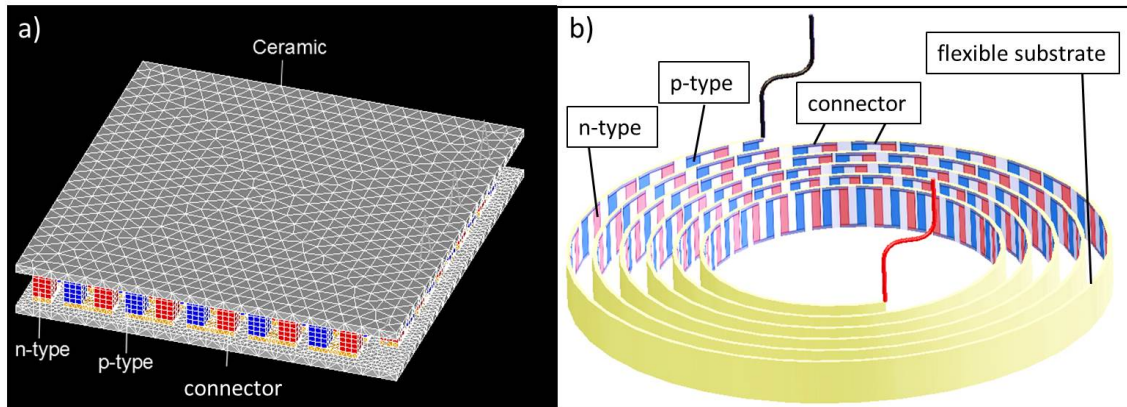


Figure 8: Schematic illustration of thermoelectric generator design. a) Rigid design with chess board geometry, b) Flexible design with Archimedean spiral geometry.

At the power-maximum of the characteristic parabolic power-plots the internal resistance of the generator R_{TEG} is equal to the external load-resistance R_{load} . The entire resistance R_{TEG} results in the addition of the resistances of each integrated thermoelectric leg (neglecting the electric resistances of metallic connectors). The maximum electric power output is then received by Equation 25.

$$P_{el,max} = \frac{(\Delta\varphi_{OC})^2}{4 \cdot R_{TEG}} = \frac{(\sum \alpha_{p-leg} - \sum \alpha_{n-leg})^2}{4 \cdot (\sum R_{p-leg} + \sum R_{n-leg})} \Delta T^2 \quad (24)$$

The thermovoltage $\Delta\varphi$ (U) increases with increasing number of integrated thermoelectric legs. But the entire electric resistivity of the TEG R_{TEG} also increases with increasing number of legs. For application it is therefore important to think about the balance of open-circuit voltage $\Delta\varphi_{OC}$ (U_{OC}) and short-circuit electric current $I_{q,SC}$ to harvest the maximum electric energy. Neglecting the connector resistivities the entire resistance is obtained as sum over all leg-resistances that are included in the generator:

$$R_{TEG} = R_{leg1} + R_{leg2} + R_{leg3} + \dots \quad (25)$$

The principle function of a thermoelectric generator, that generates a thermal induced electric ring current, is illustrated in Figure 9.

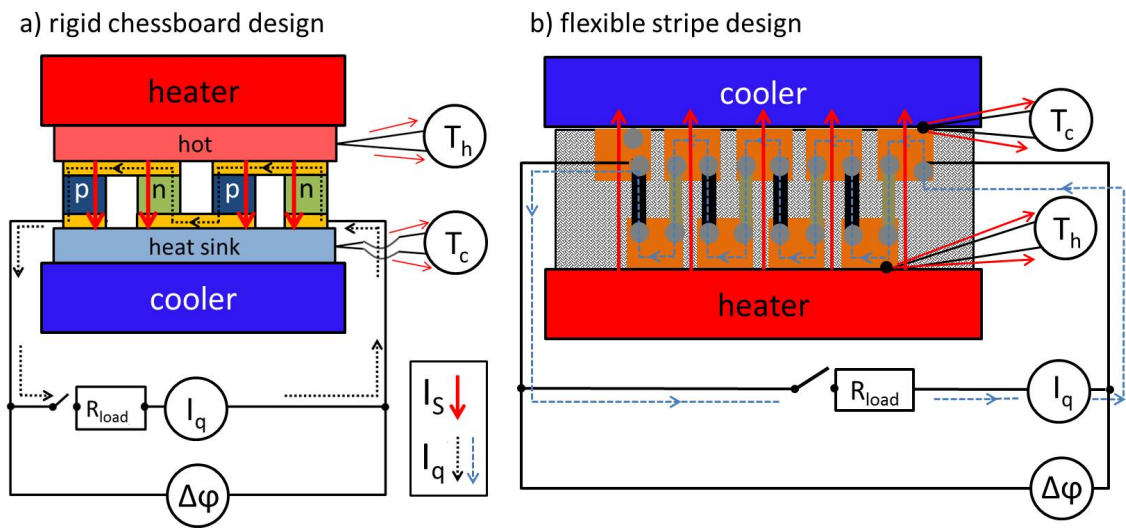


Figure 9: Principle function of a thermoelectric generator with displayed entropy flux (solid arrows) and electric flux (dashed arrows): The entropy flux is running from the hot to the cold side of the device, while the electric ring-current passes the device through the electric series connection of thermoelectric materials. a) rigid chessboard design, b) flexible stripe design.

List of Figures

1	Scientists that developed the base for thermoelectric research.	1
2	Illustration of the temperature dependence of the isothermal electric conductivity for intrinsic conduction (green) and for extrinsic conduction (red) and the charge carrier mobility (blue); a) temperature dependence of the electric conductivity σ and charge carrier mobility μ , b) schematic density of states (DOS) for extrinsic conduction mechanism, c) schematic density of states (DOS) for intrinsic conduction mechanism.	4
3	Schematic illustration for the thermoelectric coupling phenomenon. a) Electric open-circuit situation, b) Electric short-circuit situation with displayed thermal induced electric ring-current, c) Voltage-electric current and electric power-electric current characteristics with relation to subfigures a and b).	7
4	Dependence of the electric power output P_{el} and conversion efficiency η_{el} to the heat conductivity λ and the thermal power P_{th} . a) Schematic illustration of three different material legs with increasing heat conductivity: thickness of red arrows are related to the amount of transported entropy, b) Narducci-Plot [14] for different power factors $\sigma \cdot \alpha^2$ showing the increase of the electric power P_{el} and the decrease of the efficiency η_{el} with increasing heat conductivity λ	9
5	Schematic basic structures of synthesised, investigated and characterised thermoelectric compounds; a) ZnO Zincite, b) $\text{Ca}_3\text{Co}_4\text{O}_9$, c) (Ca, La) MnO_3 Perovskite, d) Bi_2Te_3 , e) Cu-Ni alloy.	10
6	Determined thermoelectric parameters of materials investigated in this thesis plotted versus the logarithmic isothermal electric conductivity $\ln(\sigma)$ with dashed arrows that mark the changes in thermoelectric properties of correlated single-phase and composite materials; a) Figure of merit ZT (left, black axis) and power factor $\sigma \cdot \alpha^2$ (right, red axis), b) Seebeck coefficient α	11
7	Schematic illustration of the synthesis process via sol-gel route using the example of the $\text{Ca}_3\text{Co}_4\text{O}_9$ ceramic.	12
8	Schematic illustration of thermoelectric generator design. a) Rigid design with chess board geometry, b) Flexible design with Archimedian spiral geometry.	14

- 9 Principle function of a thermoelectric generator with displayed entropy flux (solid arrows) and electric flux (dashed arrows): The entropy flux is running from the hot to the cold side of the device, while the electric ring-current passes the device through the electric series connection of thermoelectric materials. a) rigid chessboard design, b) flexible stripe design. 15

Bibliography

- [1] T. J. Seebeck, “Magnetische Polarisation der Metalle und Erze durch Temperatur-Differenz,” *Ostwald’s Klassiker der exakten Wissenschaften*, vol. 70, pp. 1–120, 1895.
- [2] T. N. Narasimhan, “Fourier’s heat equation: History, influence, and connections,” *Reviews of Geophysics*, vol. 37(1), pp. 151–172, 1999.
- [3] G. S. Ohm, “Die galvanische Kette mathematisch bearbeitet,” *T. H. Riemann*, vol. 1, pp. 1–245, 1827.
- [4] L. Landau and E. Lifschitz, *Lehrbuch Der Theoretischen Physik - Elektrodynamik Der Kontinua*. Lehrbuch, Dresden: Akademie Verlag Berlin, 8th ed., 1982.
- [5] H. Ibach and H. Lüth, *Festkörperphysik - Einführung in die Grundlagen*. Lehrbuch, Jülich: Springer, 3rd ed., 1989.
- [6] C. Kittel, *Einführung in die Festkörperphysik*. Lehrbuch, Dresden: R. Oldenburgverlag München Wien, 12th ed., 1999.
- [7] B. Nag, *Electron Transport in Compound Semiconductors*. Lehrbuch, Dresden: Springer-Verlag Berlin Heidelberg New York, 11. Series in Solid-Sate Siences ed., 1980.
- [8] J. Fourier, “Versuche über die Wärmeleitung in dünnen Körpern, und Beschreibung eines neuen Contactthermometers,” *Annalen der Physik*, vol. 89(6), pp. 327–343, 1828.
- [9] W. Kingery, H. Bowen, and D. Uhlmann, *Introduction to Ceramics*. Wiley series on science and technology of materials, USA: John Wiley & Sons Berlin Heidelberg New York, 2nd ed., 1976.
- [10] A. Ioffe, *Semiconductor Thermoelements and Thermoelectric cooling*. London: Infosearch Ltd. 1st ed., 1957.
- [11] A. Ioffe, *Physics of Semiconductors*. London: Infosearch Ltd. 1st ed., 1960.
- [12] C. Goupil, W. Seifert, K. Zabrocki, E. Müller, and G. Snyder, “Thermodynamics of thermoelectric phenomena and applications,” *Entropy*, vol. 13, pp. 1381–1517, 2011.

- [13] G. Min and D. Rowe, "A novel principle allowing rapid and accurate measurement of a dimensionless thermoelectric figure of merit," *Measurement Science and Technology*, vol. 12, pp. 1261–1262, 2001.
- [14] D. Narducci, "Do we really need high thermoelectric figures of merit? A critical appraisal to the power conversion efficiency of thermoelectric materials," *Applied Physics Letter*, vol. 99, pp. 102104–1 – 102104–3, 2011.
- [15] N. Schäuble, B. Süess, S. Populoh, A. Weidenkaff, and M. Aguirre, "A morphology study on thermoelectric Al-substituted ZnO," *European Conference on Thermoelectrics*, vol. 9, pp. 422–424, 2012.
- [16] M. Ohtaki, T. Tsubota, K. Egushi, and H. Arai, "High temperature thermoelectric properties of $\text{Zn}_{1-x}\text{Al}_x\text{O}$," *Journal of Applied Physics*, vol. 79(3), pp. 1819–1818, 1996.
- [17] M. Ohtaki, T. Tsubota, and K. . Egushi, "Thermoelectric properties of oxide solid solutions based on Al-doped ZnO," *International Conference of Thermoelectrics*, vol. 17, pp. 610–613, 1998.
- [18] N. Vogel-Schäuble, R. Dujardin, A. Weidenkaff, and M. Aguirre, "Influence of thermal aging phenomena on thermoelectric properties of al-substituted zno," *Journal of Electronic Materials*, vol. 41, pp. 1606–1614, 2011.
- [19] Y. Miyazaki, K. Kudo, M. Akoshima, Y. Ono, Y. Koike, and T. Kajitani, "Modulated structure of thermoelectric compound $[\text{Ca}_2\text{CoO}_3]\text{CoO}_2$," *Journal of the Physical Society of Japan*, vol. 39, pp. L531–L533, 2000.
- [20] M. Shikano and R. Funahashi, "Electrical and thermal properties of single-crystalline $(\text{Ca}_2\text{CoO}_3)_{0.7}\text{CoO}_2$ with a $\text{Ca}_3\text{Co}_4\text{O}_9$ structure," *Applied Physics Letter*, vol. 82(12), pp. 1851–1851, 2003.
- [21] O. Jankovsky, D. Sedmidubsky, Z. Sofer, P. Simek, and J. Hejtmanek, "Thermodynamic behavior of $\text{Ca}_3\text{Co}_{3.93+x}\text{O}_{9+\delta}$ ceramics," *Ceramics-Silikaty*, vol. 56(2), pp. 139–144, 2012.
- [22] S. Lambert, H. Leligny, and D. Gebrille, "Three forms of the misfit layered cobaltite $[\text{Ca}_2\text{CoO}_3][\text{CoO}_2]_{1.62}$ · A 4D structural investigation," *Journal of Solid State Chemistry*, vol. 160, pp. 322–331, 2001.
- [23] H. Fjellvåg, E. Gulbrandsen, S. Assland, A. Olsen, and B. Hauback, "Crystal structure and possible charge ordering in one-dimensional $\text{Ca}_3\text{Co}_2\text{O}_6$," *J. Solid State Chem.*, vol. 124, pp. 190–194, 1996.
- [24] A. Weidenkaff, R. Robert, M. Aguirre, L. Bocher, T. Lippert, and S. Canulescu, "Development of thermoelectric oxides for renewable energy conversion technologies," *Renewable Energy*, vol. 33, pp. 342–347, 2007.

- [25] P. Thiel, J. Eilertsen, S. Populoh, G. Saucke, M. Döbeli, A. Shkabko, L. Sagarna, L. Karvonen, and A. Weidenkaff, “Influence of tungsten substitution and oxygen deficiency on the thermoelectric properties of CaMnO_3 ,” *Journal of Applied Physics*, vol. 114, p. 243707, 2013.
- [26] J. Fleurial, L. Gailliard, R. Triboulet, H. Scherrer, and S. Scherrer, “Thermal properties of high quality single crystals of bismuth telluride - part I: experimental characterization,” *Journal of Physics and Chemistry of Solids*, vol. 49, pp. 1237–1247, 1988.
- [27] E. Kouhkarenko, N. Frety, V. G. Shepelevich, and J. C. Tedenac, “Electrical properties of $\text{Bi}_{2-x}\text{Sb}_x\text{Te}_3$ materials obtained by ultrarapid quenching,” *Journal of Alloys and Compounds*, vol. 327, pp. 1–4, 2001.
- [28] V. L. Kuznetsov, L. A. Kuznetsova, A. E. Kaliazin, and D. M. Rowe, “High performance functionally graded and segmented Bi_2Te_3 -based materials for thermoelectric power generation,” *Journal of Materials Science*, vol. 37, pp. 2893–2897, 2002.
- [29] G. J. Snyder and E. S. Toberer, “Complex thermoelectric materials,” *Nature Materials*, vol. 7, pp. 105–114, 2008.
- [30] C. Kim, D. H. Kim, H. Kim, and J. S. Chung, “Significant enhancement in the thermoelectric performance of bismuth telluride nanocompound through brief fabrication procedures,” *ASC Applied Materials and Interfaces*, vol. 4, pp. 2949–2954, 2012.
- [31] N. D. Lowhorn, W. Wong-Ng, W. Zhang, Z. Q. Lu, M. Otani, E. Thomas, M. G. T. N. Tran, N. Dilly, S. Ghamaty, N. Elsner, T. Hogan, A. D. Downey, Q. Jie, Q. Li, H. Obara, J. Sharp, C. Caylor, R. Venkatasubramanian, R. Willigan, J. Yang, J. Martin, G. Nolas, B. Edwards, and T. Tritt, “Round-robin measurements of two candidate materials for a Seebeck coefficient standard reference material,” *Applied Physics A*, vol. 94, pp. 231–234, 2009.
- [32] D. Lide, *CRC Handbook of Chemistry and Physics*. Internet Version 2009, Boca Raton, FL: CRC Press, 89th ed., 2008.
- [33] O. Sörensen, *Nonstoichiometric Oxides*. Materials science series, London: Academic Press, 1st ed., 1981.
- [34] M. Rahaman, *Ceramics Processing and Sintering*. Academic Division of Informa, Missouri USA: CRC Press, 2nd edition ed., 2003.
- [35] A. Feldhoff, M. Arnold, J. Martynczuk, T. Gesing, and H. Wang, “The sol-gel synthesis of perovskites by EDTA/citrite complexing method involves nanoscale solid state reactions,” *Solid State Sciences*, vol. 10, pp. 689–701, 2008.

- [36] R. Landauer, “The electrical resistance of binary metallic mixtures,” *Journal of Applied Physics*, vol. 23, pp. 779–784, 1952.
- [37] A. Feldhoff, “Thermoelectric material tensor derived from the Onsager - de Groot - Callen model,” *Energy Harvesting and Systems*, vol. 2(1), pp. 5–13, 2015.
- [38] H. Fuchs, *The Dynamics of Heat – A Unified Approach to Thermodynamics and Heat Transfer*. Graduate Texts in Physics, New York: Springer, 2nd ed., 2010.
- [39] H. Fuchs, “A direct entropic approach to uniform and spatially continuous dynamical models of thermoelectric devices,” *Energy Harvesting and Systems*, vol. 1 (3-4), pp. 253–265, 2014.

2 Thermoelectric materials research

2.1 Summary

This chapter exhibits the research dealing with material investigations. Doping of single-phase materials gives a possibility to adjust the thermoelectric properties of a certain material. In general, the amount of doping elements on crystallographic sites of the main phase is low if the structure is to be conserved. With increasing content of doping elements in the sol-gel batches the formation of secondary phases increases. Hence, heavy doping often leads to formation of composite materials exhibiting intergrown structures, which show compositional thermoelectric solid state properties. Therefore, the synthesis of composite materials can provide advantageous properties of the received phase composition.

Section 2.2 treats the synthesis, characterisation and theoretical description of thermoelectric n-type oxide composite materials. The applied Aluminium-doped Zinc-oxide ($\text{Zn}_{0.98}\text{Al}_{0.02}\text{O}$) exhibits a great thermopower but a very low charge carrier concentration. Therefore, a perovskite phase was integrated to provide a higher electric conductivity in the semiconducting n-type oxide-oxide composite material. Because the charge carrier concentration of ZnO is hard to increase by doping zincite-perovskite composite phases were created.

In section 2.3 $\text{Ca}_3\text{Co}_4\text{O}_9$ was synthesised and modified. In order to increase the available thermal energy density inside this layered cobaltite compound metallic Ag-inclusions were integrated and an oxide-metal composite material was received. The structures of the novel thermoelectric composite phases were investigated using X-ray and electron diffraction method and elemental mapping with energy-dispersive X-ray method. In order to increase the electric power output of the p-type composite materials, the electrical and thermal conductivity were increased. The power factor increased with increasing content of Ag in the composite materials. Applying those composite phases in thermoelectric generators made it possible to characterize a series of varied composite materials in an entire thermoelectric conversion system. The relation of electric power output and conversion efficiency was studied by measurements of the transport properties of the constructed series of generators. The output power increased with increasing silver-content, passing through a maximum value for the sample with 5% silver in the material. Hence, the determining parameter for increasing the electric power of a certain thermoelectric generator is not the figure of merit, but the power factor. Furthermore, the thermal conductivity has to exhibit a threshold value for a good balance of thermoelectric transport parameters.

2.2 Experimental and Theoretical Thermoelectric Investigations of n-type Composite Oxide Materials

Benjamin Geppert and Armin Feldhoff

Submitted to the Journal of Electroceramics (2016)

Experimental and theoretical thermoelectric investigations of n-type composite oxide materials

Benjamin Geppert and Armin Feldhoff

Thermoelectric composite materials including two different n-type semiconducting oxides were investigated. Powder products of an orthorhombic $\text{La}_{0.6}\text{Ca}_{0.4}\text{Mn}_{0.95}\text{Ni}_{0.05}\text{O}_{3-\delta}$ perovskite and a hexagonal $\text{Zn}_{0.96}\text{Al}_{0.02}\text{Cu}_{0.02}\text{O}$ zincite were mixed in three volumetric ratios of 60/40, 50/50 and 40/60, respectively. These mixed powders were sintered to ceramic composite materials. The prepared composite ceramics were investigated microstructurally and thermoelectrically. The measurement data for the thermoelectric parameters, specific isothermal electrical conductivity σ and the Seebeck coefficient α , were compared to calculated data, related to the model of parallel layers in the direction of electric current. From received measurement data for mentioned single parameters, the power factors $\sigma\alpha^2$ and the coupling factors $\sigma\alpha$ were estimated. The theoretical approaches for mixed conducting phases, based on the measurement data for the sintered single-oxide materials, were applied to discuss the relation of the composite phases' thermoelectric properties. The theoretical description bases on fluid-like quantities and classical thermodynamic potentials. From such considerations a thermoelectric material tensor has been arrived, that was extended to describe thermoelectric composite phases and match the theoretical approach to the measurement data.

Introduction

Composite materials are compounds including at least two different and separated phases. In general, compounds with very different physical properties are combined in one mixed material to get a compound with improved properties. In the field of thermoelectricity, composite oxide materials of $\text{Ca}_3\text{Co}_4\text{O}_9 - \text{La}_{0.8}\text{Sr}_{0.2}\text{CoO}_3$ were investigated^{1,2}. Furthermore, thermoelectric $\text{NaTaO}_3 - \text{Fe}_2\text{O}_3$ and $\text{NaTaO}_3 - \text{Ag}$ composite materials were studied^{3,4}. Doping is a general approach to influence the values of the specific isothermal electronic conductivity σ , the Seebeck coefficient α and the open-circuit entropy conductivity Λ . From electronic band considerations it can be seen that the specific electronic conductivity and the Seebeck coefficient are influenced counter-directly by doping. With increasing charge carrier concentration, the electronic conductivity increases whereas the Seebeck coefficient decreases⁵. Hence, composite phases are an alternative method to dope single phase materials. Another field of investigation for composite oxides is the high-temperature oxygen permeation through perovskite compounds. In such studies, one oxide with high electronic conductivity and an other with high oxygen-ionic conductivity are combined, to perform an improved mixed conduction^{6,7}.

In the present work two n-type oxide powders were mixed to form composite oxide materials. A ZnO-based phase, that crystallizes in the hexagonal zincite structure (P6₃mc, no. 186) was applied to provide a high value for the Seebeck coefficient. Investigations of the thermoelectric properties of ZnO-

based phases were done in detail⁸⁻¹⁰. For delivering a higher electronic conductivity compared with ZnO-based phases, the La-doped CaMnO_3 phase was applied, that crystallizes in the orthorhombic perovskite structure (Pnma, no. 62). The thermoelectric properties of the La-doped CaMnO_3 perovskite were also investigated¹¹. Both compounds exhibit an n-type conduction mechanism.

Theory

The physical quantities that are used to describe the thermoelectric coupling of thermoelectric materials are the potentials for entropy (i.e. absolute temperature T) and electric charge (i.e. electric potential φ) and generated flux densities for entropy \vec{j}_S and charge \vec{j}_q ^{12,13}. For the quantitative description of the thermoelectric coupling, the determining thermoelectric proportionality factors have to be known. These quantities are the specific electronic conductivity σ , the Seebeck coefficient α and the entropy conductivity Λ . The description given by Fuchs treats the transported quantities as fluid-like pumped through the established gradients of the potentials. Such approach avoids using the elaborative descriptions of the so-called thermodynamics of irreversible processes in terms of the thermoelectric effect, that has been worked out in the Onsager-De Groot-Callen model^{14,15}, based on the reciprocal relations of Onsager^{16,17}.

Equation 1 expresses the basic transport phenomenon when material i is placed in the thermodynamic potential gradients $\vec{\nabla}T$ and $\vec{\nabla}\varphi$ ^{12,13,18}.

$$\begin{pmatrix} \vec{j}_{S,i} \\ \vec{j}_{q,i} \end{pmatrix} = \begin{pmatrix} \sigma_i \alpha_i^2 + \Lambda_i & \sigma_i \alpha_i \\ \sigma_i \alpha_i & \sigma_i \end{pmatrix} \cdot \begin{pmatrix} -\vec{\nabla}T \\ -\vec{\nabla}\varphi \end{pmatrix} \quad (1)$$

Considering a composite material made of two different thermoelectric materials ($i = 1, 2$) with thermal and electrical parallel connection, like in the case of parallel plates sketched in Figure 1a, the currents of entropy and charge through materials 1 and 2 add to each other, respectively. Hence, the flux densities of entropy \vec{j}_S and charge \vec{j}_q for the composite material are obtained as follows in Equation 2 with f_i ($\sum f_i = 1$) being the specific volumetric fractions of the two different materials.

$$\begin{pmatrix} \vec{j}_{S,comp} \\ \vec{j}_{q,comp} \end{pmatrix} = f_1 \begin{pmatrix} \vec{j}_{S,1} \\ \vec{j}_{q,1} \end{pmatrix} + f_2 \begin{pmatrix} \vec{j}_{S,2} \\ \vec{j}_{q,2} \end{pmatrix} = \begin{pmatrix} (f_1 \sigma_1 \alpha_1^2 + f_2 \sigma_2 \alpha_2^2) + (f_1 \Lambda_1) + (f_2 \Lambda_2) & (f_1 \sigma_1 \alpha_1) + (f_2 \sigma_2 \alpha_2) \\ (f_1 \sigma_1 \alpha_1) + (f_2 \sigma_2 \alpha_2) & (f_1 \sigma_1) + (f_2 \sigma_2) \end{pmatrix} \cdot \begin{pmatrix} -\vec{\nabla}T \\ -\vec{\nabla}\varphi \end{pmatrix} \quad (2)$$

Under isothermal conditions ($\vec{\nabla}T = 0$), Ohm's law for the composite material is obtained by Equation 3.

$$\vec{j}_{q,comp} = f_1 \cdot \vec{j}_{q,1} + f_2 \cdot \vec{j}_{q,2} = [f_1 \sigma_1 + f_2 \sigma_2](-\vec{\nabla}\varphi) = \sigma_{comp}(-\vec{\nabla}\varphi) \quad (3)$$

The isothermal specific electronic conductivity of the composite σ_{comp} can be identified as shown in 4.

$$\sigma_{comp} = f_1 \sigma_1 + f_2 \sigma_2 = (f\sigma)_1 + (f\sigma)_2 \quad (4)$$

Under electrically open-circuited condition (i.e. $\vec{j}_{q,i} = 0$), Equation 5 is obtained.

$$0 = [f_1 \sigma_1 \alpha_1 + f_2 \sigma_2 \alpha_2](\vec{\nabla}T) + [f_1 \sigma_1 + f_2 \sigma_2](\vec{\nabla}\varphi) \quad (5)$$

Here, the composite material couples the gradients of the entropy potential T and the electric potential φ according to Equation 6.

$$\vec{\nabla}\varphi = -\frac{f_1 \sigma_1 \alpha_1 + f_2 \sigma_2 \alpha_2}{f_1 \sigma_1 + f_2 \sigma_2}(\vec{\nabla}T) = -\alpha_{comp}(\vec{\nabla}T) \quad (6)$$

In analogy to a single-phase material¹⁸, the composite Seebeck coefficient α_{comp} is easily identified by Equation 7:

$$\alpha_{comp} = \frac{f_1 \sigma_1 \alpha_1 + f_2 \sigma_2 \alpha_2}{f_1 \sigma_1 + f_2 \sigma_2} = \frac{(f\sigma\alpha)_1 + (f\sigma\alpha)_2}{(f\sigma)_1 + (f\sigma)_2} \quad (7)$$

To consider the entire connectivity of the composite model system, a factor X is introduced to give the possibility to include the network properties in the model description. The modification for the model of ideal parallel conduction channels in terms of mixing materials with very different electric conductivities is shown in Figure 1. The electric conductivity of material 2 is negligible small compared to that of material 1. The charge carriers can only pass the material through the conduction channels. When the channel is blocked, the respective partial electric current gives no addition to the entire electric current inside the composite material. The amount of uninterrupted conduction channels in a real macroscopic composite material is lower than 100% ($X = 1$). Considering this situation, the correction factor X must exhibit values in the range $0 < X < 1$. The introduced factor X will be used in later sections.

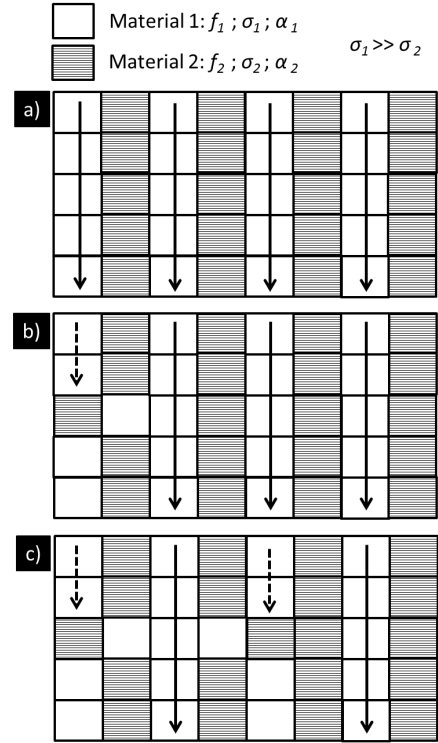


Fig. 1 Schematic illustration of the model for a binary mixture of 50/50 composition with vertically aligned parallel layers of an electrically conducting (1) and an electrically isolating (2) material parallel to the direction of electric flux (solid arrows: uninterrupted conduction channels; dashed arrows: interrupted conduction channels). a) All conduction channels are open: $X = 1$, b) conduction channels are partly interrupted: $X = 0.75$, c) half of the conduction channels are interrupted: $X = 0.5$

Experimental

Synthesis and preparation of materials

Powders of n-type zincite (nominal composition $\text{Zn}_{0.96}\text{Al}_{0.02}\text{Cu}_{0.02}\text{O}$) and perovskite (nominal composition $\text{La}_{0.6}\text{Ca}_{0.4}\text{Mn}_{0.95}\text{Ni}_{0.05}\text{O}_{3-\delta}$) thermoelectric materials were synthesised by a sol-gel route¹⁹. The nitrates of respective metal cations were stoichiometrically added to an aqueous ammonia solution of pH = 9 containing citric acid and ethylenediaminetetraacetic acid (EDTA) for complexing the soluted metal ions. The obtained precipitates were calcinated at 1223 K for 10 h with a heating and cooling rate of $3 \text{ K} \cdot \text{min}^{-1}$. After calcination, the powder products were cold-pressed and sintered at 1573 K for 10 h with a heating and cooling rate of $2 \text{ K} \cdot \text{min}^{-1}$.

For preparation of the composite phases, powder products, that were obtained by calcination of the perovskite phase and the zincite phase, were mixed by sonication in ethanol. The two different structures were mixed in three different volumetric ratios 60/40, 50/50 and 40/60, respectively.

Microstructure analysis

The materials were analyzed using field-emission scanning electron microscopy (FE-SEM) using a JEOL JSM-6700F, equipped with an Oxford Instruments INCA 300 energy-dispersive X-ray spectrometer (EDXS) for elemental analysis. The phase composition of calcined powder product and sintered ceramic of both, single oxide materials and dual-phase oxide materials, were analyzed by X-ray diffraction (XRD) using a Bruker D8 Advance with $\text{Cu-K}\alpha$ radiation. The obtained diffraction data were refined by Rietveld refinement in the TOPAS 4.1 software. The reference data for the crystal structure analysis were taken from the Powder Diffraction File (PDF2) database.

Thermoelectric analysis

To characterize the thermoelectric properties of the materials, the temperature-dependent isothermal specific electric conductivity $\sigma(T)$ and the Seebeck coefficient $\alpha(T)$, as estimated from the thermovoltage, were measured. Using these data the power factor $\sigma\alpha^2$ and the coupling parameter $\sigma\alpha$, describing the entropy conduction coupled to the electric phenomenon, were estimated for each compound. A precision vertical diamond wire-saw, model 3242 from O'WELL, was used for sample preparation. Thermoelectric properties were measured using a measurement cell constructed in-house that is a modified version of the arrangement described by Indris et al.²⁰. The sample was clamped between two platinum electrodes to close the electric circuit in a pseudo-four-point measurement. The applied furnace was an ELITE thermal system (300-1473 K). The electronic parameters were measured with KEITHLEY 2100 $6\frac{1}{2}$ Digit Multimeters. Data were acquired and converted using the LAB VIEW software.

Results and discussion

Single materials

The perovskite phase (material 1) was analyzed by SEM and XRD method for structure determination. In Figure 2a-c, scanning electron micrographs and an EDX spectrum of the surface of $\text{La}_{0.6}\text{Ca}_{0.4}\text{Mn}_{0.95}\text{Ni}_{0.05}\text{O}_{3-\delta}$ are presented.

The surface of $\text{La}_{0.6}\text{Ca}_{0.4}\text{Mn}_{0.95}\text{Ni}_{0.05}\text{O}_{3-\delta}$ sample exhibits grain sizes in the 1-2 μm range. Compared to the ZnO-based ceramic the grain sizes in the perovskite sample are ten times smaller. Furthermore, some Ca-rich phase was formed on the surfaces of the perovskite compound. In Figure 2b, the CaO formations on the surface of the $\text{La}_{0.6}\text{Ca}_{0.4}\text{Mn}_{0.95}\text{Ni}_{0.05}\text{O}_{3-\delta}$ perovskite can be seen. In the diffraction patterns of Figure 2c, the X-ray reflections caused by the exsolved CaO on the ceramic surfaces are marked with asterisks.

Figure 3 shows SEM micrographs, EDXS and XRD results of the ZnO-based ceramic. The micrograph of the sintered $\text{Zn}_{0.96}\text{Al}_{0.02}\text{Cu}_{0.02}\text{O}$ surface exhibits grain sizes that are in the 5-20 μm range. The surface of $\text{Zn}_{0.96}\text{Al}_{0.02}\text{Cu}_{0.02}\text{O}$ ceramic material is dense and shows no remaining porosity. On the surface and inside the bulk phase of $\text{Zn}_{0.96}\text{Al}_{0.02}\text{Cu}_{0.02}\text{O}$, spinel formation is present to similar amounts. Figure 3c shows the results of the compositional analysis of $\text{Zn}_{0.96}\text{Al}_{0.02}\text{Cu}_{0.02}\text{O}$ material. Because Al_2O_3 particles were used for vibration-polishing, the Al signal cannot be discussed quantitatively. Due to stoichiometric inhomogeneity of the zincite phase the soluted contents of the doping elements Al and Cu cannot be determined.

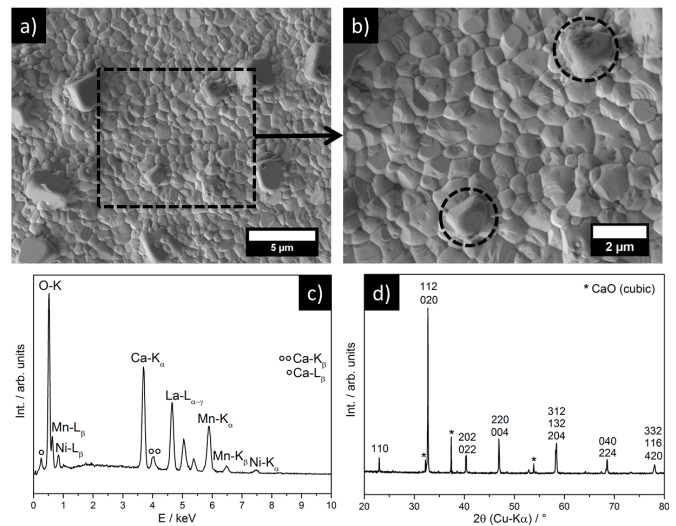


Fig. 2 Secondary electron micrographs of $\text{La}_{0.6}\text{Ca}_{0.4}\text{Mn}_{0.95}\text{Ni}_{0.05}\text{O}_{3-\delta}$ perovskite ceramic. a) surface view, b) magnified surface view (dashed rectangular in a) with CaO formations (dashed circles), c) EDX spectrum of the surface, d) XRD pattern of the surface indexed according to orthorhombic perovskite structure.

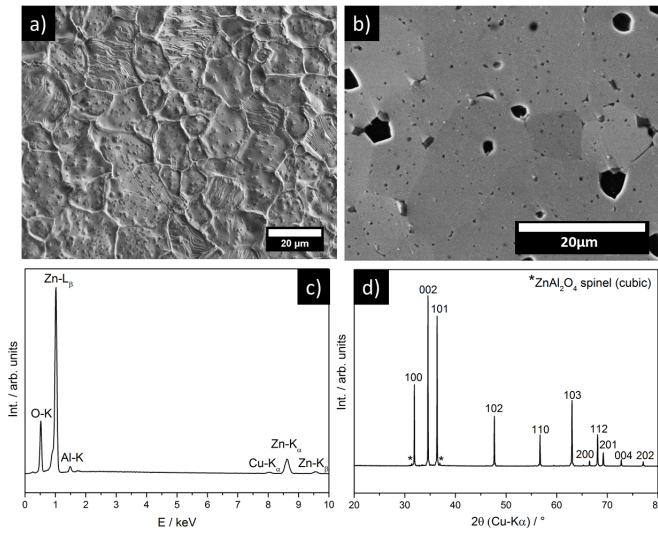


Fig. 3 Secondary electron micrographs of $\text{Zn}_{0.96}\text{Al}_{0.02}\text{Cu}_{0.02}\text{O}$ zincite ceramic: a) surface view, b) vibration-polished bulk. c) EDX spectrum of surface, d) XRD pattern of surface indexed according to hexagonal zincite structure. Asterisks mark reflections of cubic ZnAl_2O_4 spinel inclusions.

Anyway, the real composition deviates from the nominal composition and is rather $\text{Zn}_{1-(x+y)}\text{Al}_x\text{Cu}_y\text{O}$ with ZnAl_2O_4 inclusions. The separated phase inside the matrix of the ZnO-based compound is ZnAl_2O_4 spinel, that was also determined by Schäuble et al.¹⁰. The $\text{Zn}_{0.96}\text{Al}_{0.02}\text{Cu}_{0.02}\text{O}$ ceramic material exhibits the hexagonal zincite structure, see Figure 3d. For investigating the thermoelectric properties of the ZnO zincite and the $\text{La}_{0.6}\text{Ca}_{0.4}\text{Mn}_{0.95}\text{Ni}_{0.05}\text{O}_{3-\delta}$ perovskite materials the isothermal specific electric conductivity σ_i and the Seebeck coefficient α_i were measured. From the estimated values of mentioned quantities the coupling parameter $(\sigma\alpha)_i$ and the power factor $(\sigma\alpha^2)_i$ were calculated. Figure 4 shows the assembled measurement data describing the thermoelectric properties of synthesized ceramic single materials.

The high charge carrier density of the perovskite causes a electronic conductivity that is more than five times of that of the zincite phase. Due to the high carrier concentration the value of the Seebeck coefficient (entropy per unit charge transferred) is only one-hundredth of the value exhibiting by the zincite phase.

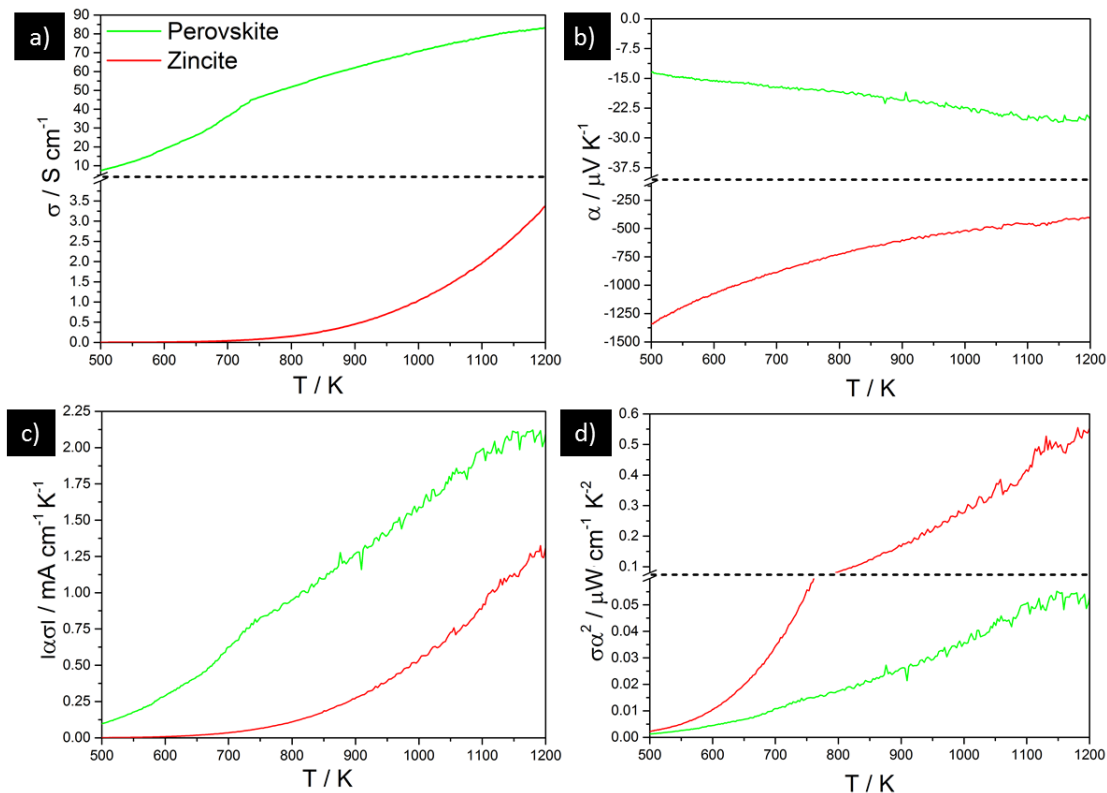


Fig. 4 Measured thermoelectric properties of studied oxide systems: a) isothermal specific electric conductivity, b) Seebeck coefficient, c) coupling factor, d) power factor. Horizontal dashed lines mark break of vertical scale; the legend for all subfigures is displayed in subfigure a.

Composite materials

The ceramic materials, i.e. the zincite and the perovskite materials were obtained as thermomechanically stable phases. For preparing composite materials from the synthesized single materials, the oxide powders of $\text{La}_{0.6}\text{Ca}_{0.4}\text{Mn}_{0.95}\text{Ni}_{0.05}\text{O}_{3-\delta}$ and $\text{Zn}_{0.96}\text{Al}_{0.02}\text{Cu}_{0.02}\text{O}$ were mixed in volumetric ratios of 60/40, 50/50 and 40/60, respectively. The structures of the sintered composite oxides were analyzed by X-ray diffraction. The diffraction data were refined with the Rietveld method to calculate the volumetric ratios of the mixed oxide phases. No third phase as result of reaction (interdiffusion) in the grain boundaries of the grains of the two different oxide phases was observed. In Figure 5, the X-ray diffraction patterns of the mixed oxide composite materials are presented together with Rietveld fits. The volumetric ratios obtained by the Rietveld refinement are in good agreement with the batched mixed oxide phases. No reaction between the different phases was observed. In Table 1, the refined crystallographic parameters of the composite oxide materials are summarized. The lattice parameters of the single phases in the composite materials are as expected and show almost independent values from volumetric ratios.

Table 1 Results of the Rietveld refinement referring to measured X-ray diffraction data and the volumetric ratios of mixed oxide phases with considered single phases of perovskite (Pnma; ICSD 51161) and zincite ($\text{P6}_3\text{mc}$; ICSD 26170).

sample	phase	$a / \text{\AA}$	$b / \text{\AA}$	$c / \text{\AA}$	$f / \text{vol.}\%$
40/60 composite	perovskite	5.471	7.700	5.441	40.60
	zincite	3.256	3.256	5.208	59.40
50/50 composite	perovskite	5.438	7.695	5.439	47.00
	zincite	3.254	3.254	5.205	53.00
60/40 composite	perovskite	5.444	7.700	5.441	59.27
	zincite	3.254	3.254	5.203	40.73

The refined volumetric ratios match to the batched ones with mismatches in the range of 1–3 %. The fits that were received performing the Rietveld refinement give results with acceptable accuracy. The 50/50 composite show the largest mismatch between batched and refined phase fractions. In Table 2, the fitting parameters are assembled for the three different composite oxides. For the meaning of the specific residuals²¹.

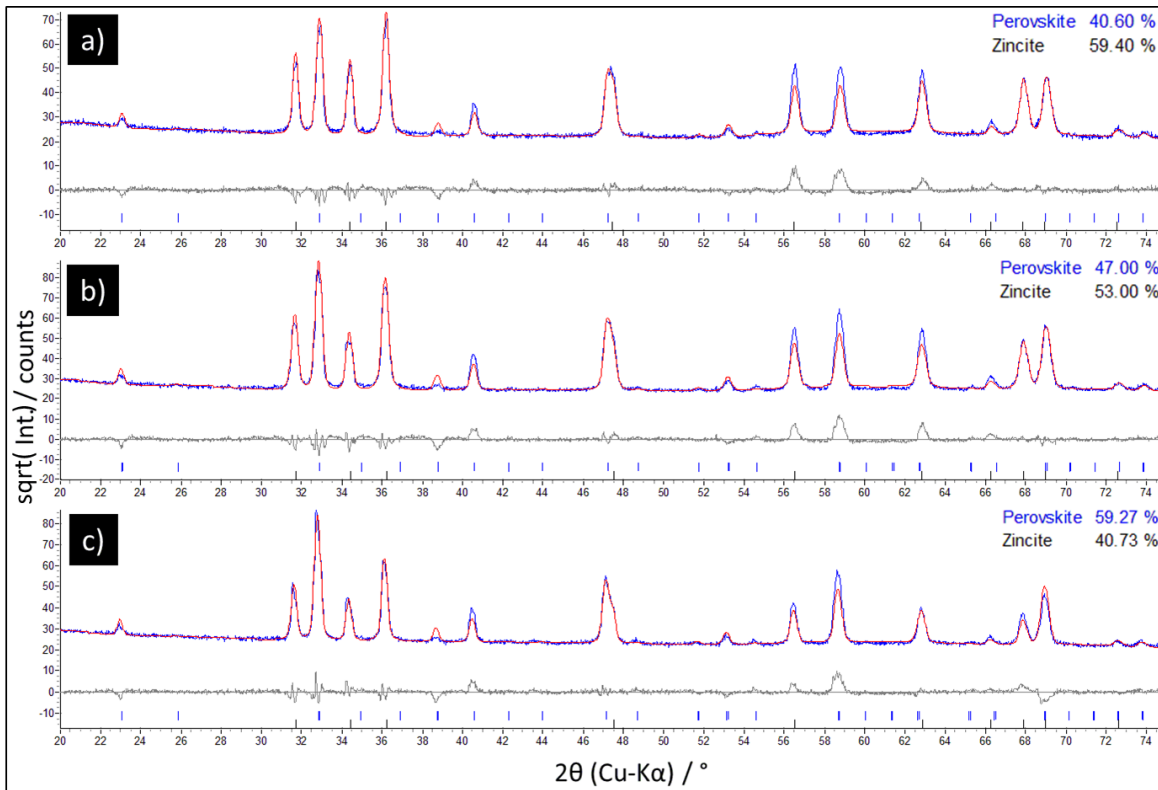


Fig. 5 X-ray diffractograms of the crushed sintered ceramic composite materials with blue curves for measured diffractograms, red curves for the Rietveld fits and grey differential curves. The intensities are shown as square root-values (\sqrt{I}). a) 40/60 composition, b) 50/50 composition, c) 60/40 composition.

Table 2 Values for specific residuals R as indicators of the goodness of fit (GOF) of the Rietveld refinements.

sample	R_{exp}	R_{wp}	GOF	phase	R_{Bragg}
40/60 composite	3.70	10.64	2.88	perovskite	9.025
				zincite	7.045
50/50 composite	3.32	11.55	3.48	perovskite	10.026
				zincite	6.872
60/40 composite	3.64	10.52	2.89	perovskite	8.682
				zincite	4.516

In Figure 6, the results of SEM with EDXS of the 50/50 composite material are shown exemplarily. In Figure 6a,c the cross-section of a typical site inside the composite bulk material is presented.

A homogeneous distribution of the two different oxide phases was observed. The SEM and EDXS results confirm those of the XRD analysis in a way that no third phase was detected. In Figure 6b, a typical site of the surface structure of the ceramic composite material exhibits also a homogeneous distribution of the two different oxide phases. The EDX spectrum in Figure 6d shows both single oxide phases with percolation network in the composite material without showing any other phases in between. The spectrum of the composite materials are received as sum of the spectra of the single oxide phases that are shown in Figure 3c for the zincite phase and in Figure 2c for the perovskite phase.

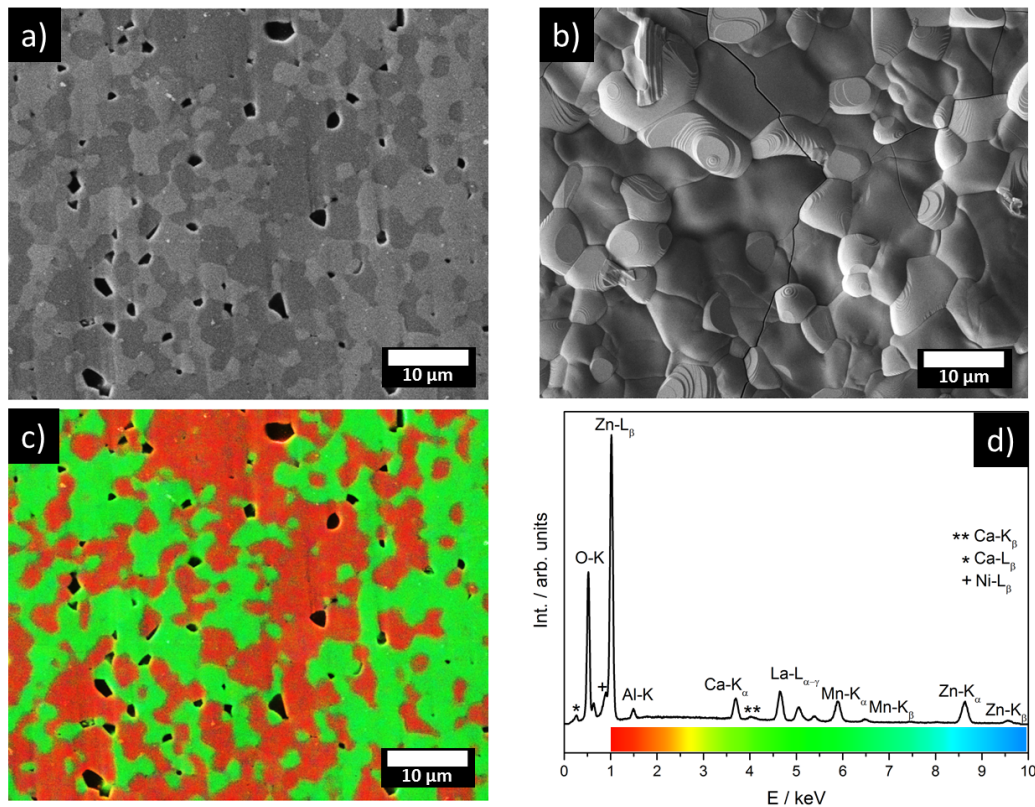


Fig. 6 Scanning electron microscope analysis of the prepared 50/50 composite material. a) polished ceramic bulk phase, b) surface of ceramic bulk phase, c) pseudocolor-micrograph of polished ceramic bulk phase, d) EDX spectrum of the composite material with relation between the specific energy-lines and applied pseudo-colors.

The thermoelectric properties of the composite materials were measured as it was done for the single oxide materials. The isothermal electric conductivities σ , the Seebeck coefficients α , the power factors $\sigma\alpha^2$ and the coupling parameters $\alpha\sigma$ of the composite materials are assembled in Figure 7.

As it was expected, the composite materials exhibit values of measured quantities that are in between those of the single oxide materials. Whereas specific electric conductivities of the composite materials depend clearly on the batched fractions of single oxide materials whereas the absolute values of the Seebeck coefficients weakly depend on the batched fractions. However, there is a dependence of the batched ratios of respective oxide phases to the value of the Seebeck coefficient. In the range of 900 K, see Figure 7, the values of α for the different compositions are equal.

Below this temperature the Seebeck coefficients are proportional to the fraction of the perovskite phase, whereas the values of α for temperatures above 900 K are proportional to the zincite fraction of the composite materials. Above 900 K, the charge carriers related to the zincite phase seem to start to determine the thermoelectric properties of the composite materials, that causes a rapid rise of the values for α . With decreasing temperature the values of the Seebeck coefficients of the composite phases are almost independent of the temperature. In the 500-650 K range, the coupling parameter $\sigma\alpha$ and the power factor $\sigma\alpha^2$ of the 60/40 composite exhibit higher values than those of the single materials. The dashed rectangulars in Figure 7c,d mark the mentioned temperature range.

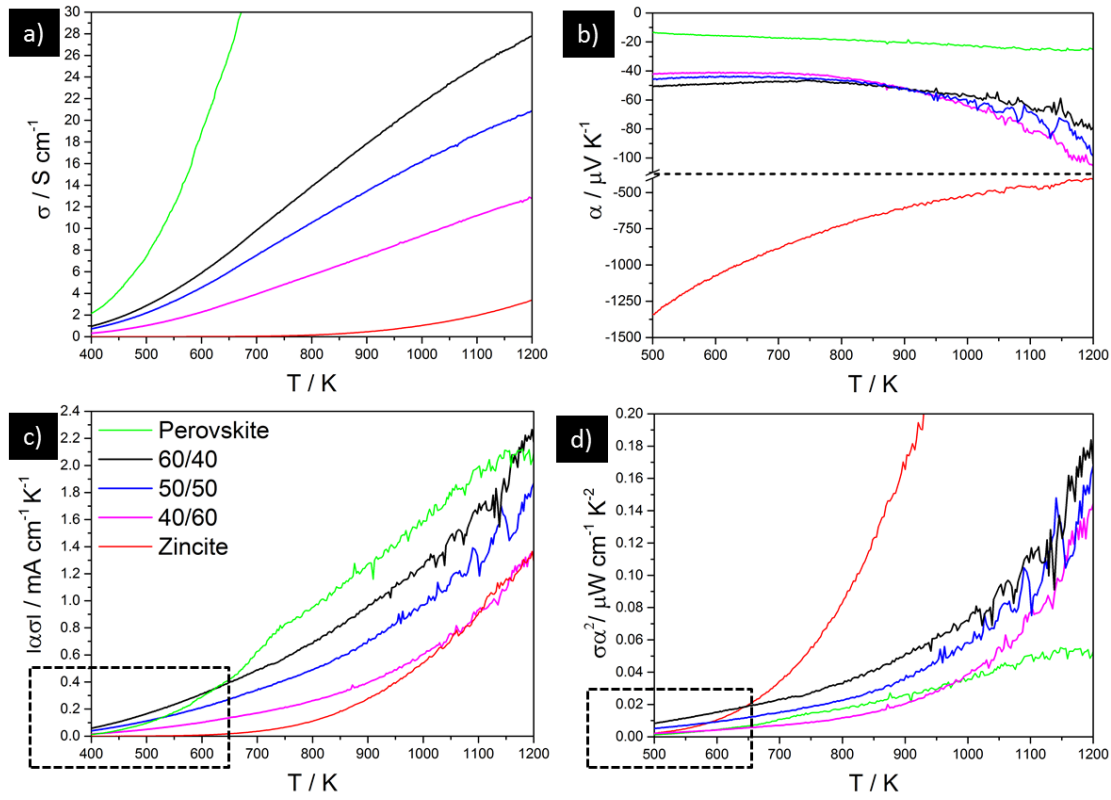


Fig. 7 Thermoelectric properties of the composite material with displayed properties of the composite building single phases: a) specific isothermal conductivities, b) Seebeck coefficients, c) coupling parameter $\sigma\alpha$ d) power factor $\sigma\alpha^2$. Vertical dashed lines mark break of scale; the legend for all subfigures is displayed in subfigure c.

To calculate the specific electrical conductivities of the composite materials from the values of the single-phase $\text{La}_{0.6}\text{Ca}_{0.4}\text{Mn}_{0.95}\text{Ni}_{0.05}\text{O}_{3-\delta}$ perovskite with fractions $f_1 = f_{\text{perovskite}}$ and $\text{Zn}_{0.96}\text{Al}_{0.02}\text{Cu}_{0.02}\text{O}$ zincite with fractions $f_2 = f_{\text{zincite}}$ in the mixed materials, the estimated factor X was considered. Equation 8 was used to calculate the values for specific electrical conductivities of the composite phases from the measurement data for electrical conductivity of the single perovskite material $\text{La}_{0.6}\text{Ca}_{0.4}\text{Mn}_{0.95}\text{Ni}_{0.05}\text{O}_{3-\delta}$.

$$\sigma_{\text{comp}} = [(f\sigma)_1 + (f\sigma)_2] \cdot X \quad (8)$$

The calculations were executed with the three fractions of the perovskite phase $f_1 = f_{\text{perovskite}} = 0.6, 0.5, 0.4$ and of the zincite phase $f_2 = f_{\text{zincite}} = 0.4, 0.5, 0.6$ for the respective composites 60/40, 50/50 and 40/60. The introduced factor was set to the value of $X = 0.48$ to match the calculated data to measured values. The calculated values of the specific electrical conductivities of the composites are presented in Figure 8.

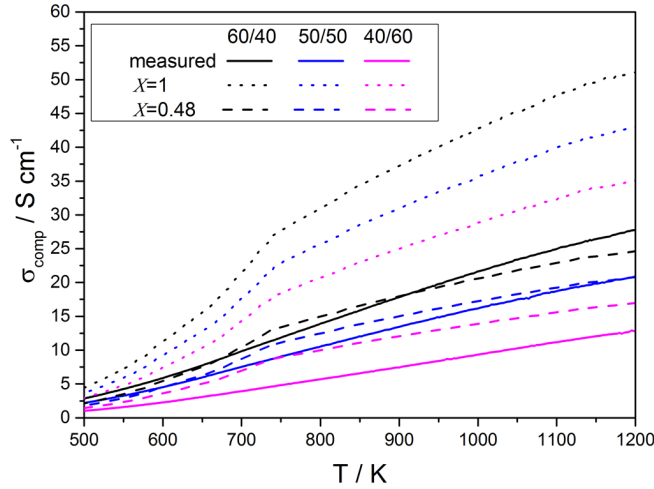


Fig. 8 Measured specific electric conductivities of the composite materials with calculated curves for respective fractional compositions with $X = 1$ and $X = 0.48$ (see Equation 8).

For the 50/50 composition, the match between the measured data and the calculated data for electrical conductivity give the best results. For the 60/40 composition the calculated data lie to low in the 1000-1200 K temperature range. Introducing the modified expression for calculating the electric conductivity, Equation 9, showing the relation for the composite Seebeck coefficient, is obtained.

$$\alpha_{\text{comp}} = \left(\frac{(f\sigma\alpha)_1 + (f\sigma\alpha)_2}{(f\sigma)_1 + (f\sigma)_2} \right) \cdot \frac{1}{X} \quad (9)$$

The assembled measurement data for the Seebeck coefficients of the respective composites and the calculated values that were determined using Equation 9 with measurement data for the single oxide materials are presented in Figure 9.

The calculated curves were matched to the measured curves with the factor $X = 0.48$ that was estimated from the matching of

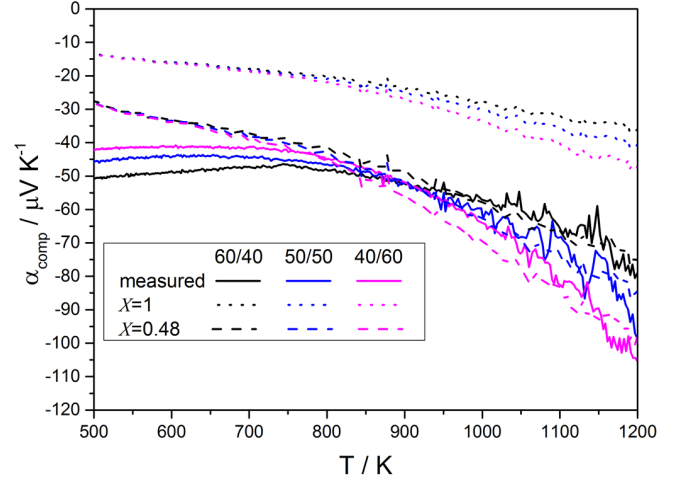


Fig. 9 Measured Seebeck coefficients of the respective composite materials with calculated curves (according to Equation 9).

measured and calculated values for the specific electric conductivity. In the temperature range above 900 K the calculated values of the Seebeck coefficients are in the range that is exhibited by the measurement data. With decreasing temperature, starting at 900 K, the fits get worse due to the rapid drop down of calculated values. For the 60/40 composite the calculated values are too low while the calculated values for the 40/60 composition are too high and nearly reach those of the 50/50 composition.

Equation 10 shows that only the coupling factor for the composites $(\sigma\alpha)_{\text{comp}}$ can be expressed by the single parameters of electric conductivity and Seebeck coefficient with respect to the fractions of the composite building materials without considering the network properties of the composite material.

$$(\sigma\alpha)_{\text{comp}} = (f\sigma\alpha)_1 + (f\sigma\alpha)_2 \quad (10)$$

Figure 10 shows the calculation results, according to Equation 10, compared to the measurement values for the coupling parameter $(\sigma\alpha)_{\text{comp}}$ of respective compositions. Here, the results for the 50/50 composition give the best match of measured and calculated values.

Assuming that the thermoelectric parameters for the composite materials can be expressed by the parameters of the single materials as it is derived in Equation 10, the transport equation describing the entire thermoelectric coupling phenomenon for the composites, the material tensor can be rewritten by using Equation 2. The modified transport equation for describing the thermoelectric properties of the oxide composite materials, considering the percolation network using the factor X , is shown in Equation 11.

$$\begin{pmatrix} \vec{J}_{S,\text{comp}} \\ \vec{J}_{q,\text{comp}} \end{pmatrix} = \begin{pmatrix} (f\sigma\alpha^2)_1 + (f\sigma\alpha^2)_2 + (f\Lambda)_1 + (f\Lambda)_2 & (f\sigma\alpha)_1 + (f\sigma\alpha)_2 \\ (f\sigma\alpha)_1 + (f\sigma\alpha)_2 & [(f\sigma)_1 + (f\sigma)_2] \cdot X \end{pmatrix} \cdot \begin{pmatrix} -\vec{\nabla}T \\ -\vec{\nabla}\varphi \end{pmatrix} \quad (11)$$

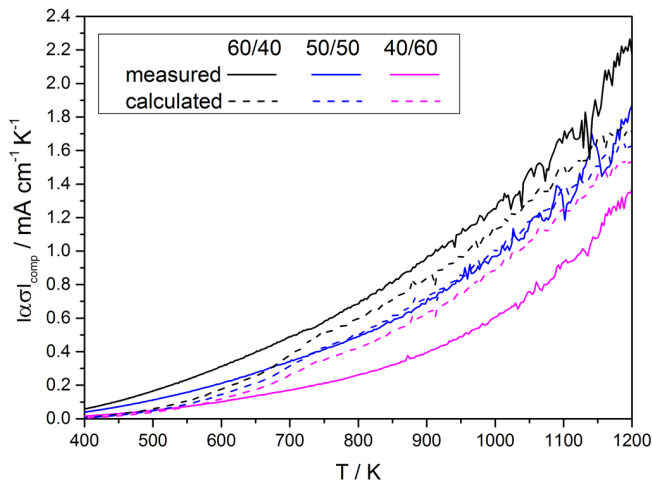


Fig. 10 Measured coupling factors of the composite materials with calculated curves for respective fractional compositions of the oxide materials (see Equation 10).

Compared to the idealized composite (i.e. parallel plates) described by Equation 2, the modified material tensor in Equation 11 considers the properties of the composite network. For the 50/50 composition the calculations are in good agreement with the measurement data. With increasing deviation from the 50/50 ratio in both directions the calculation results get worse.

Conclusions

Composite oxide materials, made from the $\text{La}_{0.6}\text{Ca}_{0.4}\text{Mn}_{0.95}\text{Ni}_{0.05}\text{O}_{3-\delta}$ perovskite phase and the $\text{Zn}_{0.96}\text{Al}_{0.02}\text{Cu}_{0.02}\text{O}$ zincite phase, were successfully synthesised in volumetric ratios of 60/40, 50/50 and 40/60, respectively. Sintered oxide bulk composites were obtained as thermally and mechanically stable materials. The values for electric conductivity σ_{comp} of the composite materials are in between of those measured for the single oxide materials. For lower temperatures the values of σ_{comp} are closer to those of the $\text{La}_{0.6}\text{Ca}_{0.4}\text{Mn}_{0.95}\text{Ni}_{0.05}\text{O}_{3-\delta}$ perovskite. The values for the Seebeck coefficient α_{comp} of the composites are closer to that one measured for the $\text{La}_{0.6}\text{Ca}_{0.4}\text{Mn}_{0.95}\text{Ni}_{0.05}\text{O}_{3-\delta}$ perovskite related to the entire temperature range. The batched fractions of mixed perovskite and zincite phases were confirmed by the Rietveld refinement of measured X-ray diffraction patterns.

The measured data for the Seebeck coefficients of the composites were compared to calculated data received from the theoretical approach related to the thermoelectric properties of different materials with specific properties of charge carriers (see Equations 7 and 9). A model for parallel plates of the two materials in direction of electric current was applied. Besides the thermoelectric parameters σ_i , α_i and the fractions f_i of the single oxide materials a percolation factor X was introduced to enable describing the percolation network. The calculated values of the composite Seebeck coefficient α_{comp} for the non-modified expression ($X = 1$) are approximately half of the measured values. The absolute values of the curve was fitted to the measured data with

a factor $X = 0.48$, that occur in the formula for the composite Seebeck coefficient α_{comp} in a reciprocal way. The introduced factor X gives a correlation for the Seebeck coefficient and the electrical conductivity, and it is, in our opinion, useful to describe the network properties inside composite oxide materials in a simple way. For ideal percolation of each of the different materials, the mixed conducting material is obtained as homogeneous single phase and the factor X equals unity ($X = 1$). In real composite systems, where inhomogeneities will cause partly interrupted electric conductivity paths, a decreases percolation factor X results, which is then smaller than unity (i.e. $X < 1$). It turned out, that the coupling factor $\sigma\alpha$ can be expressed without considering the percolation network. For the 50/50 composite, the calculation results give the best matches of measured and calculated data. Besides doping of extrinsic elements on specific sites of a certain single material, the production of composite materials can also be used to adjust the charge carrier concentration of thermoelectric material systems. So, there is an additional opportunity to modify thermoelectric material systems. Therefore, cheap materials like ZnO can be mixed up with phases including more expensive elements in order to reduce the costs of the entire thermoelectric material.

References

- 1 S. Butt, W. Xu, M. Farooq, G. Ren, F. Mohamed, Y. Lin and C. Nan, *Journal of American Ceramic Society*, 2015, **98(4)**, 1230–1235.
- 2 Y. Lin, C. Norman, D. Srivasta, F. Azough, L. Wang, M. Robbins, K. Simpson, R. Freer and I. Kinloch, *Applied Materials and Interfaces*, 2015, **7(38)**, 15898–15908.
- 3 W. Wunderlich, *Journal of Nuclear Materials*, 2009, **389**, 57–61.
- 4 W. Wunderlich, *Materials for Renewable and Sustainable Energy*, 2014, **3(21)**, 1–6.
- 5 A. Ioffe, *Semiconductor Thermoelements and Thermoelectric cooling*, Infosearch Ltd. London, 1st edn, 1957, p. 96.
- 6 W. Fang, F. Liang, Z. Cao, F. Steinbach and A. Feldhoff, *Angewandte Chemie*, 2015, **54**, 4847–4850.
- 7 H. Luo, K. Efimov, H. Jiang, A. Feldhoff, H. Wang and J. Caro, *Angewandte Chemie*, 2011, **50**, 759–763.
- 8 M. Ohtaki, T. Tsubota, K. Egushi and H. Arai, *Journal of Applied Physics*, 1996, **79(3)**, 1819–1818.
- 9 M. Ohtaki, *Journal of the Ceramic Society of Japan*, 2011, **119**, 770–775.
- 10 N. Schäuble, B. Süess, S. Populoh, A. Weidenkaff and M. Aguirre, *European Conference on Thermoelectrics*, 2012, **9**, 422–424.
- 11 A. Weidenkaff, R. Robert, M. Aguirre, L. Bocher, T. Lippert and S. Canulescu, *Renewable Energy*, 2007, **33**, 342–347.
- 12 H. Fuchs, *The Dynamics of Heat – A Unified Approach to Thermodynamics and Heat Transfer*, Springer, New York, 2nd edn, 2010, pp. 104 + 169 + 562.
- 13 H. Fuchs, *Energy Harvesting and Systems*, 2014, **1(3-4)**, 253–265.
- 14 H. Callen, *Physical Review*, 1948, **73**, 1349–1358.

- 15 S. de Groot, *Thermodynamics of irreversible processes*, North-Holland, Amsterdam, NL, 2010, pp. 141–162.
- 16 L. Onsager, *Physical Review*, 1931, **37**, 405–426.
- 17 L. Onsager, *Physical Review*, 1931, **38**, 2265–2279.
- 18 A. Feldhoff, *Energy Harvesting and Systems*, 2015, **2(1)**, 5–13.
- 19 A. Feldhoff, M. Arnold, J. Martynczuk, T. Gesing and H. Wang, *Solid State Sciences*, 2008, **10**, 689–701.
- 20 S. Indris, *Perkolation von Grenzflächen in nanokristallinen keramischen Kompositen - Li-Ionenleitfähigkeit und ⁷Li-NMR-Relaxation*, Cuvillier Verlag, Göttingen, DE, 2001, pp. 40–42.
- 21 R. Young, *Introduction to the Rietveld method*, Oxford University Press, Oxford, 1993, pp. 1–39.

2.3 Enhanced Flexible Thermoelectric Generators based on Oxide-Metal Composite Materials

Benjamin Geppert, Artur Brittner, Lailah Helmich,

Michael Bittner and Armin Feldhoff

Journal of Electronic Materials, DOI:10.1007/s11664-017-5281-7, (2016)



Enhanced Flexible Thermoelectric Generators Based on Oxide–Metal Composite Materials

BENJAMIN GEPPERT,^{1,2} ARTUR BRITTNER,^{1,3} LAILAH HELMICH,^{1,4}
 MICHAEL BITTNER,^{1,5} and ARMIN FELDHOFF^{1,6}

1.—Institute of Physical Chemistry and Electrochemistry, Leibniz Universität, Callinstraße 3A, 30167 Hannover, Lower Saxony, Germany. 2.—e-mail: benjamin.geppert@pci.uni-hannover.de. 3.—e-mail: artur.brittner@gmail.com. 4.—e-mail: lailah.helmich@web.de. 5.—e-mail: michael.bittner@pci.uni-hannover.de. 6.—e-mail: armin.feldhoff@pci.uni-hannover.de

The thermoelectric performance of flexible thermoelectric generator stripes was investigated in terms of different material combinations. The thermoelectric generators were constructed using Cu–Ni–Mn alloy as *n*-type legs while varying the *p*-type leg material by including a metallic silver phase and an oxidic copper phase. For the synthesis of Ca₃Co₄O₉/CuO/Ag ceramic-based composite materials, silver and the copper were added to the sol–gel batches in the form of nitrates. For both additional elements, the isothermal specific electronic conductivity increases with increasing amounts of Ag and CuO in the samples. The amounts for Ag and Cu were 0 mol.%, 2 mol.%, 5 mol.%, 10 mol.%, and 20 mol.%. The phases were confirmed by x-ray diffraction. Furthermore, secondary electron microscopy including energy dispersive x-ray spectroscopy were processed in the scanning electron microscope and the transmission electron microscope. For each *p*-type material, the data for the thermoelectric parameters, isothermal specific electronic conductivity σ and the Seebeck coefficient α , were determined. The *p*-type material with a content of 5 mol.% Ag and Cu exhibited a local maximum of the power factor and led to the generator with the highest electric power output P_{el} .

Key words: Flexible thermoelectric generators, composite materials, energy conversion, electric power output, conversion efficiency

INTRODUCTION

The possibility of local and individual applications and portability of energy conversion systems are receiving increasing interest. Here, the thermoelectric effect can be used to develop small and handy devices for the conversion of waste heat into useful electricity. The crucial quantities in determining the thermoelectric properties of a material are the isothermal ($\Delta T = 0$) specific electric conductivity σ , the Seebeck coefficient α (from the thermovoltage) and the specific entropy conductivity Λ in electric open-circuit conditions ($I_{el} = 0$).^{1–3} The coupled potential drops for entropy ΔT and charge $\Delta\varphi = U$, namely the generated voltage, and the related generated entropy current I_S

and charge current I_{el} , can be quantitatively described in terms of thermoelectric quantities, considering a thermoelectric material tensor that includes all the measurable thermoelectric properties that determine the thermoelectric performance of a particular material. The transport equation describing the entire thermoelectric effect is shown in Eq. 1^{4,5}:

$$\begin{pmatrix} I_S \\ I_{el} \end{pmatrix} = -\frac{A_{leg}}{L_{leg}} \cdot \begin{pmatrix} \sigma\alpha^2 + \Lambda & \sigma\alpha \\ \sigma\alpha & \sigma \end{pmatrix} \cdot \begin{pmatrix} \Delta T \\ \Delta\varphi \end{pmatrix} \quad (1)$$

A_{leg} is the cross-sectional area and L_{leg} the length of bar-shaped material legs. The heat conductivity in open-circuit conditions λ is related to the entropy conductivity Λ via the absolute working temperature, T , as shown in Eq. 2.⁶

(Received September 26, 2016; accepted January 1, 2017)

Published online: 27 January 2017

$$\lambda = T \cdot \Lambda \quad (2)$$

In addition to trying to apply certain materials to certain temperature conditions, the geometric properties of a complete thermoelectric generator (TEG) must be considered. The construction of a TEG requires an electric series connection of a hole conductor ($\alpha > 0$, p -type), where the motions of thermal and electric currents are directed in the same direction and an electron conductor ($\alpha < 0$, n -type), where the thermal and electric currents are directed in the opposite directions.³ The material legs assembled in electric series are commonly connected using metallic (e.g. copper) connectors. If the device is placed in a drop of thermal potential ΔT , a difference in the electric potential $\Delta\varphi = U$ builds up, and, according to Eq. 1, coupled currents I_S and I_{el} are generated. The direct conversion of thermal energy to electric energy is unique for thermoelectric systems. Hence, a TEG is a device that transfers energy from an entropy current directly to an electric current.¹⁻³ These properties make a thermoelectric generator useful for recovering waste heat in different processes.

At the power-maximum of the characteristic parabolic power-plots, the internal resistance of the generator $R_{el,TEG}$ is equal to the external load-resistance R_{load} . The entire resistance $R_{el,TEG}$ results in the addition of the resistances of each integrated thermoelectric leg (neglecting the electric resistances of the metallic connectors). The maximum electric power output is then received by Eq. 3.

$$P_{el,max} = \frac{U_{OC}^2}{4 \cdot R_{el,TEG}} = \frac{(\sum \alpha_{p-leg} - \sum \alpha_{n-leg})^2}{4 \cdot (\sum R_{p-leg} + \sum R_{n-leg})} \Delta T^2 \quad (3)$$

Hence, a maximization of the material specific electric conductivity σ leads to a minimization of the entire electric resistance of the regarded generator $R_{el,TEG}$. The flexible stripe-TEGs were fabricated as already reported by us.⁷

The figure of merit ZT_{TE} for thermoelectric materials gives a relationship with the conversion efficiency and can be expressed by the parameters thermovoltage (electric open-circuit) U_{OC} , the short-circuit electric current $I_{el,SC}$ and the entire electric resistivity R_{el} that is related to the geometry of the regarded sample, according to the following descriptions.⁸

$$ZT = \frac{U_{OC}}{I_{el,SC} \cdot R_{el}} - 1 = \frac{\sigma \cdot \alpha^2}{\lambda} \cdot T = \frac{\sigma \cdot \alpha^2}{\Lambda} \quad (4)$$

The first term can directly be used to estimate the figure-of-merit for an entire generator ZT_{TEG} . The figure-of-merit is related to the conversion efficiency η_{el} which increases with the increasing power factor $\sigma\alpha^2$ and decreases with increasing heat conductivity

λ . The conversion efficiency η is an important parameter if the thermoelectric generator is applied in a thermal potential gradient exhibiting a finite heat-source working at low thermal currents.

In order to maximize the electric output power P_{el} of a certain TEG, it is disadvantageous to decrease the thermal conductivity of the integrated thermoelectric materials. Narducci published a remarkable work that gives an insight into thermoelectric power generation using infinite heat-sources with high thermal energy input. He postulates that the materials then need to reach a threshold value for the thermal conductivity (not a minimized value for the thermal conductivity) to receive the maximum electric power output.⁹

$$P_{el} = -\eta_{el} \cdot P_{th} = -\eta_{el} \cdot \frac{A_{leg}}{L_{leg}} \cdot \lambda \cdot \Delta T \quad (5)$$

Hence, for infinite heat-sources, the thermal conductivity λ must not have to exhibit too low values to harvest the maximum electric power output. The amount of generated electric power is limited by the thermal power P_{th} fed into the TEG at the hot side. Regarding lower thermal resistances of the thermoelectric materials in the generator leads to an increase of the electric power output at suboptimal conversion efficiency. The efficiency at electric maximum power ($R_{el,TEG} = R_{load}$) η_{el} is obtained as shown in Eq. 6.

$$\eta_{el} = \frac{1}{2} \cdot \frac{T_h - T_c}{T_h} \cdot \left(1 + \frac{2}{Z \cdot T_h} - \frac{\Delta T}{4 \cdot T_h} \right)^{-1} \quad (6)$$

The term in front of the bracket is the Carnot efficiency $\eta_c = \frac{T_h - T_c}{T_h}$.

Due to explained relationship, the ceramic $\text{Ca}_3\text{Co}_4\text{O}_9$ (CCO) phase was modified in order to increase the power factor of the obtained composite materials and include metallic Ag aggregations to provide the possibility to generate a larger amount of thermal current density inside the composite materials compared to the single $\text{Ca}_3\text{Co}_4\text{O}_9$ phase. Since Ca-Co-O cobaltite ceramic systems aroused interest because of their good termoelectric performance, there have been many studies on modifying the layered oxide materials. Single crystals of $\text{Ca}_3\text{Co}_4\text{O}_9$ exhibit a figure-of-merit $ZT = 0.83$ at 973 K.¹⁰ Polycrystalline ceramic samples show significantly lower values. Compared to other thermoelectric oxide materials, the CCO-based materials exhibit high charge carrier concentrations in the temperature range close to room temperature, which make these materials applicable not only at high temperatures. Measured thermoelectric parameters for polycrystalline $\text{Ca}_3\text{Co}_4\text{O}_9$ ceramics from various laboratories have been assembled.¹¹ The $\text{Ca}_3\text{Co}_4\text{O}_9$ -based ceramics belong to the family of misfit cobalt oxides consisting of stacked CdI_2 -type CoO_2 layers and NaCl-type Ca_2CoO_3 units

Table I. Physical manufacturers' data of applied commercial materials with thermoelectric parameters for 293 K

Material	$\sigma/S\text{cm}^{-1}$	$\lambda/W\text{m}^{-1}\text{K}^{-1}$	$\Lambda/W\text{m}^{-1}\text{K}^{-2}$	$\alpha/\mu\text{VK}^{-1}$	$T_{\text{degradation}}/\text{K}$
Mineral fiber	$10^{-14} \dots 10^{-15}$	1.0	3.4×10^{-3}	n.a	890 (T_{strain})
Cu tape	5.88×10^5	394	1.3	n.a	1356 (T_{melt})
Cu-Ni alloy	2.04×10^4	23	7.8×10^{-2}	-40	1553 (T_{melt})
Ag-epoxy resin	1.11×10^3	1.0	3.4×10^{-3}	n.a	623 (T_{strain})

n.a. Not available.

along the c -axis. A detailed structure refinement of the $\text{Ca}_3\text{Co}_4\text{O}_9$ phase was performed.¹² The incommensurate structure can be written as $[\text{Ca}_2\text{CoO}_3]_{(b_1, b_2)}\text{CoO}_{2-\delta}$ concerning different b -values for each subsystem. The addition of Ag and Cu has been reported to increase the isothermal specific electronic conductivity σ . Those studies were mainly performed using the solid-state synthesis route. Ag-modified $\text{Ca}_3\text{Co}_4\text{O}_9$ -based materials have already been applied in a rigid high-temperature TEG.¹³ In the present work, the ceramic materials were synthesised by the sol–gel method which is described in the “Experimental” section. The prepared samples showed a clear trend related to the presence of Ag- and Cu-distribution in the samples. Using the sol–gel route, the batched Ag^+ -ions get reduced in the aqueous sol. Hence, in the presented samples, the Ag is present in the form of large metallic agglomerates that are inhomogenously scattered in the oxide matrix. Such metallic Ag inclusions have also been investigated in order to dope CCO.¹⁴ While the added Ag makes the ceramic materials ceramic–metallic CCO–Ag composite phases, the added Cu forms Cu-oxide phases that are present in the CCO-matrix as homogenously distributed microscale inclusions. Hence, the addition of Ag and Cu in the sol–gel route makes the samples oxide–metal, namely $\text{Ca}_3\text{Co}_4\text{O}_9/\text{CuO}/\text{Ag}$, composite phases.

EXPERIMENTAL

Material Synthesis and Preparation of Generators

The p -type thermoelectric oxide $\text{Ca}_3\text{Co}_4\text{O}_9$ was synthesized using the sol–gel method.⁶ Nitrates of calcium, cobalt, silver and copper cations were stoichiometrically added to an aqueous ammonia solution of pH = 9 containing citric acid and EDTA for complexing the solvated metal ions. The amounts $x_{\text{Ag}} = x_{\text{Cu}} = x$ were 0, 0.02, 0.05, 0.1 and 0.2 (0 mol.%, 2 mol.%, 5 mol.%, 10 mol.%, and 20 mol.%). The obtained precipitates were calcined at 1173 K for 5 h with a heating and cooling rate of 3K min^{-1} . The calcined powder product was cold-pressed and sintered at 1173 K for 20 h at a heating and cooling rate of 2K min^{-1} . Bar-shaped legs with

length, width and thickness of 8 mm, 1.5 mm, and 1 mm, respectively, were cut from the obtained $\text{Ca}_3\text{Co}_4\text{O}_9$ -based ceramic discs.

The Cu-Ni alloy was in the form of a commercially available wire with a diameter of 1 mm. To connect the thermoelectric materials, adhesive Cu-tape was attached on a mineral-fiber band. The used pieces of copper tape have a width of 6.3 mm and a thickness of 50 μm . The mineral-fiber band is 14.5 mm wide and 150 μm thick. Silver paste was used to preconnect the thermoelectric materials with the Cu connectors. To receive a mechanically stable connection, the legs were fixed to the Cu connectors using Ag-epoxy resin. The Ag-resin was cured at 400 K for 1 h. Using the silver paste without fixing afterwards leads to the delamination of the silver layer from the Cu surface during heating due to the thermomechanical stresses inside the assembled layer structure. In the final devices, the thermoelectric legs have a median distance of 2.5 mm. The manufacturer's physical data for applied commercial materials are listed in Table I. The parameters for the Cu tape were taken from the data sheet prepared by Deutsches Kupfer-Institut e.V. (DKI).¹⁵

Microstructure Analysis

The materials were analyzed using field-emission scanning electron microscopy (FE-SEM) using a JEOL JSM-6700F, equipped with an Oxford Instruments INCA 300 energy-dispersive x-ray spectrometer (EDXS) for elemental analysis. Furthermore, transmission electron microscopy (TEM) was used to investigate the microstructure of composite materials on the micro- to nano-scale. The phase compositions of the sintered ceramic materials were analyzed by x-ray diffraction (XRD) using a Bruker D8 Advance with Cu-K_α radiation. The obtained diffraction data were analysed by the Rietveld method using the TOPAS 4.1 software. The reference data for the crystal structure analysis were taken from the Powder Diffraction File (PDF2) database.

Thermoelectric Measurements of Single Materials

To characterize the thermoelectric properties of the materials, the temperature-dependent

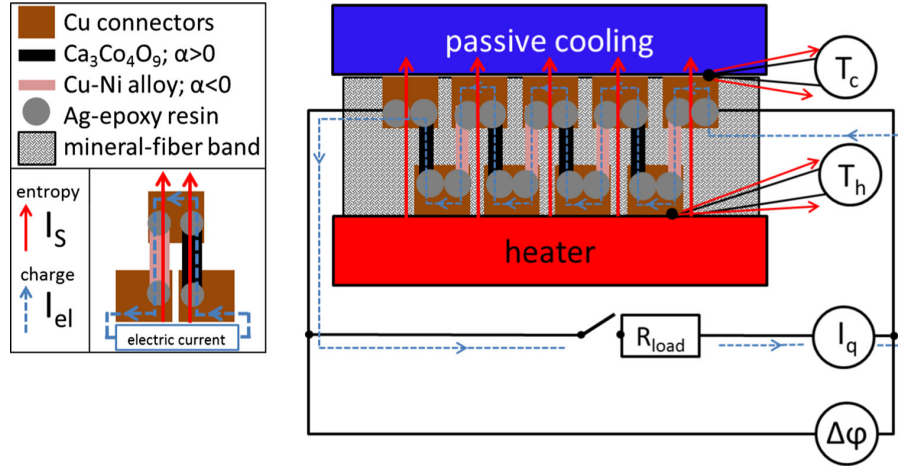


Fig. 1. The measurement setup showing the assembled materials in the stripe-TEG.

isothermal specific electric conductivity and the Seebeck coefficient, as estimated from the thermovoltage, were measured. Using these data, the power factor $\sigma\alpha^2$ and the coupling factor $\sigma\alpha$, which are a part of the thermoelectric material tensor in Eq. 1, were estimated for each compound. A precision vertical diamond wire-saw model 3242 from O'WELL was used for sample preparation. The isothermal specific electric conductivities were measured using a measurement cell constructed in-house which is a modified version of the arrangement described by Indris.¹⁶ The sample is clamped between two platinum electrodes to close the electric circuit in a pseudo-four-point measurement. The Seebeck coefficient was measured using a NORECS probostat measurement system. The applied furnace was an ELITE thermal system. The electronic parameters were measured with KEITHLEY 2100 6 $\frac{1}{2}$ Digit Multimeters. The measured data were acquired and converted using LAB VIEW software.

Thermoelectric Measurements of Flexible Stripe-TEGs

The fabricated stripe-TEGs were placed on a heater to estimate their thermoelectric characteristics. The heat sink was established naturally, using the temperature drop, which was generated by contacting a passive cooling system to the cold sides of the devices. The passive-cooler was exchanged at each temperature step and the temperature profile was equilibrated. Hence, the temperature of the cold junction of the device increased with increasing temperature of the hot side (heater side). The used heat-source was a STUART CB160 hot-plate. The

flexible stripe-TEGs were placed on the heater in a bent (coiled) form. The thermovoltage $U = \Delta\phi$ and the electric current I_{el} were measured for different values of the external load. A sketch of the measurement setup including a legend of applied materials is presented in Fig. 1.

RESULTS AND DISCUSSION

The thermoelectric measurement data for the Seebeck coefficient α , the electric isothermal specific conductivity σ and the combined parameters $\sigma\alpha$ and $\sigma\alpha^2$ are presented in Fig. 2.

In Fig. 2a, the thermoelectric properties are assembled in a way of a Jonker analysis.^{17,18} From the theoretical point of view, the correlation of the Seebeck coefficient α and the logarithmic isothermal specific electric conductivity $\ln(\sigma)$ show a linear dependence. Non-degenerated *p*-type material systems, which belong to the same basic phase, are positioned on a line exhibiting the slope of $-\frac{k_B}{e} = -86.15\mu\text{V K}^{-1}$. Degenerated systems deviate from this line showing higher values for the specific electric conductivity σ . For larger amounts of Ag in the composite materials, such a degenerated behavior is expected. But the ceramic sample with $x = 0.05$ showed the highest Seebeck coefficient which makes the material with 5 mol.% Ag and Cu the one providing a local maximum value for the power factor $\sigma\alpha^2$ in the range of 0–10 mol.% (Fig. 2-c). In Fig. 2b, the dependence of the Ag and Cu amount and $\ln(\sigma)$ is presented. The data show a linear dependence. In Fig. 2d, the coupling factor $\alpha\sigma$, which is part of the thermoelectric material tensor in Eq. 1, is plotted versus the Ag and Cu amount. The thermoelectric parameters of

Enhanced Flexible Thermoelectric Generators Based on Oxide–Metal Composite Materials

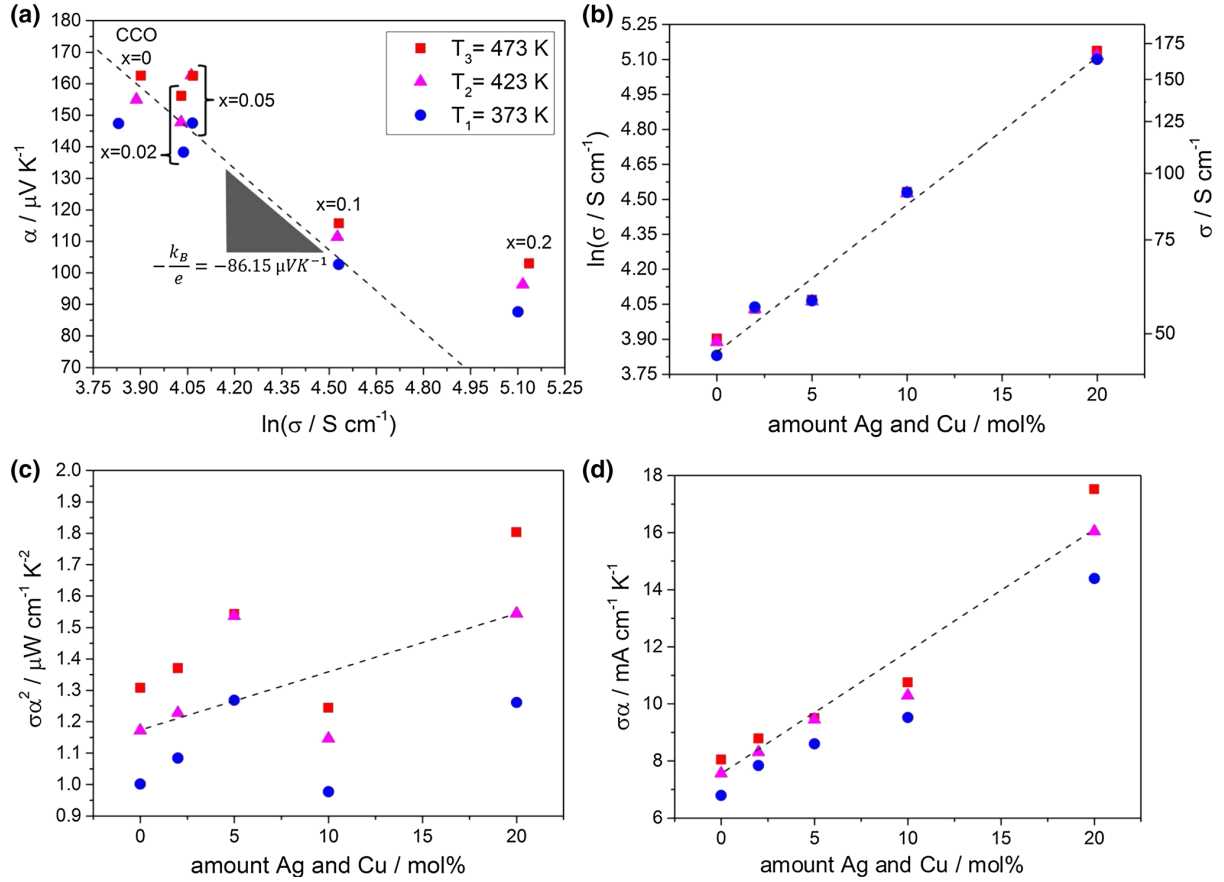


Fig. 2. Thermoelectric properties of synthesized $\text{Ca}_3\text{Co}_4\text{O}_9$ -based materials with plotted linear guidelines (dashed lines); (a) Jonker plot ($\ln(\sigma)$ versus Seebeck coefficient α) with line of slope $-\frac{k_B}{e} = -86.15 \mu\text{V K}^{-1}$ as guide to the eye, (b) isothermal specific electronic conductivity σ (logarithmic scale) and $\ln(\sigma)$ versus amount of Ag and Cu, (c) power factor $\sigma\alpha^2$ versus amount of Ag and Cu, (d) coupling factor $\sigma\alpha$ versus amount of Ag and Cu.

synthesised materials generally show expected behavior in terms of the Jonker analysis. For Fig. 2a, the relationship of the Seebeck coefficient α and the specific electric conductivity σ is:

$$\alpha = -\frac{k_B}{e} (\ln \sigma - \ln \sigma_0) \quad (7)$$

For the coupling factor $\sigma\alpha$ (Fig. 2d), the theoretical assumption gives:

$$\sigma\alpha = -\frac{k_{rmB}}{e} (\ln \sigma - \ln \sigma_0) \sigma \quad (8)$$

And for the power factor $\sigma\alpha^2$ (Fig. 2c) it is:

$$\sigma\alpha^2 = \left(\frac{k_B}{e}\right)^2 (\ln \sigma - \ln \sigma_0)^2 \sigma \quad (9)$$

σ_0 is the intercept of the line.

To clarify the structure–property relationships, the synthesised composite materials were analysed

by electron microscopy methods. Furthermore, the phases of the $\text{Ca}_3\text{Co}_4\text{O}_9$ -matrix and the oxidic CuO and the metallic Ag inclusions were confirmed by XRD diffraction measurements and by electron diffraction in the framework of the TEM analysis. The Ag crystallizes in the cubic crystal system.

The stoichiometry of the $\text{Ca}_3\text{Co}_4\text{O}_9$ phase is only thermodynamically stable in a small window of Co content in the oxide structure. There have been studies on the phase composition in dependence of the Co content, resulting in a phase diagram for the Ca–Co–O systems.¹⁹ To get a closer view into the synthesized CCO-based phases, electron microscopic studies were carried out using cross-section polished samples from the ceramic-based composite materials. In Fig. 3, the distributions of samples containing elements are presented in the form of pseudo-color energy-dispersive elemental mapping. Figure 3f shows the EDX spectrum related to the

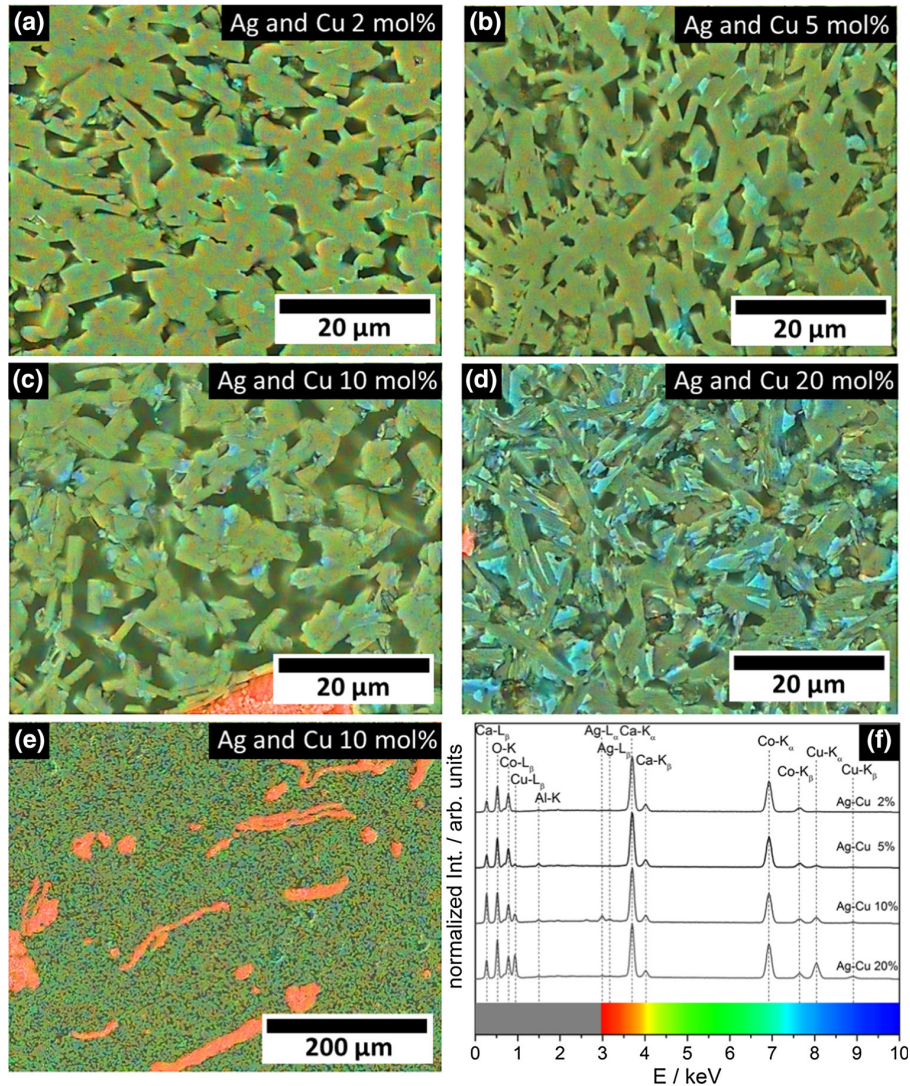


Fig. 3. EDXS-based pseudocolor mapping of vibration-polished cross-section of prepared $\text{Ca}_3\text{Co}_4\text{O}_9$ -based ceramic materials. (a) Homogeneous region of the sample with $x = 0.02$, (b) homogeneous region of the sample with $x = 0.05$, (c) homogeneous region of the sample with $x = 0.1$, (d) homogeneous region of the sample with $x = 0.2$, (e) inhomogeneously distributed metallic Ag-agglomerates in the material with $x = 0.1$, (f) EDX spectra of homogeneous regions related to the areas shown in (a–d) with integrated energy-pseudocolor scale.

homogeneous areas shown in Fig. 3a–d. To show the metallic Ag agglomerates, a lower magnification of the sample with 10 mol.% of Ag and Cu is presented in Fig. 3e. While the Cu-rich oxide inclusions exhibit grain sizes in the range of 1–10 μm , the metallic Ag regions are approximately 10–20 times larger.

The composite samples with 5 mol.% and 20 mol.% Ag and Cu content were analyzed by TEM. The CuO phase was found as sub-micrometer inclusions. Ag was not found on the sub-micrometer

scale. The silver agglomerates exhibited formations in the micrometer range (see Fig. 3e). Figure 4 shows sub-micrometer CuO inclusions embedded in the CCO-matrix.

Figure 4e presents the EEL spectra processed for the $\text{Ca}_3\text{Co}_4\text{O}_9$ phase (green-colored) and the CuO inclusions (blue-colored). The phases were found as separated systems with less interpenetrated cation exchange. The EEL spectra show a small content of Co inside the CuO phase. Hence, the phases forming the composite material are $\text{Ca}_3\text{Co}_4\text{O}_9$ as matrix

Enhanced Flexible Thermoelectric Generators Based on Oxide–Metal Composite Materials

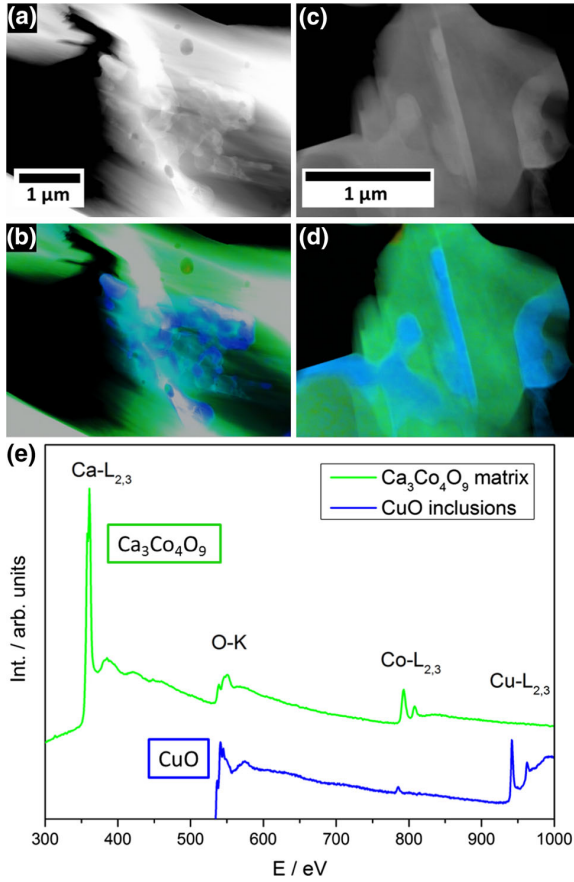


Fig. 4. Results of TEM investigations. (a, b) 5 mol.% Ag and Cu, (c, d) 20 mol.% Ag and Cu, (a, c) dark-field micrographs with bright CuO inclusions in the darker $\text{Ca}_3\text{Co}_4\text{O}_9$ matrix, (b, d) pseudocolor mapping related to the energy-pseudocolor scale presented in Fig. 3f. (e) EEL spectrum of $\text{Ca}_3\text{Co}_4\text{O}_9$ matrix (upper green curve) and CuO inclusions (bottom blue curve). Scale bars of (a and c) also apply to (b and d), respectively (Color figure online).

material with micrometer Ag agglomerates and CuO as inclusions on the submicrometer to the micrometer scale. No other phases were formed in the synthesis of the composite materials. The smaller CuO formations are supposed to conserve the Seebeck coefficient α of the composite materials by influencing the electron-scattering in the entire phase. Therefore, the sample with 20 mol.% Ag and Cu exhibits a conserved value of the Seebeck coefficient α compared to the high electrical conductivity. The values of the 20 mol.% deviate from the Jonker-line to higher values of the electrical conductivity. Such an arrangement of phases in the

composite material leads to an increased value of the power factor. The Ag phase is present in larger metallic agglomerates which provide pathways in the composite bulk material which decrease the resistances for charge and entropy. The Ag formations are not percolated. For an entire Ag percolation in the $\text{Ca}_3\text{Co}_4\text{O}_9$ matrix, the composite materials are supposed to exhibit a low metal-like value for the Seebeck coefficient α .

The $\text{Ca}_3\text{Co}_4\text{O}_9$ -based materials were prepared and integrated in flexible TEGs. As described in the “Experimental” section, each TEG was constructed in the same way but the p -type CCO-based material was varied. Figure 5a and b show photomicrographs of constructed TEGs displaying the used materials. In Fig. 5c, photomicrographs of cut composite materials are presented. In Fig. 5d, a top view of the bent device is shown and the curvature was graphically estimated. Figure 5e shows the measurement setup for determining the TEG’s electric power output characteristics. The measurements were performed applying a passive cooling system. The devices were measured in a bent (coiled) form. The physical parameters of the materials used are listed in Table I.

The thermoelectric power-characteristics for each TEG related to the hot-side temperature are presented in Fig. 6. The performance-determining parameters are open-circuit voltage U_{OC} , the short-circuit electric current I_{SC} and the entire resistivity $R_{el,TEG}$ which were determined by applying Ohm’s law. The parameters are assembled in Table II.

The measurement data referring to the TEG’s parameters reflect the data that were received for the CCO-based p -type materials. The maximum electric power output was obtained for the TEG constructed using the material with $x = 0.05$, reaching a slight maximum compared to the other TEGs. With increasing Ag amount of the p -type material, the generator’s short-circuit electric current increases due to the decreasing electric resistivity; therefore, the thermal conductivity is expected to increase. The open-circuit voltage decreases with increasing amounts of Ag and Cu as expected from the measurements of the Seebeck coefficient. But the TEG, containing the material with $x = 0.05$, also exhibits the highest open-circuit voltage, which is expected due to the measured values of the Seebeck coefficient. To calculate the figure-of-merit ZT_{TEG} for the investigated stripe-TEGs, the characteristic parameters, which are presented in Table II, were used. The relationship for these data, expressing ZT , is displayed in Eq. 4. From the calculated values for the figure-of-merit, the conversion efficiency was estimated using Eq. 6. The efficiency

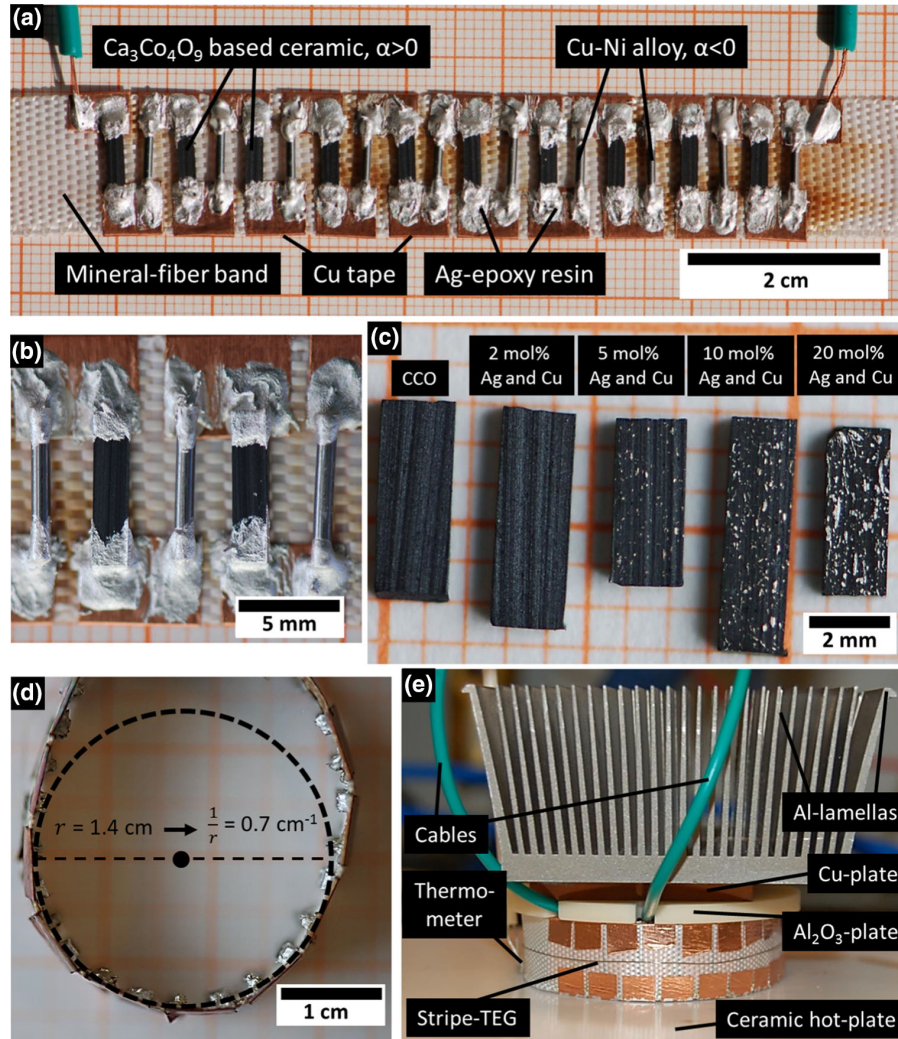


Fig. 5. Photomicrographs of constructed TEGs: (a) stripe TEG showing used materials, (b) magnified photograph of TEG showing detailed impression of integrated legs, (c) photograph of cross-sections of the synthesised CCO-based materials showing the macroscopic metallic Ag inclusions, (d) top view on bent stripe-TEG showing the maximum curvature of the devices, (e) measurement setup for determination of TEG's power-characteristics related to Fig. 1.

varies anti-proportionally to the maximum electric power output of the characterised TEGs with respect to the Ag content of the materials. The relationships of ZT_{TEG} , η_{el} and P_{el} are illustrated in Eqs. 4, 5, and 6. The efficiency η_{el} and ZT are counter-related in the framework of the thermal conductivity λ of the system. In Fig. 6a, the

predicted shape of the decay-fit is shown which illustrates the decrease of the conversion efficiency η_{el} (dashed curves) while the maximum electric power output increases, as is illustrated by the asymptotic fits (dashed curves).⁹ The generator containing the pure CCO material exhibits the best efficiency but is limited in terms of electric output-

Enhanced Flexible Thermoelectric Generators Based on Oxide–Metal Composite Materials

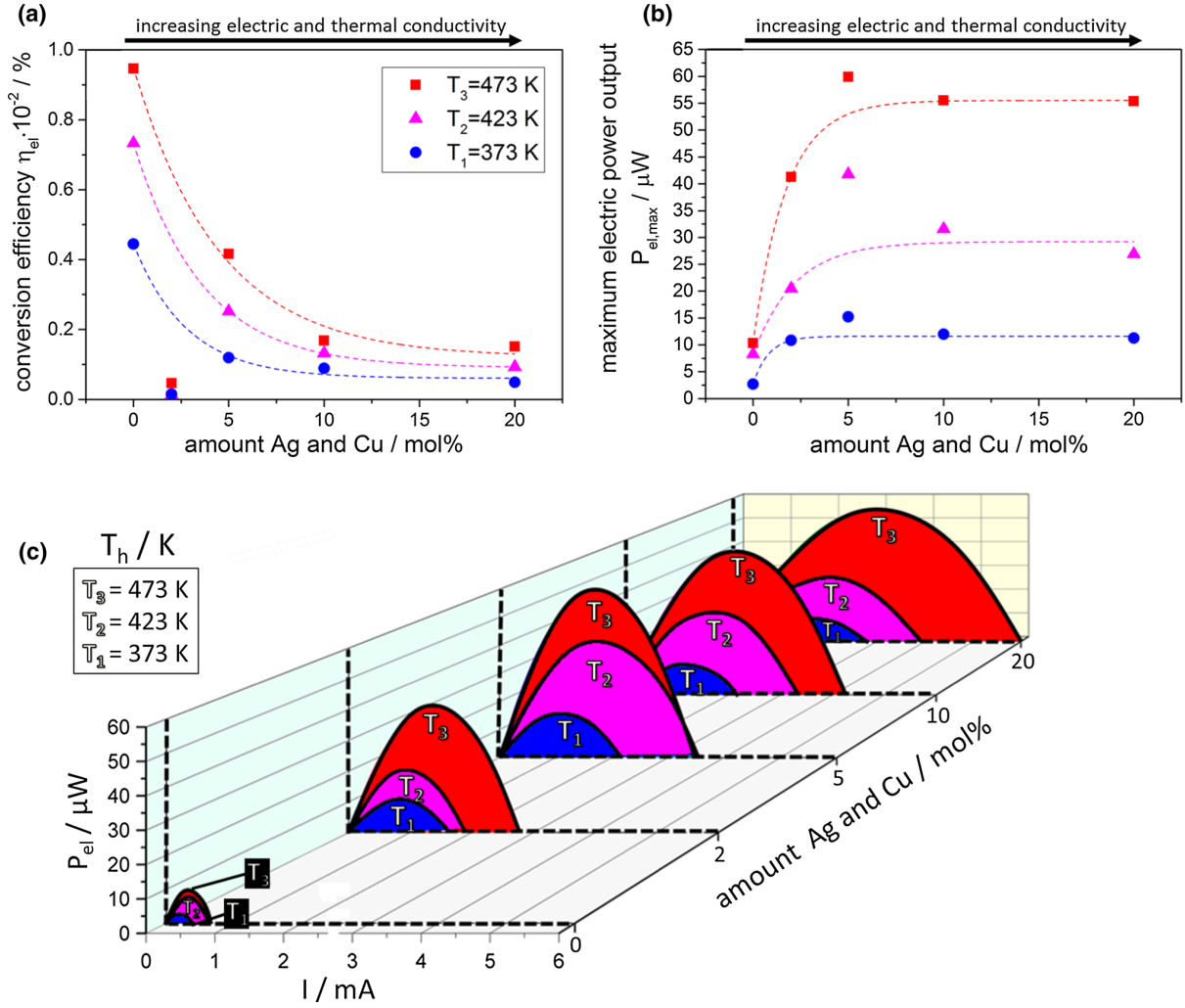


Fig. 6. Power characteristics of constructed TEGs. (a) Conversion efficiency η for the constructed TEGs calculated from electric parameters using Eq. 6, (b) maximum electric output-power of stripe-TEGs related to different amounts of Ag and Cu in the $\text{Ca}_3\text{Co}_4\text{O}_9$ -based p -type legs, (c) parabolic power-characteristics for each constructed stripe-TEG for the three applied hot-plate temperatures.

Table II. Determined thermoelectric parameters of the flexible TEGs for different temperature conditions

composition	T_{hot}/K	$\Delta T/K$	$R_{el,TEG}/\Omega$	$P_{el,max}/\mu W$	U_{OC}/mV	$I_{el,SC}/mA$	$ZT_{TEG} \times 10^{-3}$
CCO $x = 0$	473	30.3	110.35	10.33	67.7	0.61	5.74
	423	22.4	77.58	8.28	50.7	0.65	5.41
	373	13.2	82.37	2.70	29.8	0.36	4.95
$x = 0.02$	473	27.6	21.66	41.27	59.8	2.76	0.31
	423	20.1	23.42	20.48	43.8	1.87	0.11
	373	12.2	15.72	10.83	26.1	1.66	0.18
$x = 0.05$	473	30.8	19.75	59.88	68.9	3.48	2.47
	423	20.1	13.40	41.79	47.4	3.58	2.07
	373	12.4	12.78	15.23	27.9	2.18	1.42
$x = 0.1$	473	30.6	12.27	55.52	52.2	4.25	1.01
	423	21.8	11.37	31.56	37.9	3.33	1.00
	373	13.3	10.65	11.96	22.6	2.12	0.97
$x = 0.2$	473	23.7	6.18	55.38	37.0	5.98	1.18
	423	17.4	6.88	26.88	27.2	3.95	0.88
	373	10.9	6.04	11.25	16.5	2.73	0.65

power due to its high internal electric and thermal resistivity.

CONCLUSIONS

In the presented study $\text{Ca}_3\text{Co}_4\text{O}_9$ -based composite materials were synthesized. In the batches of the sol-gel route, Ag and Cu were added to the synthesis solutions with amounts of 0 mol.%, 2 mol.%, 5 mol.%, 10 mol.%, and 20 mol.%. The sintered samples were obtained as composite materials containing the $\text{Ca}_3\text{Co}_4\text{O}_9$ phase, and with increasing amounts of silver the fraction of inhomogeneously distributed metallic Ag agglomerates also increases. With increasing the Cu content in the batches, an increasing amount of CuO phase was formed during the synthesis. The thermoelectric analysis results in a local maximum of the power factor σx^2 for the material with 5 mol.% Ag and Cu. In the Jonker analysis, the samples with 5 mol.% and 20 mol.% deviate from the Jonker-line. The material with $x = 0.05$ showed a higher value for the Seebeck coefficient α and the material with $x = 0.2$ exhibits a higher value for the electric conductivity σ as expected by the Jonker analysis.

The investigations of the constructed stripe-TEGs resulted in measurement data that can be understood in light of Narducci's approach.⁹ For the TEG containing the material with $x = 0.05$ Ag and Cu, a slight maximum for the electric output power for each hot-side temperature was obtained. The optimum parameter balance for the investigated system is reached in the range of $x = 0.05$. With increasing content of metallic Ag, the thermal resistivity drastically decreases. For amounts of Ag larger than $x = 0.05$, the electric power output reaches a plateau-region, which is predicted by Narducci for systems exhibiting power factors of the same order of magnitude. The conversion efficiency η_{el} decreases with increasing Ag content due to the increasing thermal conductivity. For the generator containing the pure $\text{Ca}_3\text{Co}_4\text{O}_9$ phase, the conversion efficiency

η_{el} starts with maximum values and decreases with increasing amounts of Ag in the samples. The summarized results confirm the results executed by Narducci that ZT is not the determining quantity for the maximization of electric output power of a certain TEG system. For $\text{Ca}_3\text{Co}_4\text{O}_9$ -based materials in TEGs, considering an infinite heat source, the limiting parameters are the power factor and the thermal conductivity of the material. Therefore, the TEG including the p -type material with $x = 0.05$ showed the largest electric power output which was more than 5 times larger than that of the TEG including the pure $\text{Ca}_3\text{Co}_4\text{O}_9$ p -type material.

REFERENCES

1. H. Fuchs, *Graduate Texts in Physics*, 2nd edn. Springer, Berlin (2010).
2. H. Fuchs, *EHS*, 1(3–4), 253 (2014).
3. A. Feldhoff *EHS*, 2(1), 5 (2015).
4. A. Feldhoff and B. Geppert, *EHS*, 2(1–2), 69 (2014).
5. B. Geppert, D. Groeneveld, V. Loboda, A. Korotkov, and A. Feldhoff, *EHS*, 10, 689 (2008).
6. A. Feldhoff, M. Arnold, J. Martynczuk, T. Gesing, and H. Wang, *Solid State Sci.*, 10, 689 (2008).
7. B. Geppert and A. Feldhoff, *EHS*, 2, 1 (2015).
8. G. Min and D. Rowe, *Meas. Sci. Technol.*, 12, 1261 (2001).
9. D. Narducci, *Appl. Phys. Lett.*, 99, 102104–1 (2011).
10. M. Shikano and R. Funahashi, *Appl. Phys. Lett.*, 82(12), 1851 (2003).
11. J. Fergus, *J. Eur. Ceram. Soc.*, 32, 525 (2011).
12. S. Lambert, H. Leligny, and D. Gebrille, *J. Solid State Chem.*, 160, 322 (2001).
13. L. Han, Y. Jiang, S. Li, H. Su, X. Qin, T. Han, H. Zhong, L. Chen, and D. Yu, *J. Alloys Compd.*, 509, 8970 (2011).
14. Y. Wang, Y. Sui, J. Cheng, X. Wang, and W. Su, *J. Phys. D: Appl. Phys.*, 41, 1 (2008).
15. H. Franke and K. Juhl, *Kupfer in der Elektrotechnik-Kabel und Leitungen*, 1st edn. Breuerdruck, Korschbroich (2010).
16. S. Indris, Perkolaton von Grenzflächen in nanokristallinen kera-mi-schen Kompositen - Li-Ionenleitfähigkeit und ⁷Li-NMR-Relaxation, Dissertation (Cuvillier Verlag) (2001).
17. G. Jonker, *Philips Res. Rep.*, 23(2), 8 (1968).
18. Q. Zhu, E. Hopper, B. Ingram, and T. Mason, *J. Am. Ceram. Soc.*, 94(1), 187 (2011).
19. O. Jankovsky, D. Sedmidubsky, Z. Sofer, P. Simek, and J. Hejtmanek, *Ceram. Silik.*, 56(2), 139 (2012).

3 Thermoelectric generators research

3.1 Summary

The construction of thermoelectric generators requires the electrical series connection of materials with n-type and p-type conduction mechanism. This essential assembly was realized by the commonly used rigid chess-board geometry and by flexible (i.e. coilable) stripe thermoelectric generators.

In section 3.2 an oxide-based thermoelectric generator with $\text{In}_{1.95}\text{Sn}_{0.05}\text{O}_3$ as n-type material is presented. The rigid design, constructed with $\text{Zn}_{0.98}\text{Al}_{0.02}\text{O}$ as n-type legs and $\text{Ca}_3\text{Co}_4\text{O}_9$ (CCO) as p-type legs, is applicable in the high-temperature range only ($T > 1000$ K). The isolating character of the ZnO-phase at lower temperatures averts the application in the intermediate-temperature range, in the way, that an increased electrical conductivity of the n-type material is needed.

In section 3.3 a prototype system of a flexible device is presented. For usage at lower temperatures, Cu-Ni-Mn alloy was integrated as n-type material. The $\text{Ca}_3\text{Co}_4\text{O}_9$ phase exhibits a high charge carrier concentration compared to other oxides, and therefore, this material is applicable in the low- and intermediate-temperature range. Such a material combination was used to fabricate the flexible stripe-TEGs. These stripe-TEGs can be fabricated as open system. The thermoelectric bulk material legs can be assembled easily.

A finite-element simulation tool was used to model thermoelectric devices with all assembled materials of the entire system. In section 3.4 a script-based tool was developed and validated using a commercial device. Deep insights into the local variations of the relevant thermoelectric parameters were obtained from this type of modeling. Overall, the developed model system can predict the thermoelectric properties of a certain TEG if the proper parameters for feeding the simulation tool are selected. Work on thermoelectric materials and systems benefits from the use of finite-element simulations to check the properties before constructing a device.

In section 3.5 the finite-element simulation tool was modified and applied to a home-made generator. The properties of the regarded systems can be varied easily, thus making finite-element simulation tools a very flexible possibility for predicting the power characteristics of a thermoelectric device in terms of the requirements for its application. The contact resistances were determined and integrated into the simulation. This procedure made the simulation result in the accurate values of the electric current density inside each material of the prototype generator.

3.2 Oxide-Based Thermoelectric Generator for High-Temperature Application Using p-Type $\text{Ca}_3\text{Co}_4\text{O}_9$ and n-Type $\text{In}_{1.95}\text{Sn}_{0.05}\text{O}_3$ Legs

Michael Bittner, Benjamin Geppert, Nikola Kanas,

Sathya Prakash Singh, Kjell Wiik and Armin Feldhoff

Energy Harvesting and Systems, 3(3), 213-222, (2016)

Michael Bittner*, Benjamin Geppert, Nikola Kanas, Sathya Prakash Singh, Kjell Wiik and Armin Feldhoff

Oxide-Based Thermoelectric Generator for High-Temperature Application Using p-Type $\text{Ca}_3\text{Co}_4\text{O}_9$ and n-Type $\text{In}_{1.95}\text{Sn}_{0.05}\text{O}_3$ Legs

DOI 10.1515/ehs-2016-0002

Abstract: A thermoelectric generator couples an entropy current with an electrical current in a way, that thermal energy is transformed to electrical energy. Hereby the thermoelectric energy conversion can be described in terms of fluxes of entropy and electric charge at locally different temperature and electric potential. Crucial for the function of a thermoelectric generator is the sign and strength of the coupling between the entropy current and the electrical current in the thermoelectric materials. For high-temperature application, tin-doped indium oxide ($\text{In}_{1.95}\text{Sn}_{0.05}\text{O}_3$) and misfit-layered calcium cobalt oxide ($\text{Ca}_3\text{Co}_4\text{O}_9$) ceramics were used as n- and p-type legs. The n-type material reaches a power factor of $6.8 \mu\text{W} \cdot \text{cm}^{-1} \cdot \text{K}^{-2}$ at 1,073 K and a figure of merit ZT of 0.07. The p-type material reaches $1.23 \mu\text{W} \cdot \text{cm}^{-1} \cdot \text{K}^{-2}$ and a figure of merit ZT of 0.21 at 1,073 K. A thermoelectric generator consisting of ten legs was characterized for different invested temperatures. It delivers 4.8 mW maximum power output and a electrical power density of $2.13 \text{mW} \times \text{cm}^{-2}$ when the hot side is at 1,073 K and a temperature difference of 113 K is applied.

Keywords: Thermoelectric power generation, Module, Oxide materials, $\text{Ca}_3\text{Co}_4\text{O}_9$, $\text{In}_{2-x}\text{Sn}_x\text{O}_3$

Introduction

Thermoelectric (TE) materials got lately more and more attention due to climate change and thereby their ability to utilize waste heat from power plants and combustion

*Corresponding author: Michael Bittner, Institute of Physical Chemistry and Electrochemistry, Leibniz Universität Hannover, Germany; Department of Materials Science and Engineering, NTNU Trondheim, Norway, E-mail: michael.bittner@pci.uni-hannover.de
Benjamin Geppert, Institute of Physical Chemistry and Electrochemistry, Leibniz Universität Hannover, Germany
Nikola Kanas, Sathya Prakash Singh, Kjell Wiik, Department of Materials Science and Engineering, NTNU Trondheim, Norway
Armin Feldhoff, Institute of Physical Chemistry and Electrochemistry, Leibniz Universität Hannover, Germany

engines. A thermoelectric generator, which is made of those materials can convert thermal energy into electrical energy. Research in the field of thermoelectric materials focuses on improving the figure of merit ZT, which was originally derived by Ioffe (1957) and is shown in eq. [1]. Improving the figure of merit ZT is one approach to enhance the efficiency of the energy conversion system.

$$ZT := \frac{\sigma \cdot \alpha^2}{\Lambda} \quad [1]$$

The involved material parameters are the isothermal electrical conductivity σ , the Seebeck coefficient α and the electric open-circuit entropy conductivity Λ . For clarity the latter is preferred over the thermal energy (“heat”) conductivity λ , which is related to it by eq. [2]; see Fuchs (2010) and Feldhoff (2015):

$$\lambda = \Lambda \cdot T \quad [2]$$

For high-temperature electric power generation in air, n- and p-type semi-conducting thermoelectric oxides are supposed to be promising materials, due to their advantages, such as non-toxicity, thermal and mechanical stability at high temperatures and moreover high chemical stability under oxidizing conditions; see Rowe (1995). Several publications focus on the layer-structured cobalt oxide $\text{Ca}_3\text{Co}_4\text{O}_9$, based on CaO, and Sn-doped indium oxide ($\text{In}_{2-x}\text{Sn}_x\text{O}_3$) due to their high power factor $\sigma \cdot \alpha^2$ and thus the efficiency of TEGs made of it, see Xu et al. (2002), Miyazaki (2004), Bérardan et al. (2008) and Guilmeau et al. (2009).

$\text{Ca}_3\text{Co}_4\text{O}_9$ exhibits a misfit-layered structure, which consists of CdI₂-type CoO₂ triangular lattice and a layered rock-salt part of three Ca₂CoO₃ units which are stacked alternately along the c-axis. The electronic structure of $\text{Ca}_3\text{Co}_4\text{O}_9$ is beneficial for thermoelectric applications due to its density of states (DOS), which consists of two non-bonding, degenerated e'_g levels and thus a broad delocalized e'_g band and a bonding, non-degenerated a_{1g} level and thereby a localized a_{1g} band. The density of states near the Fermi energy E_F is schematically shown in Figure 1(a). The height of the Fermi energy E_F can be

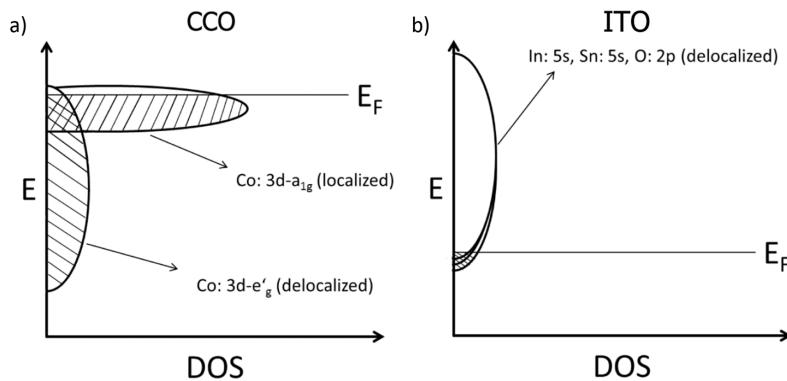


Figure 1: Schematic representation of the density of states (DOS) near the Fermi level E_F , occupied states (hatched) below E_F in: a) Co:3d energy levels of the rhombohedrally distorted CoO_6 octahedron (a_{1g} and e'_g) of $\text{Ca}_3\text{Co}_4\text{O}_9$ after Miyazaki (2004) and b) In:5s, Sn:5s and O:2p energy levels of $\text{In}_{1.95}\text{Sn}_{0.05}\text{O}_3$ after Yan and Wang (2012).

controlled by the valence state of cobalt cations. It can be adjusted with the aid of hole-doping, or with implementing dopants into the structure. When E_F crosses the border where the a_{1g} and e'_g orbitals are hybridized, according to Miyazaki (2004), a high electrical conductivity is expected due to a high density of unoccupied states in the electronic bands above the highest occupied state. The thermoelectric properties like electrical conductivity σ , Seebeck coefficient α and entropy conductivity Λ of $\text{Ca}_3\text{Co}_4\text{O}_9$ can be further enhanced by controlling the micro- and nano-structure. Liu et al. (2005) and Kenfaui et al. (2010) used spark plasma sintering (SPS) and Nagahama et al. (2002) a templated grain growth method to modify the structure of $\text{Ca}_3\text{Co}_4\text{O}_9$.

The Seebeck coefficient α can be expressed after eq. [3] for the degenerate case ($k_B T \ll E_F$) and depends on the ratio of the oxidation states of cobalt ($\text{Co}^{3+/4+}$); see Singh (2000) and Miyazaki (2004). Thereby $A(E)$ is proportional to the area of the DOS at the Fermi level E_F .

$$\alpha \sim - (\delta \ln A(E) / \delta E)_{E=E_F} \quad [3]$$

A prospective n-type oxide is In_2O_3 , which is an indirect semiconductor with a band gap of 1.16 eV. The top of the valence band of In_2O_3 shows a small dispersion (localized states), made of hybridized O:2p and In:5d states. The bottom of the conduction band possesses a large dispersion (delocalized states; see Figure 1(b)), which mainly comes from the hybridized O:2p and In:5s orbitals. For heavily doped In_2O_3 or by use of Sn as dopant, the E_F is situated inside the conduction band; see Figure 1(b). The electrical conductivity is strongly affected by the electronic configuration near the Fermi level E_F . When Sn is used as a dopant for In_2O_3 , a strong hybridization of the

Sn:5s, In:5s and O:2p orbitals forms antibonding states and thereby affects the states near the bottom of the conduction band, shown in Figure 1(b), which leads to a small band gap after Yan and Wang (2012).

The properties of tin-doped In_2O_3 (ITO) depend on the amount of Sn within the structure; see Guilmeau et al. (2009). For a low Sn fraction, $\text{In}_{2-x}\text{Sn}_x\text{O}_3$ possesses a medium effective mass m^* and a low carrier concentration n , which are both beneficial to the Seebeck coefficient α . For a highly degenerated semiconductor, the Seebeck coefficient α is defined after eq. [4], γ depends on the dominating scattering process (-0.5 for acoustic phonons, 0 for neutral impurities and 1.5 for ionized impurities); see Seeger (1991) and Guilmeau et al. (2009):

$$\alpha = \frac{2}{3} \left(\frac{\pi}{3} \right)^{\frac{2}{3}} \left(\gamma + \frac{2}{3} \right) \frac{k_B^2 m^*}{e h^2 n^{\frac{2}{3}}} \quad [4]$$

Guilmeau et al. (2009) already carried out investigations about tin-doped In_2O_3 , and it is assumed to be a promising thermoelectric n-type material. To our knowledge, no thermoelectric generator (TEG) has been constructed and characterized made of $\text{Ca}_3\text{Co}_4\text{O}_9$ as p-type and $\text{In}_{1.95}\text{Sn}_{0.05}\text{O}_3$ as n-type semiconductor.

Experimental

The thermoelectric materials, n-type $\text{In}_{1.95}\text{Sn}_{0.05}\text{O}_3$ (ITO) and p-type $\text{Ca}_3\text{Co}_4\text{O}_9$ (CCO), were synthesized via a sol-gel route, which allows obtaining fine-grained powders of homogenous composition as described by Feldhoff et al. (2008). The nitrates of accordant metal cations were stoichiometrically solved and added to an aqueous ammonia

solution of pH=9 which also contained citric acid and ethylenediaminetetraacetic acid (EDTA) for complexing the soluted metal ions in the solution. Indium(III) nitrate hydrate from Alfa Aesar, 99.9% trace metal basis was used as indium source and tin(II) acetate 95.0% from Alfa Aesar as tin source. For $\text{Ca}_3\text{Co}_4\text{O}_9$, calcium(II) nitrate tetrahydrate $\geq 99.0\%$ from Sigma Aldrich and cobalt(II) nitrate hexahydrate ACS 98–102.00% from Alfa Aesar were used as sources. The obtained powders were calcined for 10 h at 973 K, in case of $\text{In}_{1.95}\text{Sn}_{0.05}\text{O}_3$ and for 5 h at 1,073 K in case of $\text{Ca}_3\text{Co}_4\text{O}_9$ with a heating and cooling rate of $3 \text{ min} \cdot \text{K}^{-1}$, respectively. The calcined powders were cold pressed and sintered. The n-type material $\text{In}_{1.95}\text{Sn}_{0.05}\text{O}_3$ was sintered for 15 h at 1,873 K with a heating and cooling rate of $3 \text{ min} \cdot \text{K}^{-1}$. The p-type material $\text{Ca}_3\text{Co}_4\text{O}_9$ was sintered for 10 h at 1,173 K with the same heating and cooling parameters. All steps, synthesis, calcination and sintering, were performed under ambient air conditions.

The phase compositions of synthesized powders and sintered ceramics for both materials were characterized by X-ray diffraction (XRD) using a Bruker D8 Advance with $\text{Cu-K}\alpha$ radiation. A time per step of 0.3 s, a step size of 0.0105° , a voltage of 40 kV and a current of 40 mA were applied for XRD measurement. Microstructural characterization was carried out by field-emission scanning electron microscope (FE-SEM) of the type JEOL JSM-6700F, which was equipped with an energy-dispersive X-ray spectrometer (EDXS) of the type Oxford Instruments INCA 300 for elemental analysis. N-type specimen were vibration-polished on a Buehler Vibromet-2 using 50 nm colloidal alumina suspension. P-type specimen were polished with a Struers Tegramin-20 using a multistep polishing program with colloidal diamond suspensions with grain sizes from 9 to $1 \mu\text{m}$. Density measurements were performed by an Archimedes setup using ISO 5018:1983 (the International Organization for Standardization) in which the dry mass, mass in solvent and wet mass of the sample, was measured. The coefficient of thermal expansion (CTE) was estimated in synthetic air using a dilatometer DIL 402 C from Netzsch.

To determine the thermoelectric properties of the chosen materials, electrical conductivity σ , Seebeck coefficient α and entropy conductivity measurements Λ were measured as a function of temperature. Thereby the power factor $\sigma \cdot \alpha^2$ and the figure of merit ZT of $\text{Ca}_3\text{Co}_4\text{O}_9$ as well as for $\text{In}_{1.95}\text{Sn}_{0.05}\text{O}_3$ were estimated. Thermoelectric properties were measured with a home-made measurement cell after Indris (2001). The used furnace is an ELITE thermal system. The electronic parameters were measured with KEITHLEY 2100 $6\frac{1}{2}$ Digit Multimeters. Data were acquired and converted using LAB VIEW software. The measurements of

the heat conductivity λ and entropy conductivity Λ , respectively were carried out by a laser flash setup LFA 457 MicroFlash from Netzsch.

Characterization of the thermoelectric generator and estimation of ZT of the module were realized with a load-resistance dependent measurement under steady-state conditions, as shown schematically in Figure 2.

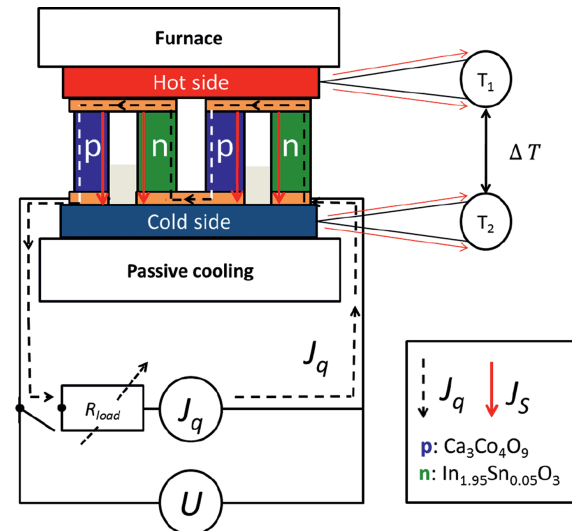


Figure 2: Sketch of the measurement setup to characterize the oxide-based thermoelectric generator in ambient air. Remind the alternating directions of coupling an entropy current J_S with an electrical current J_q in p- ($\alpha > 0$) and n-type ($\alpha < 0$) semiconducting legs. If a closed electrical circuit is present (closed switch), a circular electrical current (drawn in dotted lines) is driven by the entropy currents (red arrows), which expresses the power conversion. When the switch is open, the open circuit voltage is measured. Electrical current J_q and voltage U are measured with multimeters as a function of the load resistance R_{load} , which are adjusted by a variable resistor. The temperatures T_1 and T_2 and thereby the temperature difference ΔT between hot and cold side are measured with Pt-Rh thermocouples, which are operated in electrical open-circuit conditions. Here, entropy fluxes are present but small as compared to the ones running the generator.

Materials Properties

To verify the crystal structure and phase purity of n- and p-type powders and ceramics, XRD analyses were carried out. The $\text{Ca}_3\text{Co}_4\text{O}_9$ powder obtained after calcination at 1,073 K for 5 h is phase pure. After cold pressing and sintering at 1,173 K for 10 h a pure $\text{Ca}_3\text{Co}_4\text{O}_9$ ceramic was obtained. Comparing the powder pattern with the pattern of the $\text{Ca}_3\text{Co}_4\text{O}_9$ ceramic, a texture is visible (reflection 2010 (overbar on 2)); see Figure 3(a). Based on the results of

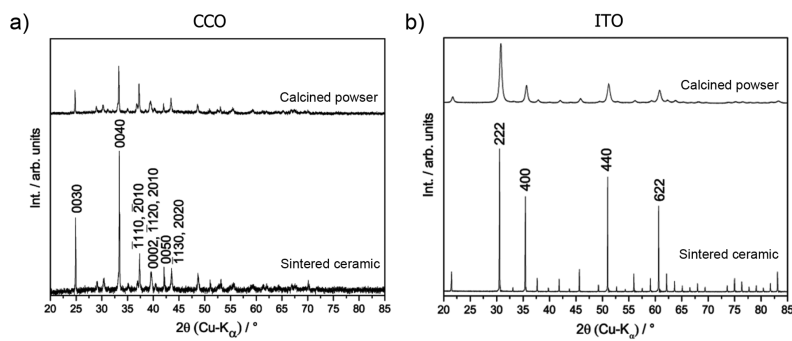


Figure 3: X-ray diffraction patterns of: a) CCO calcined powder and sintered ceramic, indexed reflections of superspace group Cm (0 1-p 0), equivalent to Bm (0 0 γ), no. 8.3; see Prince (2004) and b) ITO calcined powder and sintered ceramic, indexed reflections of space group Ia-3 (no. 206), taken from PDF-2 database (01-089-4596).

Miyazaki et al. (2002), a Rietveld refinement, utilizing Topas 4.2 software, was performed to analyze the $\text{Ca}_3\text{Co}_4\text{O}_9$ ceramic. The best results were accomplished for superspace group Cm (0 1-p 0), equivalent to Bm (0 0 γ), no. 8.3; see Prince (2004), the crystal system was monoclinic base-centered with $a = 4.84 \text{ \AA}$, $c = 10.84 \text{ \AA}$, $\beta = 96.11^\circ$ and $\alpha = \gamma = 90^\circ$. The b-axis was refined to be $b_1 = 2.82 \text{ \AA}$ for the CoO_2 subsystem and $b_2 = 4.55 \text{ \AA}$ for the Ca_2CoO_3 subsystem; see Miyazaki et al. (2002). For the n-type material $\text{In}_{1.95}\text{Sn}_{0.05}\text{O}_3$, a pure nanopowder is obtained after calcination at 973 K for 10 h. The powder got pressed and sintered at 1,873 K for 15 h and a pure $\text{In}_{1.95}\text{Sn}_{0.05}\text{O}_3$ ceramic was

obtained; see Figure 3(b). It crystallized in space group Ia-3 (no. 206) in a cubic body-centered unit cell with $a = 10.12 \text{ \AA}$, taken from PDF-2 database (01-089-4596).

For microstructural characterization of the thermoelectric materials by SEM, the sintered ceramics were prepared by polishing steps. The n-type ceramic was treated with a multistep polishing program followed by vibration polishing. The p-type material was also prepared with a multistep polishing program finished with a fine polishing step with a diamond grains solution. Figure 4 reveals the results of microstructural investigation of the n-type $\text{In}_{1.95}\text{Sn}_{0.05}\text{O}_3$ and p-type $\text{Ca}_3\text{Co}_4\text{O}_9$ materials.

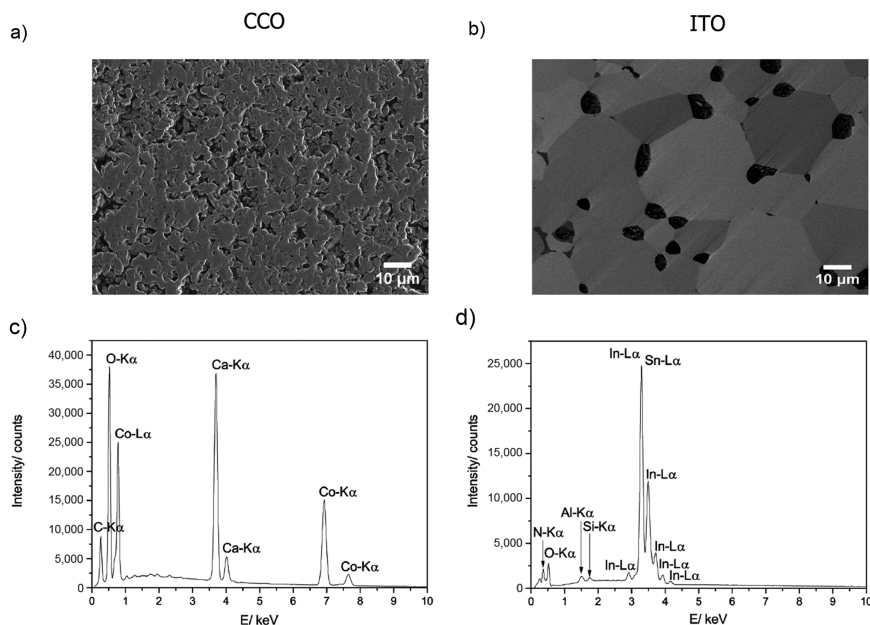


Figure 4: a,b) Sintered ceramics prepared by a single polishing program for $\text{Ca}_3\text{Co}_4\text{O}_9$ sample, and polishing and vibration-polishing program for $\text{In}_{1.95}\text{Sn}_{0.05}\text{O}_3$ sample, analyzed cross-section in SEM, c,d) EDX spectra of $\text{Ca}_3\text{Co}_4\text{O}_9$ and $\text{In}_{1.95}\text{Sn}_{0.05}\text{O}_3$ ceramic.

The SEM investigations of the $\text{Ca}_3\text{Co}_4\text{O}_9$ polished sample shown in Figure 4(a) exhibits no visible grain distribution of the p-type material. The sintered $\text{Ca}_3\text{Co}_4\text{O}_9$ ceramic shows a high porosity with a connected pore network. Figure 4(c) shows the EDX spectra of the $\text{Ca}_3\text{Co}_4\text{O}_9$ sample, a C peak due to the polishing steps is obtained in the spectrum but no other impurities. The SEM investigations in Figure 4(b, d), of the vibration-polished $\text{In}_{1.95}\text{Sn}_{0.05}\text{O}_3$ sample, show grain sizes which are varying from 10 to 40 μm . The sample possesses a closed porosity. The pores are isolated and do not form a network. An Al peak was detected in the EDX spectrum, shown in Figure 4(d). This can be explained by the insertion of Al_2O_3 nanoparticles into the pores during the vibration-polishing step. In the elemental distribution analysis made by EDX no impurities are visible except those of the polishing steps, i. e. Al and Si.

Density measurements of the n-type $\text{In}_{1.95}\text{Sn}_{0.05}\text{O}_3$ and p-type $\text{Ca}_3\text{Co}_4\text{O}_9$ materials were performed with an Archimedes setup. For the n-type material, 92.12% of the theoretical density could be achieved. The sintered $\text{Ca}_3\text{Co}_4\text{O}_9$ sample achieved a theoretical density of 54.0% only. Table 1 shows the measured values for the

Table 1: Measured values of density and porosity of $\text{In}_{1.95}\text{Sn}_{0.05}\text{O}_3$ (15 h at 1,873 K) and $\text{Ca}_3\text{Co}_4\text{O}_9$ (10 h at 1,173 K) ceramic, using ISO 5018:1983 (the International Organization for Standardization).

Material	Bulk density/ $\text{g}\cdot\text{cm}^{-3}$	True density/ $\text{g}\cdot\text{cm}^{-3}$	Open porosity/%	Closed porosity/%	True porosity/%
$\text{In}_{1.95}\text{Sn}_{0.05}\text{O}_3$	6.55	7.11	3.48	4.46	7.94
$\text{Ca}_3\text{Co}_4\text{O}_9$	2.53	4.68	45.2	0.64	45.8

density of the bulk ceramic as well as calculated values for open porosity, true porosity and closed porosity for both materials.

These measurements confirm the SEM investigations. $\text{In}_{1.95}\text{Sn}_{0.05}\text{O}_3$ possesses a low open porosity and a slightly higher closed porosity. $\text{Ca}_3\text{Co}_4\text{O}_9$ exhibits a high open porosity and almost no closed porosity. This indicates that there is a connected network present between the pores. The coefficient of thermal expansion was measured with a dilatometer from Netzsch 402C as a function of temperature for $\text{In}_{1.95}\text{Sn}_{0.05}\text{O}_3$ and $\text{Ca}_3\text{Co}_4\text{O}_9$ ceramics. Starting from powder samples, two dilatometer measurements were performed. First cycles represent the sintering curves for $\text{In}_{1.95}\text{Sn}_{0.05}\text{O}_3$ and $\text{Ca}_3\text{Co}_4\text{O}_9$ samples, respectively. The second cycles depict the dilatometer measurements, shown in Figure 5(a, b). Figure 5(a, b) shows the quotient of the variation in length and initial length dL/L_0 in percent as a function of temperature, the value of the CTE during heating and cooling was estimated from the measured values (dashed lines). The CTE between 400 °C and 900 °C during heating and cooling exhibits almost the same value of $14.7 \cdot 10^{-6}\text{K}^{-1}$ for $\text{In}_{1.95}\text{Sn}_{0.05}\text{O}_3$. The CTE of $\text{Ca}_3\text{Co}_4\text{O}_9$ between 673 K and 1073 K represents $15.0 \cdot 10^{-6}\text{K}^{-1}$ during heating and $18.1 \cdot 10^{-6}\text{K}^{-1}$ during cooling, respectively.

Figure 6(a, b) shows the measured values for σ and α of $\text{In}_{1.95}\text{Sn}_{0.05}\text{O}_3$ and $\text{Ca}_3\text{Co}_4\text{O}_9$ as a function of temperature. The electrical conductivity σ of $\text{Ca}_3\text{Co}_4\text{O}_9$ is almost constant over the whole temperature range and reaches $32.5 \text{ S}\cdot\text{cm}^{-1}$ at 1,073 K. The electrical conductivity of $\text{In}_{1.95}\text{Sn}_{0.05}\text{O}_3$ increases exponentially at about 900 K and achieves $608 \text{ S}\cdot\text{cm}$ at 1,073 K. The Seebeck coefficient α of $\text{Ca}_3\text{Co}_4\text{O}_9$ is almost constant from 500 to 1,100 K and decreases to lower temperatures. The α value of $\text{In}_{1.95}\text{Sn}_{0.05}\text{O}_3$ increases slightly with temperature. The

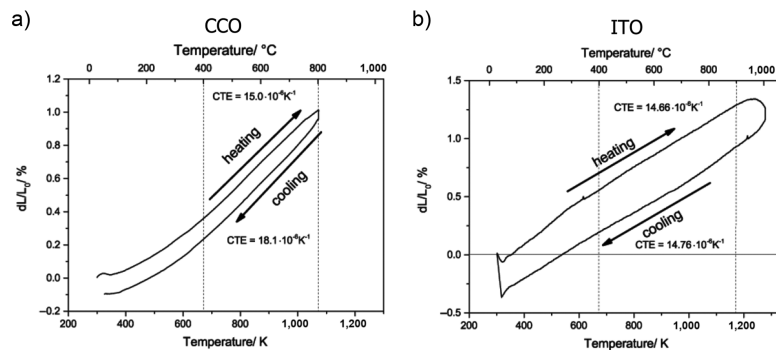


Figure 5: Coefficient of thermal expansion (CTE): thermal expansion and shrinkage during heating and cooling as a function of temperature of a) $\text{Ca}_3\text{Co}_4\text{O}_9$ and b) $\text{In}_{1.95}\text{Sn}_{0.05}\text{O}_3$ ceramic. Dashed lines indicate the temperature ranges for which the CTE was estimated, respectively.

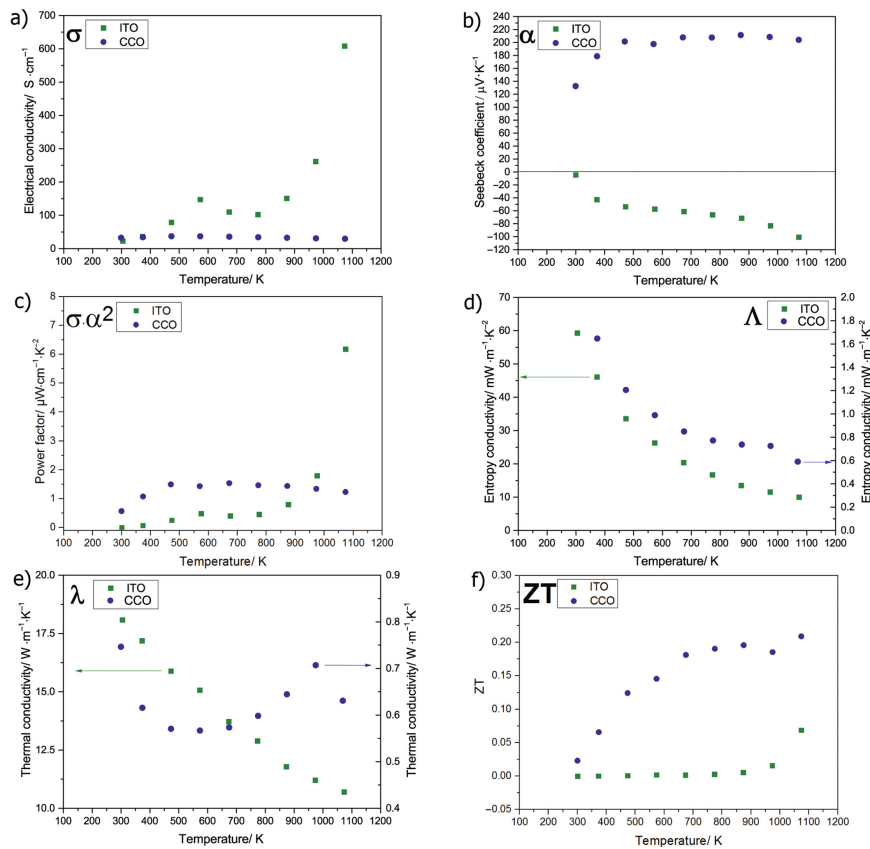


Figure 6: Thermoelectric properties as a function of temperature of n-type $\text{In}_{1.95}\text{Sn}_{0.05}\text{O}_3$ (squares, ITO) and p-type $\text{Ca}_3\text{Co}_4\text{O}_9$ (circles, CCO). a) Electrical conductivity σ and b) Seebeck coefficient α . c) power factor $\sigma \cdot \alpha^2$, d) entropy conductivity Λ , e) heat conductivity λ (eq. [2]) and f) figure of merit ZT , estimated according to eq. [1].

Seebeck values for both materials reach $203.8 \mu\text{V} \cdot \text{K}^{-1}$ and $-100.8 \mu\text{V} \cdot \text{K}^{-1}$ at 1,073 K, respectively. The values for tin-doped indium oxide are in the same order as those reported by Guilmeau et al. (2009). The electrical conductivity σ of $\text{Ca}_3\text{Co}_4\text{O}_9$ differs in absolute values, and the course of the Seebeck coefficient α turns slightly different, due to a lower density of the ceramic, compared to other studies, see Rasekh et al. (2013) and Xu et al. (2002). The values for the power factor in Figure 6(c) of $\text{Ca}_3\text{Co}_4\text{O}_9$ and $\text{In}_{1.95}\text{Sn}_{0.05}\text{O}_3$, calculated from σ and α differ between 300 and 900 K. The power factor of $\text{In}_{1.95}\text{Sn}_{0.05}\text{O}_3$ exceeds that of $\text{Ca}_3\text{Co}_4\text{O}_9$ after 1,000 K due to an exponential increase in the electrical conductivity. The figure of merit ZT of $\text{In}_{1.95}\text{Sn}_{0.05}\text{O}_3$ and $\text{Ca}_3\text{Co}_4\text{O}_9$ were estimated from the ciphered power factors $\sigma \cdot \alpha^2$, of $6.8 \mu\text{W} \cdot \text{cm}^{-1} \cdot \text{K}^{-2}$ (ITO), and $1.23 \mu\text{W} \cdot \text{cm}^{-1} \cdot \text{K}^{-2}$ (CCO) and the entropy conductivity Λ respectively, which was measured via a laser flash setup.

Figure 6(d) shows the entropy conductivity Λ of $\text{In}_{1.95}\text{Sn}_{0.05}\text{O}_3$ and $\text{Ca}_3\text{Co}_4\text{O}_9$ as a function of the temperature. And Figure 6(f) shows the calculated figure of merit of $\text{In}_{1.95}\text{Sn}_{0.05}\text{O}_3$ and $\text{Ca}_3\text{Co}_4\text{O}_9$ after eq. [1] as a function of temperature. The entropy conductivity Λ reaches $10 \text{mW} \cdot \text{m}^{-1} \cdot \text{K}^{-2}$ at 1,073 K for $\text{In}_{1.95}\text{Sn}_{0.05}\text{O}_3$ and $0.59 \text{mW} \cdot \text{m}^{-1} \cdot \text{K}^{-2}$ for $\text{Ca}_3\text{Co}_4\text{O}_9$. The estimated figure of merit for $\text{In}_{1.95}\text{Sn}_{0.05}\text{O}_3$ and $\text{Ca}_3\text{Co}_4\text{O}_9$ as a function of temperature achieve 0.07 and 0.21 at 1,073 K, respectively. The measured values for the heat conductivity λ of $10.6 \text{W} \cdot \text{m}^{-1} \cdot \text{K}^{-1}$ at 1,073 K for a $\text{In}_{1.95}\text{Sn}_{0.05}\text{O}_3$ sample vary slightly, compared to $8.5 \text{W} \cdot \text{m}^{-1} \cdot \text{K}^{-1}$ at 1,000 K for an indium oxide sample, which is doped with the same tin fraction, reported by Guilmeau et al. (2009). Because of a slightly lower heat conductivity λ reported in literature, the ZT value in this study also differs a little from literature, maybe because of a different density of the measured samples. The trend for the heat conductivity λ

and the measured values of $0.63 \text{ W} \cdot \text{m}^{-1} \cdot \text{K}^{-1}$ at 1,073 K for $\text{Ca}_3\text{Co}_4\text{O}_9$ also differ compared to the trend and value of $1.7 \text{ W} \cdot \text{m}^{-1} \cdot \text{K}^{-1}$ at 1,073 K, reported by Nong, Liu, and Ohtaki (2010). According to this trend, the value of $0.63 \text{ W} \cdot \text{m}^{-1} \cdot \text{K}^{-1}$ at 1,073 K seems to be undersized. This can be attributed to a lower density and high open porosity of the measured $\text{Ca}_3\text{Co}_4\text{O}_9$ sample, allowing gas to permeate and thus contributing to the heat conductivity. The figure of merit ZT matches with the reported values in literature.

Thermoelectric Generator

To assemble a thermoelectric generator, legs of n- and p-type semiconductor materials were cut out of disk-shaped ceramics, utilizing a wire saw. The n-type $\text{In}_{1.95}\text{Sn}_{0.05}\text{O}_3$ legs have an area of 1.1 mm^2 and a length of 2 mm. The p-type $\text{Ca}_3\text{Co}_4\text{O}_9$ legs possess an area of 1.5 mm^2 and a length of 2 mm. The constructed oxide-based thermoelectric generator consists of 5 n-type $\text{In}_{1.95}\text{Sn}_{0.05}\text{O}_3$ and 5 p-type $\text{Ca}_3\text{Co}_4\text{O}_9$ legs. The legs were connected to each other on the top and bottom plate via a gold connector. The gold connector was placed on the electrical insulating Al_2O_3 plates via coating of an Au-paste from HERAEUS. The legs were placed on a Al_2O_3 plate in electrical serial connection. The Al_2O_3 plates are rectangles with 15 mm lateral lengths. Platinum wires were attached for electrical contacting to an external electrical circuit. The manufactured module

was baked at 1,173 K for 2 hours to obtain a mechanically stable device with metallic gold contacts.

Figure 7 shows a sketch of the thermoelectric generator and a side view of the constructed TEG with n- and p-type legs, contacts, Al_2O_3 -plates and Pt-wires. The oxide-based thermoelectric generator was characterized at high-temperature conditions in air. Figure 2 shows the utilized measurement setup schematically. The upper side of the generator was heated by a furnace up to $T_{hot} = 1,073 \text{ K}$ while the bottom side was cooled by a passive cooler (T_{cold}) to establish a temperature gradient over the device obtaining a temperature drop of $\Delta T = 113 \text{ K}$. Two Pt/Rh thermocouples measure the temperature at the hot and cold side, respectively and thereby ΔT . The generator is connected with a voltmeter and an amperemeter in parallel connection. The electrical power output of the generator can be measured if a variable resistor is prior to the amperemeter. The electrical power output is maximum if the resistivity of the module is equal to the load resistivity. The thermoelectric generator couples an entropy current J_S and an electric current J_q in a way that energy is transferred from thermal to electric process; see Figure 2. An oxide-based generator possesses a good thermal, chemical stability in oxidizing atmosphere and a conventional TEG setup provides also good mechanical stability. Oxides own still inferior thermoelectric properties, so improvement is needed for Seebeck coefficient α and entropy conductivity Λ of $\text{In}_{1.95}\text{Sn}_{0.05}\text{O}_3$ and electrical conductivity σ and entropy conductivity Λ of $\text{Ca}_3\text{Co}_4\text{O}_9$. After a period of time of 1 hour, the device was in equilibrium and the variable

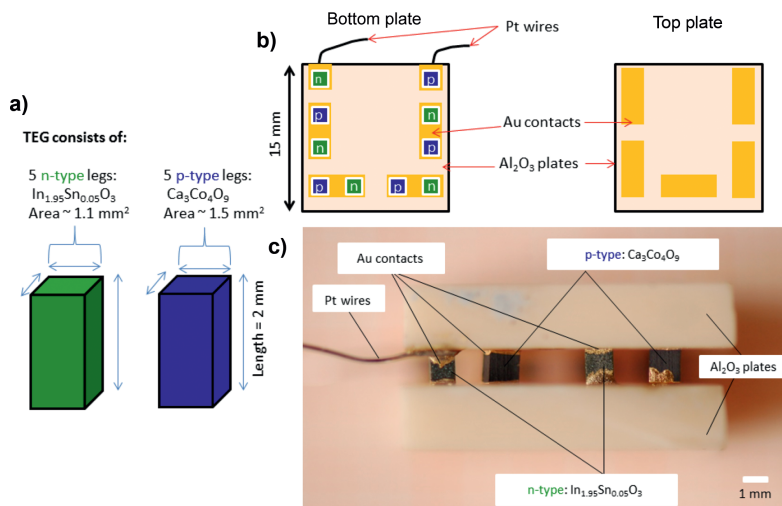


Figure 7: a) Dimensions of n- and p-type legs, b) sketch of TEG setup, c) side-view photograph of the TEG.

resistor in the external circuit was switched and thereby different load resistances R_{load} were applied. The electrical parameters electrical current J_q and voltage U were measured in dependence of R_{load} and different T_{hot} . Every measuring step last 5 min. The first measurement was always under quasi closed-circuited conditions, this means without any load resistance R_{load} other than the internal resistance by cables etc. The electrical power output P_{el} of the device is related to the current and the voltage, while the area-specific electrical power density ω_{el} depends on the quotient of the power output P_{el} and the area of the device. The electrical power output P_{el} was estimated by multiplying the measured values of U and J_q . The area-specific electrical power density was calculated by dividing P_{el} with the area of 2.25 cm^2 . Figure 8 shows the measured data points and continuously fitted plots of U and P_{el} as a function of J_q . The maximum electrical power output $P_{el,max}$, the associated electrical current $J_q(P_{max})$ and voltage $U(P_{max})$ can be estimated and read from the fitted data plots. The short-circuit current $J_{q,sc}$ and open-circuit voltage U_{OC} can also be

determined from the fitted plots in Figure 8. The calculated values of the electrical power density of $\omega_{el} = 2.13 \text{ mW} \cdot \text{cm}^{-2}$ at $T_{hot} = 1,073 \text{ K}$, $\omega_{el} = 1.6 \text{ mW} \cdot \text{cm}^{-2}$ at $T_{hot} = 1,023 \text{ K}$ and $\omega_{el} = 1.36 \text{ mW} \cdot \text{cm}^{-2}$ at $T_{hot} = 973 \text{ K}$ are also plotted in Figure 8. The TEG possesses a fill factor of 5.78% when an area of the p,n couples of 0.13 cm^2 and an area of the top and bottom plates of 2.25 cm^2 are assumed. The measured thermoelectric parameters of the device at different applied steady-state temperature conditions are listed in Table 2. The electrical power output P_{el} depends on the load-resistance R_{load} in the external circuit, which can be expressed by eq. [5].

The maximum electrical power output is a load-resistance dependent parameter. It becomes maximal if the load resistance R_{load} is equal to R_{module} after eq. [6]; see Möschwitzer and Lunze (1998).

$$P_{el} = \frac{U_{OC}^2}{4 \cdot R_{load} \cdot \frac{U_{OC} - U_{load}}{U_{load}}} \quad [5]$$

$$R_{load} = R_{module} = \left(\sum R_n + \sum R_p \right) \quad [6]$$

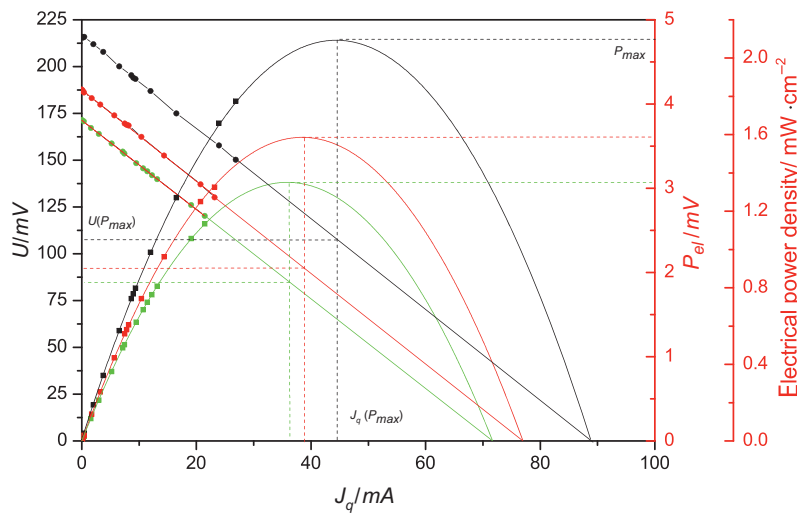


Figure 8: Fitted electrical power output P_{el} (rectangular dots) and voltage (spherical dots) as a function of the electrical current J_q at different applied T_{hot} temperatures (1,073 K in black, 1,023 K in red and 973 K in green). $U(P_{max})$ and $J_q(P_{max})$ of the respective $P_{el,max}$ at different temperature conditions are indicated (dashed lines).

Table 2: Measured and calculated values of the thermoelectric generator at different applied temperature conditions.

T_{hot}/K	$\Delta T/K$	R_{module}/Ω	U_{OC}/mV	$J_{q,sc}/mA$	$U(P_{max})/mV$	$J_q(P_{max})/mA$	P_{max}/mW
1,073	113	2.44	216.51	88.65	108.25	44.32	4.8
1,023	113	2.43	187.83	77.18	93.91	38.59	3.62
973	113	2.39	171.46	71.67	85.73	35.83	3.06

At the maximum power output, when R_{load} is equal to R_{module} (eq. [6]) and $U_{load} = \frac{1}{2}U_{OC}$, eq. [5] becomes eq. [7].

$$P_{max} = \frac{U_{OC}^2}{4 \cdot R_{module}} \quad [7]$$

The measured and calculated parameters of the TEG are listed in Table 2. The maximum electrical power output $P_{el,max}$ of the thermoelectric generator for three different applied temperatures, when a temperature difference of 113 K is established, can be read from the extrapolated curves. At a hot-side temperature of $T_{hot} = 1073\text{ K}$, the TEG provides an electrical power output of $P_{el} = 4.8\text{ mW}$, at $T_{hot} = 1,023\text{ K}$, $P_{el} = 3.62\text{ mW}$ and at $T_{hot} = 973\text{ K}$, $P_{el} = 3.06\text{ mW}$. The $U(P_{max})$ and $J_q(P_{max})$ of the respective $P_{el,max}$ at different temperatures can be read from the linearly extrapolated $U - J_q$ plot. The values for U_{OC} were measured and $J_{q,SC}$ values were extrapolated from the measured $U - J_q$ curves.

The figure of merit ZT of the generator can be calculated from these measured values by eq. [8] after Min and Rowe (2001). At a hot-side temperature of $T_{hot} = 1,073\text{ K}$ and an applied temperature drop of $\Delta T = 113\text{ K}$, a figure of merit of 0.02 can be reached. This value for the whole generator is similar to the value for the material $\text{In}_{1.95}\text{Sn}_{0.05}\text{O}_3$, see Figure 6f, which is the efficiency-limiting part of the generator.

$$ZT = \frac{U_{OC}}{J_{q,SC} \cdot R_{module}} - 1 \quad [8]$$

An oxide-based TEG made of $\text{In}_{1.95}\text{Sn}_{0.05}\text{O}_3$ and $\text{Ca}_3\text{Co}_4\text{O}_9$ provides a better balance of voltage U and current $J_q(U(P_{max})) = 108.25\text{ mV}$, $J_q(P_{max}) = 44.32\text{ mA}$ and thus a high electrical power output, compared with a generator made of ZnO and $\text{Ca}_3\text{Co}_4\text{O}_9$, see Feldhoff and Geppert (2014), which offers not more than 0.55 mW at an almost doubled temperature difference. Nevertheless it is difficult to compare thermoelectric generators with each other due to the different dimensions of the n- and p-type legs, different applied temperatures and temperature differences, see Choi et al. (2011) and Matsubara et al. (2001). But if we consider that the electrical power output depends on the product of U and J_q , the combination of $\text{In}_{1.95}\text{Sn}_{0.05}\text{O}_3$ and $\text{Ca}_3\text{Co}_4\text{O}_9$ possess beneficial properties for power generation at high-temperature conditions in ambient atmosphere.

Conclusions

An oxide-based thermoelectric generator consisting of n-type $\text{In}_{1.95}\text{Sn}_{0.05}\text{O}_3$ and p-type $\text{Ca}_3\text{Co}_4\text{O}_9$ semiconductor

legs was successfully constructed and characterized. The maximum electric power output depends and increases with increasing hot-side temperature. A high voltage and electric current is advantageous and could be accomplished by the use of a highly electrically conductive $\text{In}_{1.95}\text{Sn}_{0.05}\text{O}_3$ n-type material. The efficiency of the whole system is limited by the figure of merit ZT of the $\text{In}_{1.95}\text{Sn}_{0.05}\text{O}_3$ n-type legs. A ZT value of 0.02 for the device was achieved and a maximum electric power output of 4.8 mW was obtained at 1,073 K hot-side temperature and a temperature difference of $\Delta T = 113\text{ K}$. To improve the power output of the thermoelectric generator, the cross sections of the electric conductors can be adapted to each other in terms of the specific resistance.

References

- Bérardan, D., E. Guilmeau, A. Maignan, and B. Raveau. 2008. "Enhancement of the Thermoelectric Performances of In_2O_3 by the Coupled Substitution of $\text{M}^{2+}/\text{Sn}^{4+}$ for In^{3+} ." *Journal of Applied Physics* 104:064918–1–064918–5.
- Choi, S. M., K. H. Lee, C. H. Lim, and W. S. Seo. 2011. "Oxide-Based Thermoelectric Power Generation Module Using p-Type $\text{Ca}_3\text{Co}_4\text{O}_9$ and n-Type $(\text{ZnO})_7\text{In}_2\text{O}_3$ Legs." *Energy Conversion and Management* 52:335–9.
- Feldhoff, A. 2015. "Thermoelectric Material Tensor Derived From the Onsager - De Groot - Callen Model." *Energy Harvesting and Systems* 2 (1):5–13.
- Feldhoff, A., M. Arnold, J. Martynczuk, T. Gesing, and H. Wang. 2008. "The Sol-Gel Synthesis of Perovskites by EDTA/Citrate Complexing Method Involves Nanoscale Solid State Reactions." *Solid State Sciences* 10:689–701.
- Feldhoff, A., and B. Geppert. 2014. "A High-Temperature Thermoelectric Generator Based on Oxides." *Energy Harvesting and Systems* 1 (1–2):69–78.
- Fuchs, H. 2010. *The Dynamics of Heat – a Unified Approach to Thermodynamics and Heat Transfer*, Graduate Texts in Physics, 2nd ed. New York: Springer.
- Guilmeau, E., D. Bérardan, C. Simon, A. Maignan, B. Raveau, D. Ovono Ovono, and F. Delorme. 2009. "Tuning the Transport and Thermoelectric Properties of In_2O_3 Build Ceramics Through Doping at In-Site." *Journal of Applied Physics* 106:053715–1–053715–7.
- Indris, S. 2001. *Perkolaton Von Grenzflächen in Nanokristallinen Keramischen Kompositen - Li-Ionenleitfähigkeit Und 7li-NMR-Relaxation*. Göttingen: Cuvillier.
- Ioffe, A. 1957. *Semiconductor Thermoelements and Thermoelectric Cooling*, 1st ed. London: Infosearch Ltd.
- Kenfaui, D., G. Bonnefont, D. Chateigner, G. Fantozzi, M. Gomina, and J. G. Noudem. 2010. " $\text{Ca}_3\text{Co}_4\text{O}_9$ Ceramics Consolidated by SPS Process: Optimisation of Mechanical and Thermoelectric Properties." *Material Research Bulletin* 45:1240–9.
- Liu, Y., Y. Lin, Z. Shi, and C. Nan. 2005. "Preparation of $\text{Ca}_3\text{Co}_4\text{O}_9$ and Improvement of Its Thermoelectric Properties by Spark Plasma Sintering." *Journal of the American Ceramic Society* 88:1337–40.

- Matsubara, I., R. Funahashi, T. Takeuchi, and S. Sodeoka. 2001. "Fabrication of an All-Oxide Thermoelectric Power Generator." *Applied Physics Letters* 78:3627–9.
- Min, G., and D. Rowe. 2001. "A Novel Principle Allowing Rapid and Accurate Measurement of a Dimensionless Thermoelectric Figure of Merit." *Measurement Science and Technology* 12:1261–2.
- Miyazaki, Y. 2004. "[Crystal Structure and Thermoelectric Properties of the Misfit-Layered Cobalt Oxides.](#)" *Solid State Ionics* 172:463–7.
- Miyazaki, Y., M. Onoda, T. Oku, M. Kikuchi, Y. Ishii, Y. Ono, Y. Morii, and T. Kajitani. 2002. "Modulated Structure of Thermoelectric Compound $[\text{Ca}_2\text{CoO}_3]\text{CoO}_2$." *Journal of the Physical Society of Japan* 71:491–7.
- Möschwitzer, A., and K. Lunze. 1998. *Lehrbuch Halbleiterelektronik*, 8th ed. Heidelberg: Dr. Alfred Hüthig Verlag.
- Nagahama, D., T. Tani, Y. Masuda, H. Itahara, T. Yonezawa, and K. Koumoto. 2002. "Thermoelectric Properties of $\text{Ca}_3\text{Co}_{4-x}\text{Ga}_x\text{O}_9$ -Based Ceramics Textured by Templated Grain Growth Method." *21st International Conference on Thermoelectrics* 21:211–14.
- Nong, N. V., C. -J. Liu, and M. Ohtaki. 2010. "Improvement on the High Temperature Thermoelectric Performance of Ga-Doped Misfit-Layered $\text{Ca}_3\text{Co}_{4-x}\text{Ga}_x\text{O}_{9+\delta}$ ($x = 0, 0.05, 0.1, \text{ and } 0.2$)." *Journal of Alloys and Compounds* 491:53–6.
- Prince, E. 2004. *International Tables for Crystallography*, volume C ed. Dordrecht/Boston/London: Kluwer Academic Publishers.
- Rasekh, S., M. A. Torres, G. Constantinescu, M. A. Madre, J. C. Diez, and A. Sotelo. 2013. "Effect of Cu by Co Substitution on $\text{Ca}_3\text{Co}_4\text{O}_9$ Thermoelectric Ceramics." *Journal of Materials Science: Materials in Electronics* 24:2309–14.
- Rowe, D. 1995. *CRC Handbook of Thermoelectrics*, 89th ed. Boca Raton, FL: CRC Press.
- Seeger, K. 1991. *Semiconductor Physics*. Berlin: Springer.
- Singh, D. J. 2000. "[Electronic Structure of \$\text{NaCo}_2\text{O}_4\$.](#)" *Physical Review B* 61:13397–402.
- Xu, G., R. Funahashi, M. Shikano, I. Matsubara, and Y. Zhou. 2002. "Thermoelectric Properties of the Bi-Na-Substituted $\text{Ca}_3\text{Co}_4\text{O}_9$ System." *Applied Physics Letters* 80:3760–2.
- Yan, Y. L., and Y. X. Wang. 2012. "Electronic Structure and Low Temperature Thermoelectric Properties of $\text{In}_{24}\text{M}_8\text{O}_{48}$ ($\text{M} = \text{Ge}^{4+}, \text{Sn}^{4+}, \text{Ti}^{4+}, \text{ and } \text{Zr}^{4+}$)." *Journal of Computational Chemistry* 33:88–92.

3.3 An Approach to a Flexible Thermoelectric Generator Fabricated using Bulk Materials

Benjamin Geppert and Armin Feldhoff

Energy Harvesting and Systems, 3(2), 161-171, (2015)

B. Geppert* and A. Feldhoff

An Approach to a Flexible Thermoelectric Generator Fabricated using Bulk Materials

DOI 10.1515/ehs-2015-0015

Abstract: A prototype flexible thermoelectric generator fabricated with bulk materials is presented. Mineral-fiber band and copper tape are used as flexible substrate and electric connectors, respectively, to coil up the constructed thermoelectric device under investigation. The applied active thermoelectric materials are $\text{Ca}_3\text{Co}_4\text{O}_9$ ceramic and Cu-Ni alloy for hole and electron conduction, respectively. Thermal parallel and electric series connections of the mentioned materials were realized in the prototype flexible thermoelectric generator. The device delivered an open-circuit voltage of 16.52 mV and a short-circuit current of 19.40 μA with a temperature difference of $\Delta T_{\text{TEG}} = 31$ K for the hot side temperature of 420 K. The device exhibits an approximately 3 cm long stripe that include four basic units (n-p pair and electric connector).

Introduction

Studies on thermoelectric systems focus on thermoelectrically active materials and on entire thermoelectric devices that consist of different materials. Hence, thermoelectric investigations are highly interdisciplinary and involve fields ranging from solid state chemistry, for the development of new materials, to fabrication engineering, including geometric and electronic research. The crucial quantities in determining the thermoelectric properties of a material are the isothermal ($\vec{\nabla}T = 0$) specific electric resistivity ρ , the Seebeck coefficient α (from thermovoltage) and the specific entropy conductivity Λ at electric open-circuit conditions ($\vec{j}_q = 0$); see Fuchs (2010, 2014), Feldhoff (2015). The coupled potential gradients for entropy $\vec{\nabla}T$ and charge $\vec{\nabla}\varphi$ and the related generated entropy flux density \vec{j}_S and charge flux density \vec{j}_q can be quantitatively described in terms of thermoelectric quantities, considering a thermoelectric material tensor that includes all of the measurable thermoelectric properties that determine the thermoelectric performance of a

particular material. The array presentation for the thermoelectric description is shown in eq. [1]; see Feldhoff (2015), Geppert et al. (2015):

$$\begin{pmatrix} \vec{j}_S \\ \vec{j}_q \end{pmatrix} = - \begin{pmatrix} \frac{\alpha}{\rho} + \Lambda & \frac{\alpha}{\rho} \\ \frac{\alpha}{\rho} & \frac{1}{\rho} \end{pmatrix} \cdot \begin{pmatrix} \vec{\nabla}T \\ \vec{\nabla}\varphi \end{pmatrix} \quad [1]$$

The leg-area related flux densities for the entropy \vec{j}_S and charge \vec{j}_q with the cross-sectional area \vec{A}_{leg} of the regarded legs give the absolute fluxes J_S and J_q according to:

$$J_S = \vec{j}_S \cdot \vec{A}_{\text{leg}} \quad [2]$$

$$J_q = \vec{j}_q \cdot \vec{A}_{\text{leg}} \quad [3]$$

In addition to trying to apply certain materials to certain temperature conditions, the geometric properties of a complete thermoelectric generator (TEG) must be considered. Many studies have considered $\text{Bi}_{2-x}\text{Sb}_x\text{Te}_3$ -based materials or metals such as Ni and Cu; see Kuznetsov et al. (2002), Poudel et al. (2008). The construction of a TEG requires an electrical series-connection of a hole conductor ($\alpha > 0$), where the motions of thermal and electric fluxes are directed in the same direction and an electron conductor ($\alpha < 0$), where the thermal and electric fluxes are directed in the opposite directions; see Feldhoff and Geppert (2014). The materials connected in electronic series are called legs and are commonly connected using metallic (e.g., copper) connectors. If the device is placed in a gradient of thermal potential $\vec{\nabla}T$, an electric potential $\vec{\nabla}\varphi$ builds up, and, according to eq. [1], coupled fluxes are generated for the entropy current density \vec{j}_S and electric current density \vec{j}_q . In the case of high charge carrier densities (compared with isolating materials), the potential gradients $\vec{\nabla}$ along the length L_{leg} of the applied legs can be expressed as drops (differences) Δ in terms of the considered potentials for entropy and charge.

$$\frac{\vec{\nabla}T}{L_{\text{leg}}} = \Delta T \quad [4]$$

$$\frac{\vec{\nabla}\varphi}{L_{\text{leg}}} = \Delta\varphi \quad [5]$$

Hence, a TEG is a device that transfers energy from an entropy current to an electric current; see Fuchs (2010, 2014), Feldhoff (2015). These properties make a

*Corresponding author: B. Geppert, Institute of Physical Chemistry and Electrochemistry, Leibniz Universität Hannover, Germany, E-mail: benjamin.geppert@pci.uni-hannover.de

A. Feldhoff, Institute of Physical Chemistry and Electrochemistry, Leibniz Universität Hannover, Germany

thermoelectric generator that is useful for recovering waste heat in different processes.

Most of the current studies on flexible or even coilable thermoelectric systems are based on thin-film or at least thick-film technology. Thin-film fabrication often uses $\text{Bi}_{2-x}\text{Sb}_x\text{Te}_3$, which is the most efficient and prominent system for application in the 300–473 K range; see Cao et al. (2014) and Francioso et al. (2011). Flexible harvesters were also fabricated using metals such as Cu and Ni, see Glatz, Munwyler, and Hierold (2006). Studies have also been performed on flexible TEGs using polymer-based composites; see Suemori, Hoshino, and Ka-mata (2013), Stepien et al. (2015). Using bulk materials (pressed and sintered) the physical properties as electric resistivity, thermovoltage and mechanical stability are superior compared to those of deposited versions of the same material. Due to the techniques of thin- or thick-film production, the grains of the materials are not necessarily contacted in either sintered ceramics or metals. Compared to bulk Bi-Te, electrochemically deposited Bi-Te films exhibit higher specific electric resistance values and smaller Seebeck coefficient values; see Yoo et al. (2005). Applying bulk fabrication avoids the requirement for elaborate equipment that is typically required for thin-film fabrication of the thermoelectric materials using techniques such as sputtering, printing or growing (e.g., electrochemical deposition). The contact of grains inside the film can also be a problem for printing. (Bi, Sb)-Te films obtained by screen-printing technologies can exhibit a higher electric resistance compared with that of the bulk material. The films must be densified by cold-pressing to decrease the specific electric resistance and increase the Seebeck coefficient; see Cao et al. (2014).

The present approach allows the inclusion of different material classes, as oxides and metals, without considering the contact of the grains forming the entire bulk phase. Furthermore, the costs of the $\text{Bi}_{2-x}\text{Sb}_x\text{Te}_3$ compounds are higher than those of the materials that we intend to use in our device. A summary of material costs for thermoelectrics is presented by LeBlanc et al. (2014). Conventional systems often include ceramic bottom- and top-plates with the series connection of thermoelectric legs in between. After connecting the legs electrically, the system is closed and can only be opened by disconnecting the assembled materials. Therefore, a coilable TEG exhibits advantageous fabrication. Because the TEG stripe is prepared as a geometrically open system, it is easier to connect the thermoelectric legs to the metallic connector without producing any electric short-circuits that must be avoided. In conventional rigid devices, the prepared electric connectors have to be added very precisely to maximize the leg density. We built devices using

both the rigid approach and the flexible approach. In our opinion, upscaling is easier using the approach of first fabricating an open stripe TEG, and then packing it into a dense system (e.g., via coiling up the stripe). Therefore, a stripe TEG is easier to assemble than is a conventional “chess-pattern” geometry. A flexible prototype thermoelectric generator was fabricated using bulk materials. Mineral-fiber band as flexible substrate enables the coiling of the constructed thermoelectric system under investigation. For n-type legs, Cu-Ni alloy was applied, whereas the p-type leg was realized using $\text{Ca}_3\text{Co}_4\text{O}_9$. Cu-tape was used to connect the thermoelectric materials. The increased leg density obtained without risking electric short-circuit conditions (the applied substrate, in this case mineral-fiber band, is the electric isolating layer) is the advantage of coiled TEGs compared with conventional rigid TEGs that have a “chess pattern” geometry. Indeed, flexible TEG constructed with thin-film deposited materials can be compacted to a very high degree. The presented prototype is a macroscopic system that can also be developed at smaller scales.

Experimental

Material Syntheses and Preparation

The p-type thermoelectric oxide $\text{Ca}_3\text{Co}_4\text{O}_9$ was synthesized using the sol-gel method, as described by Feldhoff et al. (2008). Nitrates of calcium and cobalt cations were stoichiometrically added to an aqueous ammonia solution of pH = 9 containing citric acid and EDTA for complexing the solvated metal ions. The obtained precipitate was calcined at 1,073 K for 10 h with a heating and cooling rates of $3\text{K} \cdot \text{min}^{-1}$. The calcined powder product was cold-pressed and sintered at 1,173 K for 10 h at heating and cooling rates of $2\text{K} \cdot \text{min}^{-1}$. Bars (legs) with length, width and thickness of 6 mm, 1.5 mm and 1 mm, respectively, were cut from the obtained $\text{Ca}_3\text{Co}_4\text{O}_9$ ceramic-disc.

The Cu-Ni alloy was in the form of a commercially available wire with a diameter of 1 mm. To connect the thermoelectric materials, adhesive Cu-tape was attached on a mineral-fiber band (HORST GmbH; order-nr.: 10 03 02). The thermoelectric materials were mounted to the Cu connectors and attached by a commonly used solder, to obtain the electric series connection, that is essential for the device. Silver paste was used to connect the thermoelectric materials with the Cu connectors through the solder. Silver paste is used to avoid other preparation technologies such as physical vapor deposition (PVD) when coating the ceramic surface

with a metallic layer. It is not possible to use the silver paste without soldering, because this leads to the delamination of the silver layer from the Cu surface during heating due to the thermomechanical stresses inside the assembled layer structure. The manufacturer's physical data for applied commercial materials are listed in Table 1. The parameters for the Cu tape were taken from the data sheet prepared by Deutsches Kupfer-Institut e.V. (DKI), see Franke and Juhl (2000). The entropy conductivity at open-circuit conditions Λ is related to the heat conductivity λ via the absolute working temperature T , shown in eq. [6], see Feldhoff (2015).

$$\lambda = T \cdot \Lambda \quad (6)$$

Thermoelectric Measurements of Single Materials

To characterize the thermoelectric properties of the materials, the temperature-dependent isothermal specific electric resistivity and the Seebeck coefficient, as estimated from the thermovoltage, were measured. Using these data the

power factor $\frac{\alpha^2}{\rho}$, which is a part of the tensor element, describing the entropy conductivity coupled to the electric phenomenon, in eq. [1], was estimated for each compound. A precision vertical diamond wire-saw model 3242 from O'WELL was used for sample preparation. Thermoelectric properties were measured using a measurement cell constructed in-house that is a modified version of the arrangement described by Indris (2001). The sample is clamped between two platinum electrodes to close the electric circuit in a pseudo-four-point measurement. The applied furnace is an ELITHE thermal system. The electronic parameters were measured with KEITHLEY 2100 6 $\frac{1}{2}$ Digit Multimeters. The measured data were converted using the LAB VIEW software. An illustration of the measurement setup for determining the parameters of single materials is presented in Figure 1.

Thermoelectric Measurements of Prototype TEG

The fabricated prototype was placed on a heater to estimate its thermoelectric characteristics. The heat sink was

Table 1: Physical manufacturer's data of applied commercial materials with thermoelectric parameters for 293 K.

material	$\rho/m\Omega\text{cm}$	$\lambda/W(\text{mK})^{-1}$	$\Lambda/W\text{m}^{-1}\text{K}^{-2}$	$\alpha/\mu\text{VK}^{-1}$	$T_{\text{degradation}}/\text{K}$
mineral fiber	$10^{17} \dots 10^{18}$	1.0	$3.4 \cdot 10^{-2}$	n.a.	890 (T_{strain})
Cu tape	$1.7 \cdot 10^{-3}$	394	1.3	n.a.	1,356 (T_{melt})
Cu-Ni alloy	$4.9 \cdot 10^{-2}$	23	$7.8 \cdot 10^{-2}$	-40	1,553 (T_{melt})
Sn-Pb solder	$1.4 \cdot 10^{-2}$	50	$1.7 \cdot 10^{-1}$	n.a.	456 (T_{melt})

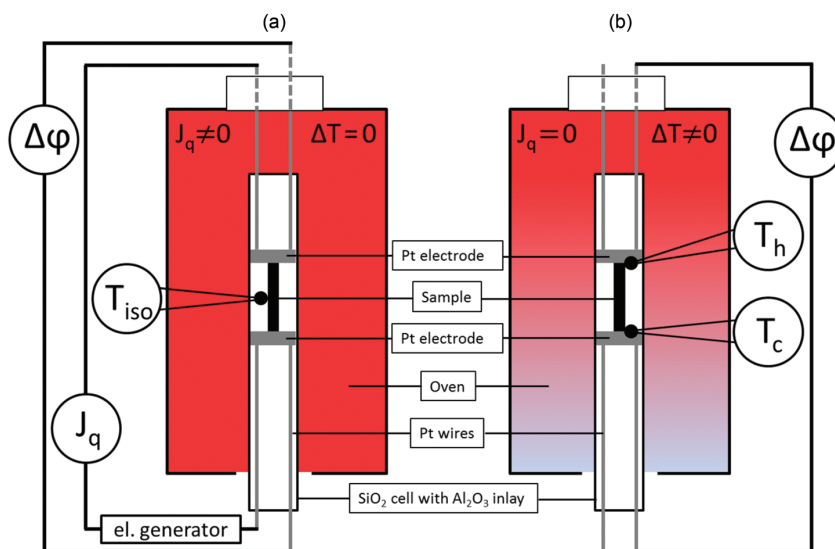


Figure 1: Schematic illustration of the measurement setup for determining the thermoelectric characteristics of single materials. (a) setup for determining the specific isothermal electric resistance, (b) setup for determining the Seebeck coefficient.

established naturally, using the temperature drop, that was generated by radiation losses without any additional setup for passive or active cooling. Hence, the temperature of the cold junction of the device increased with the increasing temperature of the hot side (heater side). The used heat-source was a STUART CB160 hot-plate. The prototype TEG was placed on the heater in a bent form as shown in Figure 3(c). A schematic illustration of the measurement setup is shown in Figure 2. The temperature was measured using thermocouples. The thermovoltage $U = \Delta\varphi$ (see eq. [5]) and the electric current $I = J_q$ (see eq. [3]) were measured for different external load R_{load} -values.

Microstructure Analysis

The materials were analyzed using field-emission scanning electron microscopy (FE-SEM) using a JEOL JSM-6700F, equipped with an Oxford Instruments INCA 300 energy-dispersive X-ray spectrometer (EDXS) for elemental analysis. The phase composition of $\text{Ca}_3\text{Co}_4\text{O}_9$ calcined powder product and sintered ceramic were analyzed by X-ray diffraction (XRD) using a Bruker D8 Advance with $\text{Cu-K}\alpha$ radiation. The reference data for the crystal structure analysis were taken from the Powder Diffraction File (PDF2) database.

Fabrication of the Flexible Thermoelectric Generator

Figure 3 shows the fabricated device as a flat stripe and in perspective view to show the provided flexibility. The basic material of the developed generator is a mineral-

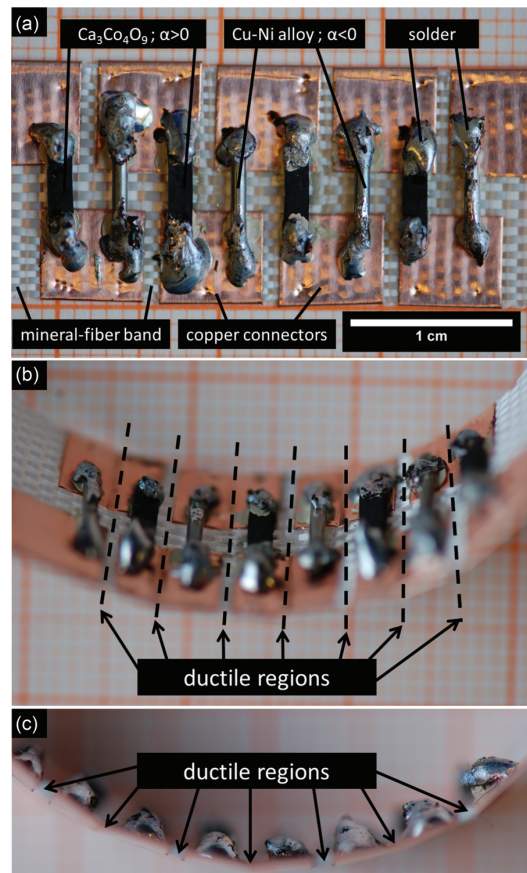


Figure 3: Microphotography of the prototype flexible TEG; (a) side view on plan side, (b) perspective view on bend device, (c) top view on bend device.

fiber band that provides a flexible substrate for the TEG stripe. The band is 14.5 mm wide and 150 μm thick and can be heated to 890 K in continuous working conditions.

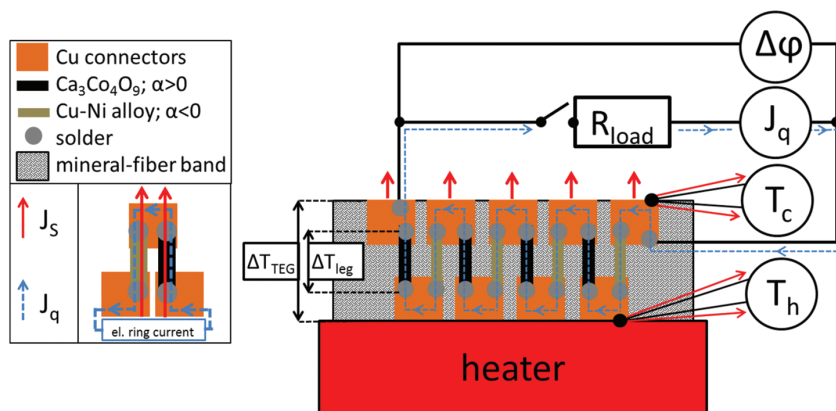


Figure 2: Schematic side-view illustration of the measurement setup for determining the thermoelectric characteristics of the flexible TEG. Schematics for a device with parallel entropy current J_s (see eq. [2]) and electric ring current J_q (see eq. [3]) are displayed.

The copper tape, used to realize the electric series connection, has a width of 6.3 mm and a thickness of 50 μm . It was attached with its adhesive side to the mineral-fiber band substrate by clamping it around the edge of the band such that there was approximately 1 mm of free space between each pair of Cu stripes. The gap between the connectors of the two sides (hot and cold sides in working conditions) is approximately 2.5 mm. The $\text{Ca}_3\text{Co}_4\text{O}_9$ ceramic legs were cut from a sintered disc of the $\text{Ca}_3\text{Co}_4\text{O}_9$ material. Each p-type leg exhibits a length of 6 mm, a width of 1.5 mm and a thickness of 1 mm. The metallic Cu-Ni alloy was used in the form of a wire with a diameter of 1 mm. The wire was also cut into pieces with a length of 6 mm. To fix the thermoelectric legs to the copper connectors, the materials were initially coated with silver paste that had been cured at room temperature. The legs were then soldered to obtain a mechanically stable connection.

To examine the inside of the fabricated device, a basic unit was cut out and embedded in epoxy resin to fix the thin and flexible part of the device. A cross-section was then obtained by cutting and polishing the assembled materials. A photograph of the cross-section of the prepared basic unit is shown in Figure 4. With the exception the silver paste all components of the prepared basic unit of the prototype flexible TEG can be

seen. Related to the prepared cut, the Cu-Ni alloy wire is completely surrounded by the used solder (right side of the basic unit). The ceramic $\text{Ca}_3\text{Co}_4\text{O}_9$ material is not completely surrounded by the solder (left side of the basic unit). Due to the location of the prepared cut for the cross-section, only one piece of the solder remains, that is positioned on the upper left edge of the $\text{Ca}_3\text{Co}_4\text{O}_9$ sample bar. Despite of the impression conveyed by the arrangement shown in Figure 4, all connecting regions of thermoelectric materials and the Cu connectors were coated completely with solder and provided a mechanically stable fixation, see Figure 3. Figure 4(b), 4(c) show pseudocolor micrographs with the displayed colors related to the energy-ranges are displayed to identify the materials used in the basic unit arrangement. The epoxy resin, surrounding the basic unit, is displayed in orange-red as caused by the X-ray emission of the carbon (C: K-emission) with an emission energy in the 0–0.5 keV range. The electric connectors (Cu: L-emission) and the Cu-Ni alloy (Cu, Ni: L-emission) are shown in yellow with an X-ray energy range of 0.5–1.0 keV. The mineral-fiber band (Si, Al: K-emission) is colored green and is related to an energy range of 1.0–2.0 keV. The solder (Sn, Pb: L, M-emission) and the silver paste (Ag: L-emission) are displayed in light blue with related X-ray emissions covering the 1.5–5 keV energy range.

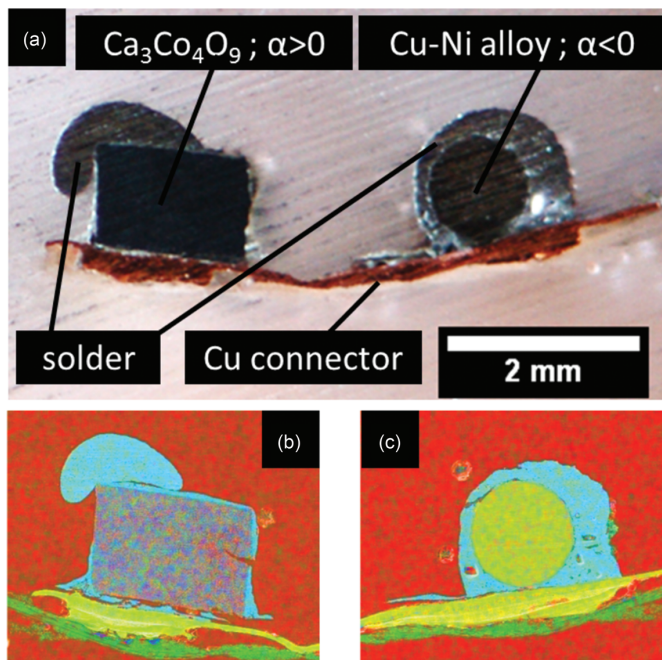


Figure 4: (a) Microphotograph of cut and polished cross-section of the prepared basic unit surrounded by epoxy resin (mineral-fiber band is not visible); (b) pseudocolor micrograph of $\text{Ca}_3\text{Co}_4\text{O}_9$ side; (c) pseudocolor micrograph of Cu-Ni alloy side. Light blue: Sn, Pb, Ca and Ag (solder and Ag-paste); green: Si, Ca and Al (mineral-fiber band); yellow: Cu and Ni (electric connector and Cu-Ni alloy); purple: Co and Ca (p-type semiconductor); orange-red: C (epoxy resin).

3.3 An Approach to a Flexible Thermoelectric Generator Fabricated using Bulk Materials 65

For the ceramic material $\text{Ca}_3\text{Co}_4\text{O}_9$, the mixture of pseudocolors results in purple color (Ca, Co: L, K-emission). The additional energy ranges are for Ca (orange-red) with an energy range of 0–0.5 keV and for Co (blue) with an energy range of 6.0–9.0 keV.

Figure 5 shows the area-related elemental distributions of the cut and polished cross-section of the prepared basic unit. The detailed results for elemental distribution of each element are presented.

The interface of the ceramic $\text{Ca}_3\text{Co}_4\text{O}_9$ and the metallic solder, interconnected with the silver paste, is the most fragile part of the device. Although the connection of the Cu-Ni alloy and the copper connector, realized by silver paste and solder, is still intact after the preparation, the ceramic $\text{Ca}_3\text{Co}_4\text{O}_9$ is delaminated from the copper tape. The difference in physical surface properties of ceramic material and metallic components leads to the poor mechanical stability of the hetero-material boundary region. The disconnection can

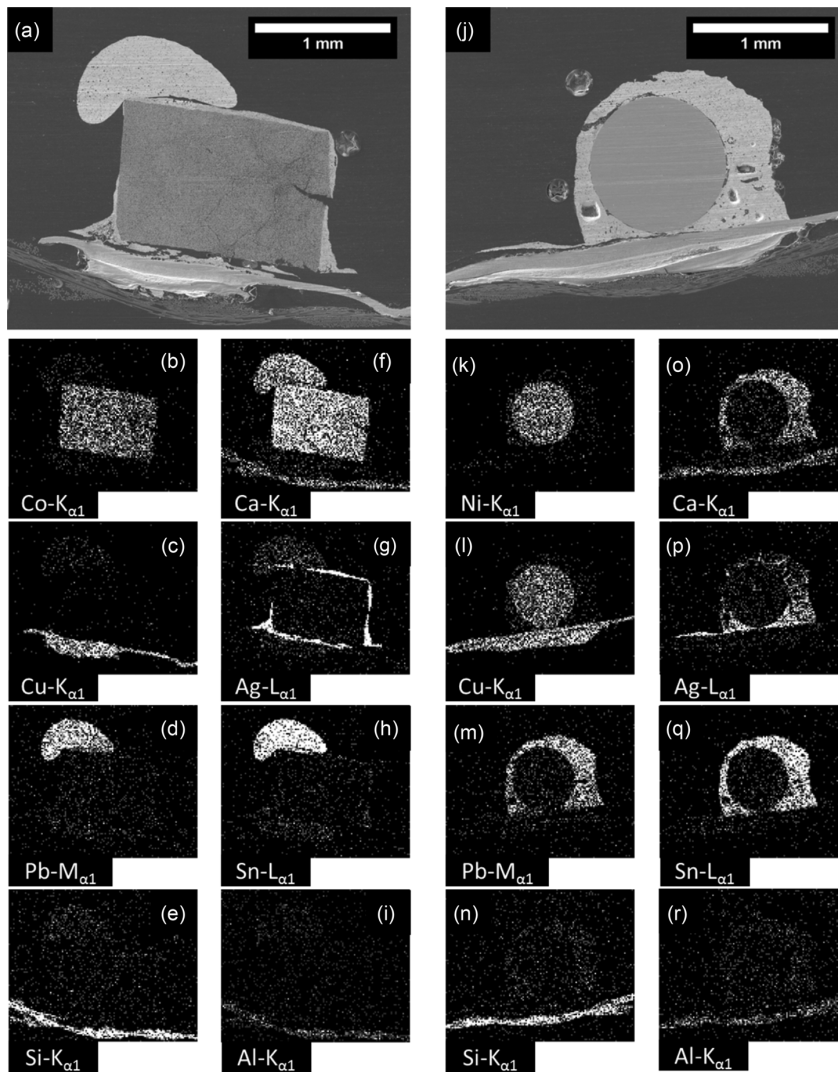


Figure 5: EDXS elemental maps of cut and polished cross-section of the prepared basic unit: (a) Secondary electron micrograph of the $\text{Ca}_3\text{Co}_4\text{O}_9$ side, (b)–(i) elemental distribution at the $\text{Ca}_3\text{Co}_4\text{O}_9$ side; (j) Secondary electron micrograph of the Cu-Ni alloy side; (k)–(r) elemental distribution at the Cu-Ni alloy side.

be caused by the mechanical preparation and heating of the device until the melting point of the solder.

Results and Discussion

Microstructure of Materials and Compositions

The crystal structures of the calcined powder product and the sintered p-type $\text{Ca}_3\text{Co}_4\text{O}_9$ ceramic were analyzed by X-ray diffraction. The diffractograms are shown in Figure 6. Neither $\text{Ca}_3\text{Co}_4\text{O}_9$ calcined powder nor the sintered ceramic show any phases other $\text{Ca}_3\text{Co}_4\text{O}_9$. The relative intensities of the detected reflections change from calcined powder to sintered oxide ceramic such that only 001 and 201 reflections remain. This indicates a texture where plate-like grains are lying preferentially with their crystallographic c-axis normal to the surface of the sintered ceramic, as shown in Figure 8. Such a textured surface structure is caused by the cold pressing during the preparation for the sintering process. The Bragg positions in Figure 6 were taken from the Powder Diffraction Files (PDF2) database.

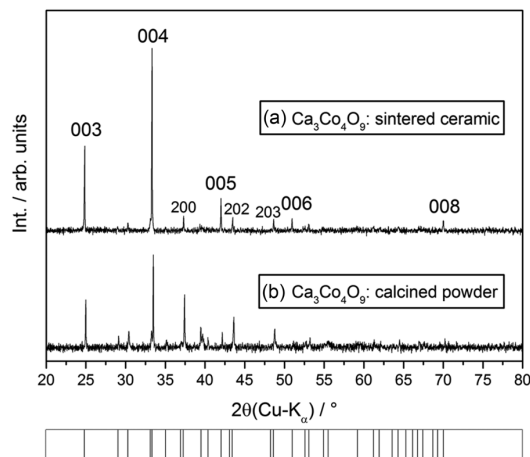


Figure 6: XRD analysis of semi-conducting $\text{Ca}_3\text{Co}_4\text{O}_9$ with displayed Bragg positions underneath (PDF number: 00-058-0661); (a) powder product calcined at 1,073 K for 10 h; (b) textured surface of the ceramic sintered at 1,173 K for 10 h.

Figure 7 shows the elemental compositions of the thermoelectric $\text{Ca}_3\text{Co}_4\text{O}_9$ ceramic and Cu-Ni alloy materials by EDXS method in the FE-SEM. The quantitative analysis of the metals inside the Cu-Ni alloy, Figure 7(b), reveals Cu, Ni

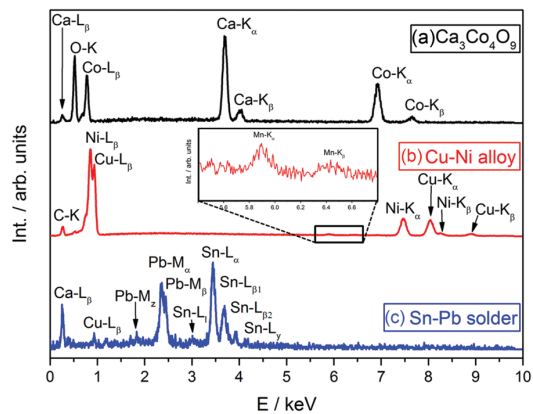


Figure 7: EDX spectra of synthesized and prepared materials. (a) sintered $\text{Ca}_3\text{Co}_4\text{O}_9$ ceramic, (b) Cu-Ni alloy with magnified view of Mn- $K_{\alpha,\beta}$ signals, (c) applied Sn-Pb based solder.

and Mn fractions of 57.89 wt.%, 41.11 wt.% and 1.00 wt.%, respectively. Cu-Ni alloys of this elemental composition typically exhibits an almost constant electric resistivity over a wide temperature range (Constantan, Isotan); this is confirmed by an inspection of Figure 10; see Lide (2008). Figure 8 shows a secondary electron micrograph of the surface microstructure for the semiconducting p-type $\text{Ca}_3\text{Co}_4\text{O}_9$. Due to the oriented crystal growth during the sintering process, the grains at the outermost surface of the sintered ceramic show a plate-like morphology. The surface structure exhibits a median grain width of $2.5\ \mu\text{m}$ and a median thickness of the crystal plates of $1.3\ \mu\text{m}$. The ceramic is not sintered to a dense body. The porous arrangement inside the ceramic can be expected to provide a low thermal conductivity; see Rhee (1975).

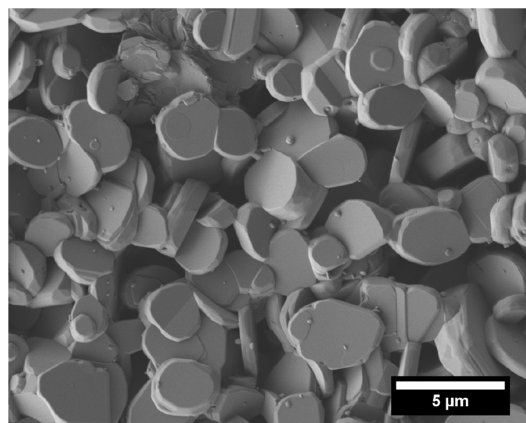


Figure 8: Secondary electron micrograph of the textured $\text{Ca}_3\text{Co}_4\text{O}_9$ surface (see Figure 6 for XRD analysis) after sintering at 1,173 K for 10 h. Note the different magnification compared with Figure 5.

Thermoelectric Investigations

The experimental errors for measurements of the Seebeck coefficients and for the isothermal specific electric resistivities were estimated by considering the errors for sample's geometry measurements, fluctuations of electrical quantities and fluctuations in the temperature profile for the measurement of each material. Based on these considerations, we developed a reliability range for each measurement. Figure 9 shows the obtained Seebeck coefficients of the $\text{Ca}_3\text{Co}_4\text{O}_9$ ceramic and the Cu-Ni alloy.

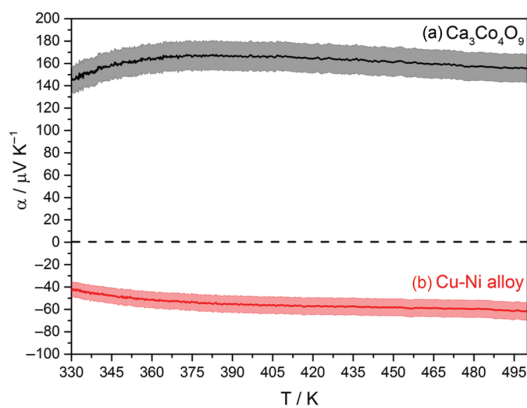


Figure 9: Measured Seebeck coefficients of applied thermoelectric materials as a function of temperature with estimated error ranges. (a) $\text{Ca}_3\text{Co}_4\text{O}_9$ ceramic; (b) Cu-Ni alloy.

The Seebeck coefficients of analyzed materials depend only weakly on temperature. The absolute value of the semiconducting oxide Seebeck coefficient is nearly three times higher than that of the used metallic thermoelectric material. The Seebeck coefficients decreased sharply at approximately room temperature (300 K) due to the vanishing temperature difference along the samples that (not shown). We therefore decided to display the values starting at 330 K and to show the values in the range for which we have reliable measurement data. The Seebeck coefficient of the ceramic material is almost three times higher than the value for the Cu-Ni alloy. The Seebeck coefficient of the Cu-Ni alloy reaches values in the range between -40 and $-60 \mu\text{V K}^{-1}$ at room temperature (300 K). This result is in good agreement with the values obtained in round-robin measurements reported by Lu et al. (2009) Lu, Lowhorn, Wong-Ng, Zhang, Lu, Otani, Thomas, Tran, Dilly, Ghamaty, Elsner, Hogan, Downey, Jie, Li, Obara, Sharp, Caylor, Venkatasubramanian, Willigan, Yang, Martin, Nolas, Edwards, and Tritt and Lowhorn et al. (2009) Lowhorn, Wong-Ng, Zhang, Lu, Otani, Thomas, Tran, Dilly, Ghamaty, Elsner, Hogan, Downey, Jie, Li, Obara, Sharp,

Caylor, Venkatasubramanian, Willigan, Yang, Martin, Nolas, Edwards, and Tritt. For the Seebeck measurements of the $\text{Ca}_3\text{Co}_4\text{O}_9$, the values are $10\text{--}20 \mu\text{V K}^{-1}$ higher than those obtained at 300 K by Miyzaki (2004).

Figure 10 shows the results for isothermal specific electric resistivity ρ measurements of applied thermoelectric materials as a function of temperature. The isothermal specific resistivities of ceramic $\text{Ca}_3\text{Co}_4\text{O}_9$ are in the expected range for this semiconducting oxides. The measurement results are on the same order of magnitude as those presented in Miyzaki (2004). The absolute values are 3 to 4 times higher. For the Cu-Ni alloy, the isothermal specific resistivity is almost independent of the temperature in the considered temperature range. This was already expected from elemental analyses (see discussion of Figure 7(b)). The isothermal specific resistivity values of the Cu-Ni alloy match those reported in the manufacturer's datasheet.

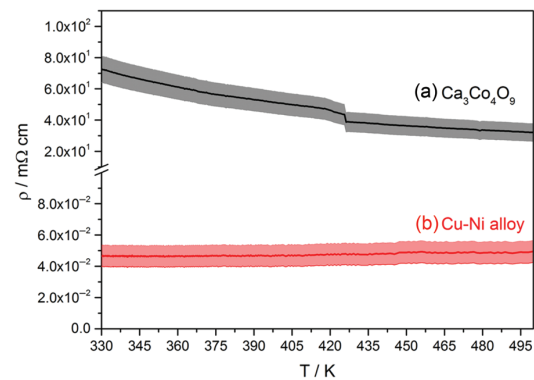


Figure 10: Measured isothermal specific electric resistivities of applied thermoelectric materials as function of temperature with estimated error ranges. (a) $\text{Ca}_3\text{Co}_4\text{O}_9$ ceramic; (b) Cu-Ni alloy.

The power factors $\frac{\alpha^2}{\rho}$ for both materials were calculated from the median values of measured electric resistances and Seebeck coefficient data and are displayed in Figure 11. The error range was received by error propagation from determined errors for the single parameters of the Seebeck coefficients α (see Figure 9) and the specific resistivities (see Figure 10).

To determine the thermoelectric parameters of the flexible prototype TEG, four temperature differences ΔT were established, as indicated in Table 2 and Figure 12. Figure 12(a) shows voltage-current (U-I) characteristics with a good agreement between the measured data (data points) and the linear fit (solid lines). Note, that the slopes of the lines correspond to the internal resistance R_{TEG} , as indicated in

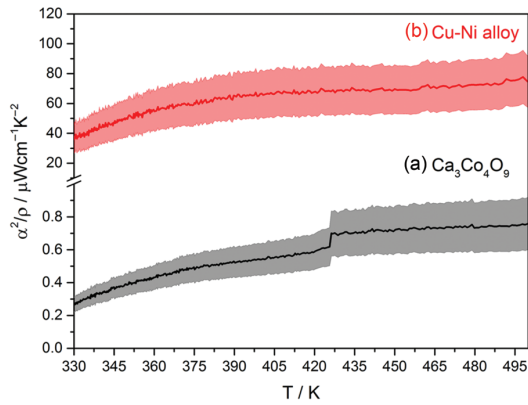


Figure 11: Power factors estimated from measured isothermal specific electric resistivities and Seebeck coefficients as function of temperature with estimated error ranges obtained from error propagation related to errors shown in Figures 9 and 10. (a) $\text{Ca}_3\text{Co}_4\text{O}_9$ ceramic; (b) Cu-Ni alloy.

Table 2: Determined thermoelectric parameters of the prototype flexible TEG for different temperature conditions.

T_h/K	$\Delta T_{\text{TEG}}/\text{K}$	$T_{\text{median}}/\text{K}$	R_{TEG}/Ω	$P_{\text{el, max}}/\text{nW}$	U_{oc}/mV	$I_{\text{sc}}/\mu\text{A}$
420	31	404	851.61	82.00	16.52	19.40
361	22	350	909.91	14.56	7.29	8.01
336	16	328	885.94	4.65	4.06	4.58
307	7	304	715.90	0.24	0.88	1.23

Table 2. The electric output power P_{el} was estimated in terms of different load resistivities R_{load} . Figure 12(b) also shows the electric output power-electric current ($P_{\text{el}}-I$) characteristics, with good agreement observed between the measured data (data points) and the parabolic fit (solid lines).

The values of the open circuit voltage U_{oc} calculated from the measured Seebeck coefficients α (see Figure 9) of single materials, are considerably larger. This is likely due to large differences between the temperature drop of the entire device from the heat source to heat sink ΔT_{TEG} and the established temperature difference along the legs of a basic unit $\Delta T_{\text{basicunit}} = \Delta T_{\text{leg}}$ (see Figure 2). Table 3 presents the calculated temperature differences along the legs of a basic unit $\Delta T_{\text{basicunit}}$ related to the measured Seebeck coefficients (see Figure 9) and open circuit voltages for the basic unit $U_{\text{oc, basicunit}}$. The data collected for the hot side temperature of $T_h = 336\text{K}$ and the temperature difference along the entire TEG, $\Delta T_{\text{TEG}} = 7\text{K}$, were not considered, because the measured values for the Seebeck coefficients for the single materials in this temperature range are not reliable (see Figure 9 and related discussion).

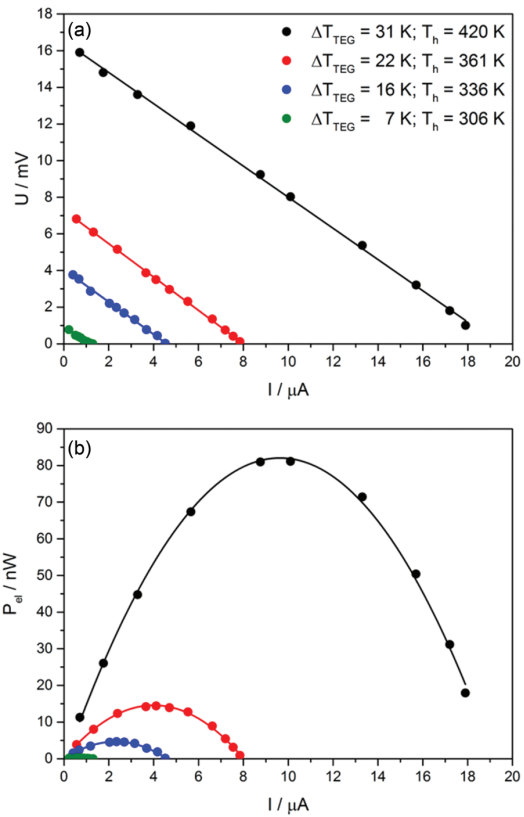


Figure 12: Thermoelectric properties of the prototype flexible TEG (four basic units, see Figure 3 for length of the device). (a) Voltage over electric current for four different temperature conditions. (b) Power-current characteristics for four different temperature conditions.

Table 3: Calculated and measured temperature distributions inside the device.

T_h/K	$\Delta T_{\text{TEG}}/\text{K}$	$\Delta T_{\text{basicunit}}/\text{K}$	$\alpha_{\text{basicunit}}/\mu\text{VK}^{-1}$	$U_{\text{oc, basicunit}}/\text{mV}$	$\frac{\Delta T_{\text{basicunit}}}{\Delta T_{\text{TEG}}}/\%$
420	31	19	222.25	4.13	61.29
361	22	9	211.06	1.82	40.91
336	16	6	182.13	1.02	37.50

Large parasitic heat losses are present along the device's hot and cold sides and are likely caused by the mineral-fiber substrate. The contact area between the copper-tape and the mineral-fiber band appears to be too large. The mineral-fiber band has to be more slim such that the amount of integrated copper can be reduced to minimize this contact areas. The thermal short-circuited situation can also be caused by the Cu-Ni alloy, which exhibits a larger thermal conductivity compared with the fiber

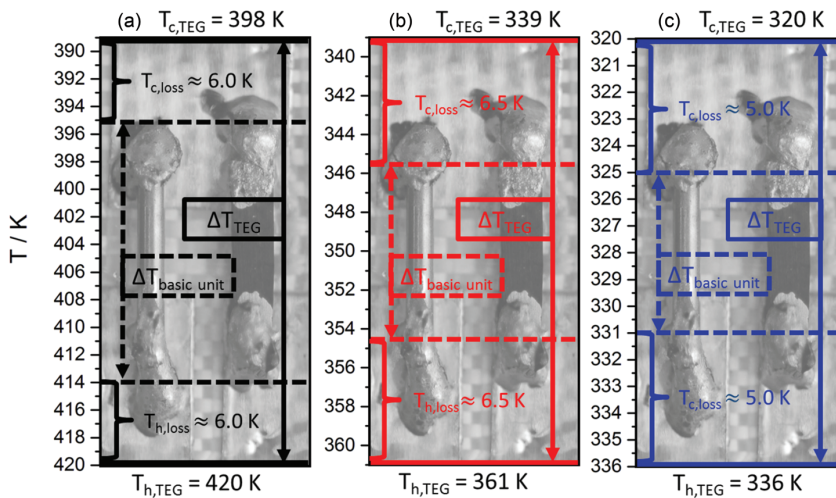


Figure 13: Temperature distributions inside the TEG with displayed thermal losses for hot side $T_{h,loss}$ and cold side $T_{c,loss}$ of the entire TEG.

substrate (see Table 1). The alloy must be the main origin of the parasitic heat losses via thermal short circuiting. Figure 13 illustrates the temperature distributions across the hot and cold sides of the device relative to the hot side temperature.

Conclusions

The prototype TEG displays flexibility that is only limited by the applied pieces of ductile copper-tape as electric connectors. The limiting factor for the heating of the device is the solder, which melts between 423 and 473 K. Because of the less heat proofed Sn-Pb solder the prototype can not be applied to temperatures above the decomposition temperature of BiTe. Related to the other materials in the device a reasonable temperature range for application should be up to 890 K (degeneration temperature of the mineral-fiber band). The solder also limits the current because of a very high boundary resistivity at the connecting regions of metallic solder and semiconducting p-type oxide. The geometrical arrangement of the applied materials provides variation of thermoelectric materials while maintaining the mechanical flexibility of the TEG. Metals and alloys as well as ceramics can be integrated in the fabrication process. The joining of dissimilar materials is the major concern. It is therefore important to investigate alternatives to soldering for attaching non-metallic materials to metallic connectors. It is also important to investigate the use of a

solder with a higher melting point, such as a Sn-Sb solder, to improve the thermal stability of the entire device. To join ceramic materials to metallic connectors, alternative solutions must be applied to avoid preparation techniques such as physical vapor deposition (PVD). Epoxy resin including metal particles for electric conduction should be tested.

The observed parasitic heat losses are likely caused by the large area of the copper-tape that can transport the heat to the mineral-fiber substrate. The substrate material should be thinner in order to decrease the thermal conduction. To decrease the thermal losses, the width of the substrate material must be smaller to minimize the gap between the hot side of the generator and the hot side of the thermoelectric junctions related to the thermoelectric legs.

Here a symmetric approach to fabrication was used. The legs were centered between the hot and the cold sides of the entire device. This architecture leads to disadvantages for temperature distributions during working conditions. Instead, an asymmetric architecture, in which the legs are placed as near as possible to the hot side using a smaller Cu connector while the Cu connector of the cold side should exhibit a larger area to act as passive cooling system. It is expected that constructing the flexible TEG stripe in such an asymmetric fashion would reduce the parasitic heat losses from the heat source to the hot junction of the thermoelectric materials. For the short piece of the presented prototype it is indeed nearly impossible to integrate an effective heat exchanger. For an upscaled and coiled up version of the prototype it is

expected, that the mechanical stability suffice to place a cooler onto the device. Another imaginable possibility to integrate heat exchanger are miniaturized heat-pipes that are clamped to the electric connectors of each basic unit. For application a thermoelectric energy harvesting device a heat exchanger is considered to be essential.

References

- Cao, Z., E. Koukharenko, R. Torah, J. Tudor, and S. Beeby. 2014. "Flexible Screen Printed Thick Film Thermoelectric Generator with Reduced Material Resistivity." *PowerMEMS 557* (012016):1–5. Conference Series.
- Feldhoff, A. 2015. "Thermoelectric Material Tensor Derived From the Onsager – De Groot – Callen Model." *Energy Harvesting and Systems 2* (1):5–13.
- Feldhoff, A., M. Arnold, J. Martynczuk, T. Gesing, and H. Wang. 2008. "The Sol-Gel Synthesis of Perovskites by EDTA/Citrite Complexing Method Involves Nanoscale Solid State Reactions." *Solid State Sciences 10*:689–701.
- Feldhoff, A., and B. Geppert. 2014. "A High-Temperature Thermoelectric Generator based on Oxides." *Energy Harvesting and Systems 1* (1–2):69–78.
- Francioso, L., C. D. Pascali, I. Farella, C. Martucci, C. Creti, P. Siciliano, and A. Perrone. 2011. "Flexible Thermoelectric Generator for Ambient Assisted Living Wearable Biometric Sensors." *Journal of Power Sources 196*:3239–43.
- Franke, H., and K. Juhl. 2000. *Kupfer in Der Elektrotechnik-Kabel Und Leitungen*. Duesseldorf, DE: Breuerdruck. Internet Version 2000.
- Fuchs, H. 2010. *The Dynamics of Heat – a Unified Approach to Thermodynamics and Heat Transfer*, 2nd edn. New York: Springer. Graduate Texts in Physics.
- Fuchs, H. 2014. "A Direct Entropic Approach to Uniform and Spatially Continuous Dynamical Models of Thermoelectric Devices." *Energy Harvesting and Systems 1* (3–4):253–65.
- Geppert, B., D. Groeneveld, V. Loboda, A. Korotkov, and A. Feldhoff. 2015. "Finite-Element Simulations of a Thermoelectric Generator and Their Experimental Validation." *Energy Harvesting and Systems 2* (1):95–104.
- Glatz, W., S. Munwyler, and C. Hierold. 2006. "Optimisation and Fabrication of Thick Flexible Polymer Based Micro Thermoelectric Generator." *Sensors and Actuators, A 132*:337–45.
- Indris, S. 2001. *Perkolaton Von Grenzflächen in Nanokristallinen Keramischen Kompositen – Li-Ionenleitfähigkeit Und Li-NMR-Relaxation*. Göttingen, DE: Cuvillier Verlag. Dissertation.
- Kuznetsov, V. L., L. A. Kuznetsova, A. E. Kaliazin, and D. M. Rowe. 2002. "High Performance Functionally Graded and Segmented-based Materials for Thermoelectric Power Generation." *Journal of Materials Science 37*:2893–7.
- LeBlanc, S., S. K. Yee, M. L. Scullin, C. Dames, and K. E. Goodson. 2014. "Material and Manufacturing Cost Considerations for Thermoelectrics." *Renewable and Sustainable Energy Reviews 32*:313–27.
- Lide, D. 2008. *CRC Handbook of Chemistry and Physics*, 89th edn. Boca Raton, FL: CRC Press. Internet Version 2009.
- Lowhorn, N. D., W. Wong-Ng, W. Zhang, Z. Q. Lu, M. Otani, E. Thomas, M. G. T. N. Tran, N. Dilly, S. Ghamaty, N. Elsner, et al. 2009. "Round-Robin Measurements of Two Candidate Materials for a Seebeck Coefficient Standard Reference Material." *Applied Physics A 94*:231–4.
- Lu, Z. Q. J., N. D. Lowhorn, W. Wong-Ng, W. Zhang, Z. Q. Lu, M. Otani, E. Thomas, M. G. T. N. Tran, N. Dilly, S. Ghamaty, et al. 2009. "Statistical Analysis of a Round-Robin Measurement Survey of Two Candidate Materials for a Seebeck Coefficient Standard Reference Material." *Journal of Research of the National Institute of Standards and Technology 114*:37–55.
- Miyzaki, Y. 2004. "Crystal Structure and Thermoelectric Properties of the Misfit-Layered Cobalt Oxides." *Solid State Ionics 117*:463–7.
- Poudel, B., Q. Hao, Y. Ma, Y. Lan, A. Minnich, B. Yu, X. Yan, D. Wang, A. Muto, D. Vashaee, et al. 2008. "High-Thermoelectric Performance of Nanostructured Bismuth Antimony Telluride Bulk Alloys." *Science 320*:634–8.
- Rhee, S. 1975. "Porosity-Thermal Conductivity Correlation for Ceramic Materials." *Materials Science and Engineering 20*:89–93.
- Stepien, L., A. Roch, S. Schlaier, I. Dani, A. Kiri, F. Simon, M. v. Lukowicz, and C. Leyens. 2015. "Investigation of the Thermoelectric Power Factor of KOH Treated PEDOT:PSS Dispersions for Printing Applications." *Energy Harvesting and Systems 2*:1–11.
- Suemori, K., S. Hoshino, and T. Kamata. 2013. "Flexible and Lightweight Thermoelectric Generators Composed of Carbon Nanotube-Polystyrene Composites Printed on Film Substrate." *Applied Physics Letter 103* (153902):1–4.
- Yoo, B. Y., C.-K. Huang, J. R. Lim, J. Herman, M. A. Rayn, J.-P. Fleurial, and N. V. Myung. 2005. "Electrochemically Deposited Thermoelectric n-Type Thin Films." *Electrochimica Acta 50*:4371–7.

3.4 Finite-Element Simulations of a Thermoelectric Generator and Their Experimental Validation

Benjamin Geppert, Dennis Groeneveld, Vera Loboda,

Alexander Korotkov and Armin Feldhoff

Energy Harvesting and Systems, 2(1), 95-104, (2015)

Special Double Issue Article

B. Geppert*, D. Groeneveld, V. Loboda, A. Korotkov and A. Feldhoff

Finite-Element Simulations of a Thermoelectric Generator and Their Experimental Validation

Abstract: A versatile finite-element simulation tool was developed to predict the electric power output, the distributions of the electric and entropy potentials (i.e., the absolute temperature) and the local flux densities of electric charge and thermal energy (i.e., heat) for a thermoelectric generator. The input parameters are the thermogenerator architecture (i.e., geometries of different components and number of legs) and material properties such as specific electric conductivity, Seebeck coefficient and thermal conductivity. The finite-element simulation tool was validated by modeling a commercially available thermoelectric generator, which was based on semiconducting n- and p-type $\text{Bi}_{2-x}\text{Sb}_x\text{Te}_3$ with ceramic cover plates, and comparing the modeled voltage–current characteristics and power characteristics with experimental values for different temperature conditions. The geometric parameters could easily be determined from photomicrography and cross-sectional scanning electron microscopy observations. The electric conductivity and Seebeck coefficient were measured, as functions of temperature, from the integer module as leg-averaged values. The thermal conductivity was taken from literature data, which required estimating the compositions of components using energy-dispersive X-ray spectroscopy in the scanning electron microscope and their crystal structures using X-ray diffraction. Good agreement was found between the simulated and measured voltage–current and power–current characteristics. The finite-element simulation tool is versatile because it uses a script-based approach, which allows easy parameter changes and allows it to be adapted

to thermogenerators consisting of different geometries and materials, including novel materials.

Keywords: thermoelectric generator, thermal energy, electric energy, energy conversion, finite-element method

DOI 10.1515/ehs-2015-0001

Introduction

The development and application of thermoelectric materials, for example, for harvesting electrical power from waste heat sources, is a current field of study that requires interdisciplinary investigations. The implementation of newly developed thermoelectric materials into thermoelectric generators (TEGs) benefits from modeling the thermoelectric properties of the generators with respect to the individual properties of the employed materials. A TEG is a device that transfers energy from thermal (entropy) current to electric current; see Fuchs (2010, 2014), Feldhoff (2015). Following the concept of energy carriers as outlined by Falk, Herrmann, and Schmid (1983), it is quite intuitive to use the term *thermal energy* E, th when energy flows together with entropy S and to use the term *electric energy* E, el when energy flows together with electric charge q . The most straightforward description of a thermoelectric device relies on considering the flux densities of the aforementioned fluid-like quantities because it links them by the respective potentials, which are the absolute temperature T for entropy and the electric potential φ for electric charge. The energy flux densities are then as follows; see Fuchs (2014), Feldhoff and Geppert (2014b, 2014a), Feldhoff (2015):

$$\vec{j}_{E,th} = T \cdot \vec{j}_S \quad [1]$$

$$\vec{j}_{E,el} = \varphi \cdot \vec{j}_q \quad [2]$$

The flux densities of entropy \vec{j}_S and electric charge \vec{j}_q in a thermoelectric material, that is subjected to gradients of thermal potential $\vec{\nabla}T$ and electric potential $\vec{\nabla}\varphi$, can be easily obtained if a thermoelectric material tensor is considered; see Feldhoff (2015):

*Corresponding author: **B. Geppert**, Institute of Physical Chemistry and Electrochemistry, Leibniz Universität Hannover, Hannover, Lower Saxony, Germany, E-mail: benjamin-geppert@pci.uni-hannover.de

D. Groeneveld, Institute of Physical Chemistry and Electrochemistry, Leibniz Universität Hannover, Hannover, Lower Saxony, Germany, E-mail: dennis_groeneveld@ewetel.net

V. Loboda: E-mail: vera_loboda@mail.ru, **A. Korotkov:** E-mail: korotkov@rphf.spbstu.ru, Integrated Electronics Department, St. Petersburg Polytechnic University, St. Petersburg, Russia

A. Feldhoff, Institute of Physical Chemistry and Electrochemistry, Leibniz Universität Hannover, Hannover, Lower Saxony, Germany, E-mail: armin.feldhoff@pci.uni-hannover.de

$$\begin{pmatrix} \vec{j}_s \\ \vec{j}_q \end{pmatrix} = - \begin{pmatrix} \sigma \cdot \alpha^2 + \Lambda & \sigma \cdot \alpha \\ \sigma \cdot \alpha & \sigma \end{pmatrix} \cdot \begin{pmatrix} \vec{\nabla} T \\ \vec{\nabla} \varphi \end{pmatrix} \quad [3]$$

The thermoelectric tensor consists of three tensorial quantities; however, these quantities are treated as scalars. These are the specific electric conductivity σ under isothermal conditions (i.e., $\vec{\nabla} T = 0$, vanishing thermal potential gradient), the specific entropy conductivity Λ under electric open-circuited conditions (i.e., $\vec{j}_q = 0$, vanishing electric current), and the so-called Seebeck coefficient α , which is defined as *entropy flow per flow of unit charge*; see Fuchs (2014), Feldhoff and Geppert (2014b, 2014a), Feldhoff (2015).

In principle, electric charge is bound to some particle with chemical potential μ , and in the concept of combined potentials, see Fuchs (2014), the electrochemical potential $\tilde{\mu} = \mu + q \cdot \varphi$ is the more accurate quantity. However, because gradients are relevant, when the chemical potential μ has a weak temperature dependence, the electric potential φ can be used as a good approximation rather than the electrochemical potential $\tilde{\mu}$ as in eqs [2] and [3]; see Feldhoff (2015).

To construct the basic unit of a thermoelectric generator, two materials with different algebraic signs for the Seebeck coefficient α (*entropy flow per flow of unit charge*) must be thermally connected in parallel and electrically connected in series. For $\alpha > 0$, the motions of thermal and electrical fluxes are directed in the same way. In contrast, for $\alpha < 0$, the thermal and electrical fluxes are directed in opposite directions; see Feldhoff and Geppert (2014b), Feldhoff (2015). By additively connecting several of these basic units thermally in parallel and electrically in series, the electric potential φ can be increased over the device to provide an important electric energy flux density at device output according to eq. [2]; see Feldhoff (2015) for illustration. The choice of the thermoelectric materials that comprise the TEG depends on the conditions in which the energy conversion is to be performed.

Among the various thermoelectric materials, semiconductors exhibit the best thermoelectric performance because of their moderate charge carrier concentration, and they provide a good balance between specific electrical conductivity σ and the Seebeck coefficient α ; see Ioffe (1957). Consequently, semiconductors provide a high value of the so-called power factor $\sigma \cdot \alpha^2$, which is the charge-coupled entropy conductivity and occurs as part of the thermoelectric tensor in eq. [3]. To obtain a good TEG performance, the combination of n- and p-type semiconductors and a low-resistance electrical connection between them realized by metals or alloys is preferred. In commercially available generators, $\text{Bi}_{2-x}\text{Sb}_x\text{Te}_3$ -based materials are primarily used; see Kuznetsov et al. (2002), Poudel et

al. (2008). Additionally, the geometric properties of the materials that are combined to form the complete device have to be optimized for every system. Finite-element method (FEM) simulations are useful for calculating the thermoelectric performance in terms of the used materials and their geometric properties without constructing a real TEG. The thermoelectric properties can be measured over each individual material. Afterwards, the materials can be combined in a simulated TEG system with a specific geometry. Because the device does not have to be constructed, FEM simulations provide results ecologically, flexibly and rapidly. The objective of the present study is to demonstrate that FEM simulations are useful for predicting the thermoelectric properties of a TEG.

Experimental

Thermoelectric Measurement Setup

To estimate the thermoelectric characteristics of the TEG, it was placed between a heat source (heated copper plate) and a heat sink (water-cooled copper plate). The device was fixed with a clamping force of 0.6 kN, as indicated by a dynamometer. A schematic illustration of the measurement setup is shown in Figure 1. To provide good thermal surface contact, thermal grease with a specific thermal energy conductivity of $\lambda > 1.46\text{W}(\text{mK})^{-1}$ in the temperature range of ca. 300–550 K was used as the interface material. The temperature was monitored using thermocouples. The voltage $U = \Delta\varphi$ was measured as the drop of the electric potential on the external load R_{load} . Due to the low internal resistance R_{module} of the thermoelectric generator (see Table 4), the electric current I was estimated indirectly:

$$I = \frac{U}{R_{\text{load}}} \quad [4]$$

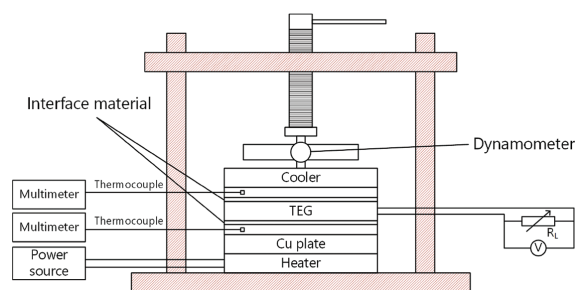


Figure 1: Schematic illustration of the measurement setup for determining the thermoelectric characteristics of the TEG with thermal grease as the interface material, after Hejtmanek et al. (2014).

The electric output power P_{el} was estimated according to:

$$P_{el} = \frac{U^2}{R_{load}} \quad [5]$$

Estimation of the Geometric and Thermoelectric Properties of the Thermoelectric Generator

A commercially available thermoelectric generator was purchased from Conrad Electronics SE (item number 193593-62, model number 1-7105). To construct the TEG in the model system, the geometry of the device, including the thermoelectric legs, the electric copper connectors and the alumina cover plates, were determined using the graphical tool ImageJ, which was applied to photomicrographs; see Schneider, Rasband, and Eliceiri (2012).

Figure 2 presents photographs of the TEG and of the device modeled based on the estimated geometry for each individual component.

The TEG includes $12^2 - 2 = 142$ legs. The space between each pair of legs is 1 mm. Table 1 lists the geometric properties of the TEG without considering the tin solder. The geometric properties were estimated by analyzing the photographs shown in Figure 2. The relevant parameters are the length L of each material parallel to the entropy flux and its cross-sectional area A . The filling factor of the module, i.e., the ratio of thermoelectric active to inactive areas, is equal to 32%. For the copper connectors and alumina cover plates, the values for the specific resistivity ρ and specific thermal energy (heat) conductivity λ were taken from the literature; see Lide (2008). For the thermoelectric $\text{Bi}_{2-x}\text{Sb}_x\text{Te}_3$ materials, the specific thermal energy (heat) conductivity λ was also taken from the literature; see Kim et al. (2012). The

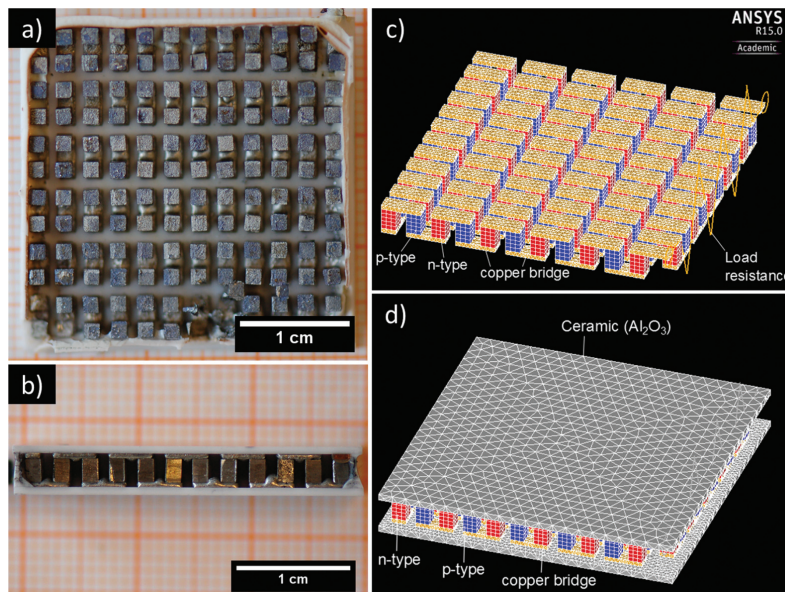


Figure 2: Photographs of the TEG for estimating the geometrical parameters and display of the modeled device; (a) inner top view of the TEG, (b) side view of the TEG, (c) modeled device with n- and p-type thermoelectric material and electric copper connectors, (d) modeled device with Al_2O_3 cover plates.

Table 1: Measured geometric properties of the TEG.

Component	Material	L/mm	A/mm^2	$\rho/\Omega\text{m}$	$\lambda/\text{W}(\text{mK})^{-1}$	$\Lambda/\text{Wm}^{-1}\text{K}^{-2}$
TE leg(n,p)	$\text{Bi}_{2-x}\text{Sb}_x\text{Te}_3$	2.05	1.96	see Table 4	1.05	$3 \cdot 10^{-3}$
Electric connector	Cu	0.44	5.32	$2.06 \cdot 10^{-8}$	401	1.15
Cover plates	Al_2O_3	0.64	870	$1 \cdot 10^{16}$	30.5	$8.71 \cdot 10^{-2}$

Notes: Length L of material and cross-sectional area A . The specific thermal energy resistivity ρ and specific thermal energy (heat) conductivity λ were taken from the literature as indicated in the text. The specific entropy conductivity λ was estimated according to eq. [6]. All data refer to a medial temperature of 350 K.

temperature-averaged values for the specific entropy conductivity Λ in Table 1 were calculated for a medial temperature of 350 K according to:

$$\lambda = T \cdot \Lambda \quad [6]$$

The specific electrical resistivity $\rho = \frac{1}{\sigma}$ of the thermoelectric material is the reciprocal of the specific electrical conductivity σ , and it was estimated under the temperature drops listed in Table 4. The systematic error, which results from the deviation from isothermal conditions (i.e. $\nabla T = 0$) according to requirements of eq. [3], however, is assumed to be small.

The Seebeck coefficient α was experimentally determined under electric open-circuited conditions (i.e. $\vec{j}_q=0$), for which eq. [3] provides:

$$\alpha = -\frac{\vec{\nabla}\varphi}{\nabla T} \approx -\frac{\left(\frac{\Delta\varphi}{L}\right)}{\left(\frac{\Delta T}{L}\right)} = -\frac{\Delta\varphi}{\Delta T} \quad [7]$$

As expressed by eq. [7], for balanced gradients of potentials referring to a sample of length L , the gradients ∇ can be substituted by the drops Δ of potentials along this length.

Microstructure Analysis

A basic unit was cut from the thermoelectric generator and polished using diamond-lapping films (Allied High Tech Multiprep) for field-emission scanning electron microscopy (FE-SEM) investigations using a JEOL JSM-6700F, which was equipped with an Oxford Instruments INCA 300 energy-dispersive X-ray spectrometer (EDXS) for elemental analysis. The phase composition of the bulk n- and p-type $\text{Bi}_{2-x}\text{Sb}_x\text{Te}_3$ -legs was analyzed by X-ray diffraction (XRD) using a Bruker D8 Advance with Cu-K_α radiation. The legs were isolated from the TEG and prepared for XRD measurements by pressing the ductile material onto the sample holder to increase the detectable area of the samples. This preparation approach caused an orientation in the crystal structure, which was considered in the analysis of the diffraction data. The XRD measurement results were analyzed using the Rietveld method as implemented in Topas 4.2. The reference data for the structure analysis were taken from the Inorganic Crystal Structure Database (ICSD).

Finite-Element Simulations

Using a script-based input process referring to the Analysis System (ANSYS), changes in thermoelectric properties as a result of changing material parameters, such as the composition and geometry of the considered

materials, and the number of legs can be rematched very easily. The used ANSYS version is 15.0 academic. The script-based input tool uses the ANSYS Parametric Design Language (APDL). The simulation process can be separated into three basic steps: preprocessing, solving and postprocessing. During the preprocessing step, the geometric properties are created, the material's properties are set, the model is meshed and additional conditions are defined. Meshing determines the number of elements of the model and their nodes. The accuracy is given by the network's density. After the preprocessing is complete, solving of the grid points is executed. During the postprocessing step, the results are exported as plots, tables or figures. In this work, as mentioned in Section "Estimation of the Geometric and Thermoelectric Properties of the Thermoelectric Generator", a commercially available TEG was measured to estimate the average data for the thermoelectric properties and to evaluate a model system created using the FEM simulation tool. The modeled device consists of 72048 elements. Each thermoelectric leg is build up by 36 elements (total number of elements for the thermoelectric legs is 5,112) while each electric copper connector contains 220 elements (total number of elements for the electric copper connectors is 31,460). Each alumina cover plate consists of 17,138 (total number of elements for the alumina cover plates is 35,476). The non-linear solution converged after equilibrium iteration 2.

Results and Discussion

Microstructure of Materials

To estimate the elemental composition of the thermoelectric materials using the EDXS method in the FE-SEM, a two-leg fragment was cut from the TEG and polished. The SEM micrograph in Figure 3(a) shows the thermoelectric n- and p-type $\text{Bi}_{2-x}\text{Sb}_x\text{Te}_3$, the electric copper connectors and the alumina cover plates. The geometrical parameters are the same as those obtained from the photomicrograph of Figure 2(a), (b). Figure 3(b)–(f) shows the EDXS elemental distribution in the device by bright contrast.

Figure 4 presents the EDX spectra of the n- and p-type material (areas of analysis are marked in Figure 3(a)). The EDXS analysis does not detect any amount of antimony inside the n-type thermoelectric semiconductor. However, Kouhkarenko et al. (2001) reported that doping with a certain amount of antimony, approximately 25 at.% in the bismuth telluride structure,

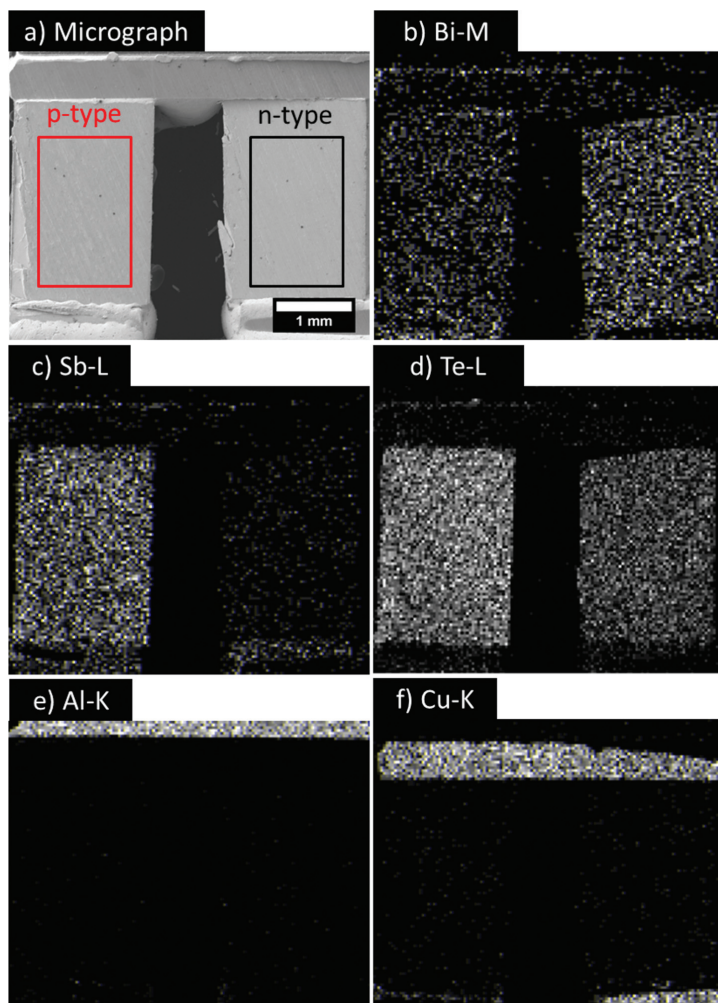


Figure 3: Side view of basic unit of the TEG exhibiting p- and n-type thermoelectric legs; (a) secondary electron micrograph, (b) Bi-M, (c) Sb-L, (d) Te-L, (e) Al-K, (f) Cu-K. Rectangularly marked areas in (a) refer to EDX spectra shown in Figure 4.

leads to an improvement in the Seebeck coefficient α of the n-type thermoelectric material. The thermoelectric properties of $\text{Bi}_{2-x}\text{Sb}_x\text{Te}_3$ are also influenced by the ratio of (Bi,Sb) and Te; see Fleuri et al. (1988). The ideal ratio for a stoichiometric composition $(\text{Bi,Sb})_2\text{Te}_3$ is $\frac{(\text{Bi,Sb})}{\text{Te}} = \frac{2}{3} = 0.667$. Within the accuracy of quantitative EDXS, both materials (n-type and p-type) match this value, which supports the assumption that the materials have been made according to the strategy described by Kouhkarenko et al. (2001).

The composition of the analyzed materials of the TEG is as expected. As indicated by the XRD pattern in Figure 5, the structure is preferentially orientated with the c-axis perpendicular to the sample holder, which is confirmed by the appearance of lattice reflections from

the $(0\ 0\ l)$ planes with $l = 9, 12, 15$ (main reflection), 18, and 21. Furthermore, reflections from the $(1\ 0\ l)$ planes with $l = 10, 13, 25, 28$ are present, which, however, indicates only a slight tilt away from the c-axis. For refinement of the crystal structure, the preferred orientation resulting from the preparation (pressing of ductile material onto the sample holder) has to be considered. Because of the considerable amount of the Sb in the p-type material, the lattice parameters for this composition are smaller than those for the n-type material. The radii for structure-building elements can be extracted from Shannon (1976). With a medial coordination number of 6, it is 76 pm for Sb^{3+} , 103 pm for Bi^{3+} , and 221 pm for Te^{2-} . For the n-type material, which contains only Bi on the cationic site, the diffraction data were fitted to the

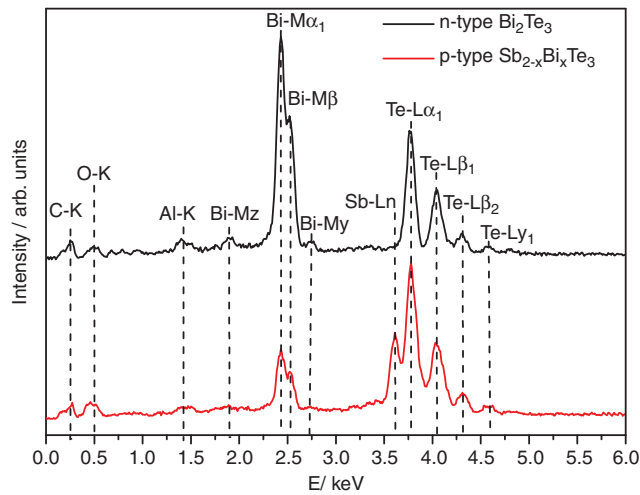


Figure 4: EDX spectra of n- and p-type thermoelectric legs according to the rectangular areas marked in Figure 3(a).

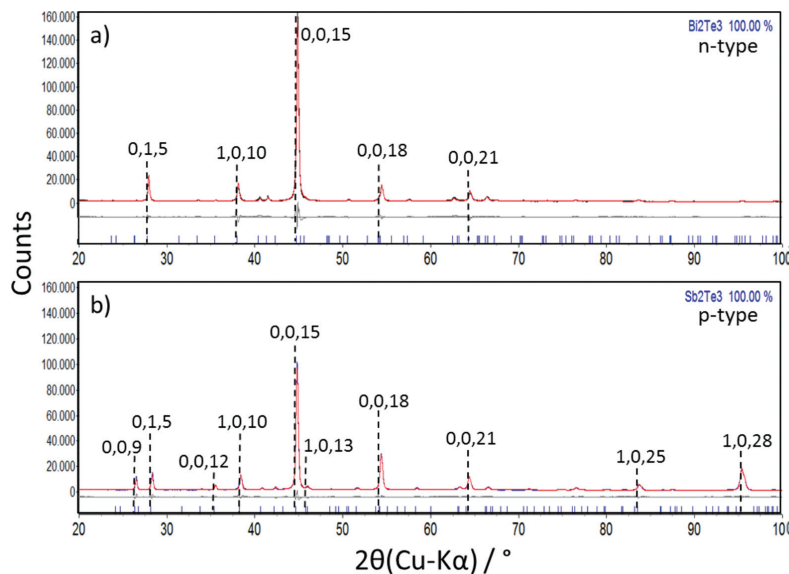


Figure 5: Scanned (black curve) and refined (red curve) X-ray diffraction data with difference curve (light gray); (a) n-type Bi_2Te_3 , (b) p-type $\text{Sb}_{2-x}\text{Bi}_x\text{Te}_3$.

reference structure of Bi_2Te_3 . For the p-type material, which contains a large amount of Sb on the cationic site, the diffraction data were fitted to the reference structure of Sb_2Te_3 . The lattice parameters that were calculated by fitting the diffraction data to the aforementioned reference structures are listed in Table 2.

The results for the atomic positions considering the goodness of the Rietveld fit are listed in Table 3. The coordinates $x = 0$ and $y = 0$ are fixed. The goodness of fit (GOF) is expressed by the R-weighted pattern R_{wp}

and R-expected R_{exp} . For the fit criteria used in Topas 4.2 see Young (1993).

Thermoelectric Investigations

To estimate the thermoelectric properties of the TEG, the measurement data were analyzed and the average values for the specific electrical conductivity $\sigma(T)$, the Seebeck coefficient $\alpha(T)$ from the thermovoltage $U(T)$ and the

Table 2: Lattice parameters and unit cell volumes obtained from the Rietveld refinement and comparison to references. The space group, No. 166, is represented in hexagonal axes.

Stoichiometry	Description	Space group	a/Å	c/Å	V _{cell} /Å ³
Bi ₂ Te _{3-y}	Measured (n-type)	R- $\bar{3}$ mH	4.367	30.401	502.01
Bi ₂ Te ₃	ICSD: 158366	R- $\bar{3}$ mH	4.385	30.497	502.82
Sb _{2-x} Bi _x Te _{3-y}	Measured (p-type)	R- $\bar{3}$ mH	4.280	30.439	482.89
Sb ₂ Te ₃	ICSD: 2084	R- $\bar{3}$ mH	4.264	30.458	479.59

Table 3: Atomic positions and goodness of fit for the Rietveld refinement of the X-ray diffraction data presented in Figure 5. The coordinates $x = 0$ and $y = 0$ are fixed.

Description	Atom	Site	z coordinate ICSD	z coordinate Rietveld	R _{wp}	R _{exp}	GOF
n-type	Bi1	6 c	0.3985	0.3993	9.22	1.87	4.93
	Te1	3 a	0.0	0.0			
	Te2	6 c	0.7919	0.7906			
p-type	Sb1	6 c	0.3988	0.3986	8.54	1.88	4.53
	Te1	6 c	0.7872	0.7874			
	Te2	3 a	0.0	0.0			

temperature difference ΔT for the thermoelectric materials were calculated. The electronic and thermal quantities for copper and alumina were taken from Lide (2008) and are presented in Table 1. A summary of the electronic, thermal and thermoelectric parameters of the thermoelectric materials is given in Table 4. The specific resistivities ρ_{leg} of the legs were estimated from the absolute resistivity of the complete device R_{module} by considering the number of thermoelectric legs and their geometry. The Seebeck coefficient α_{leg} was estimated from the open-circuit voltage U_{OC} according to eq. [7]. Because the coefficient was averaged over all integrated legs, the same absolute values for n- and p-type legs are obtained, and the Seebeck coefficient becomes $\pm\alpha_{leg}$. The maximum electric current I_{SC} under electric short-circuited conditions (i.e. $U = \Delta\varphi = 0$) and the maximum electric output power P_{max} are listed. All quantities are related to the established temperature drops ΔT and the medial temperature of the device T_{medial} .

To determine the thermoelectric parameters of the device, five temperature differences ΔT were established, which are indicated in Table 4 and Figures 6 and 7. Figure 6 shows $U-I$ curves with good agreement between the FEM simulation (solid line) and measurement (data points) for all temperature conditions. Note, that the slope of the lines refers to the internal resistance R_{module} , as indicated in Table 4. The electric output power P_{el} was estimated in terms of different load resistivities R_{load} . Figure 7 shows good agreement between the experimental $P_{el} - I$ curve (data points) and the FEM simulation (solid line).

The results of the thermoelectric behavior can be shown in a vectorial plot that refers to the density of transported quantities, the thermal energy flux density $\vec{j}_{E,th}$ and the electric flux density \vec{j}_q . Figure 8 shows the results of the FEM simulation of the properties of the TEG's components at the maximum electric power output for a chosen temperature difference of 58 K. The colors of

Table 4: Determined thermoelectric parameters of the TEG (complete device) and single legs for different temperature conditions.

T _{hot} /K	ΔT /K	T _{medial} /K	R _{module} /Ω	$\rho_{leg}/\mu\Omega \cdot m$	$\alpha_{leg}/\mu V \cdot K^{-1}$	P _{max} /mW	U _{OC} /mV	I _{SC} /mA
373	58	344	2.28	15.35	± 142.18	144.59	1171	530.74
358	43	337	2.39	16.10	± 158.53	90.42	968	422.97
343	33	327	2.30	15.49	± 144.05	47.42	675	291.08
328	25	316	2.27	15.29	± 131.55	23.22	467	206.45
313	13	307	2.65	17.84	± 107.80	3.73	199	79.75

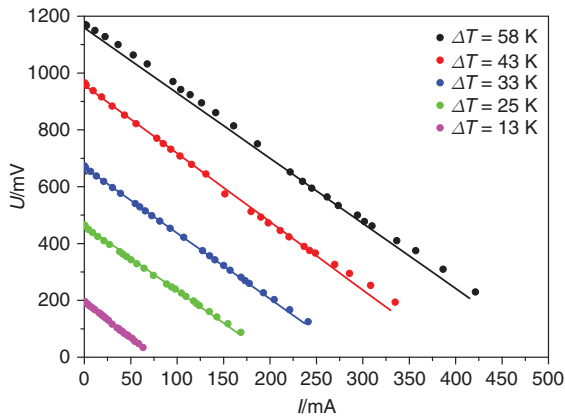


Figure 6: Comparison of measured (dots) and simulated (lines) decrease in voltage over electrical current in terms of load resistance R_L and temperature difference ΔT .

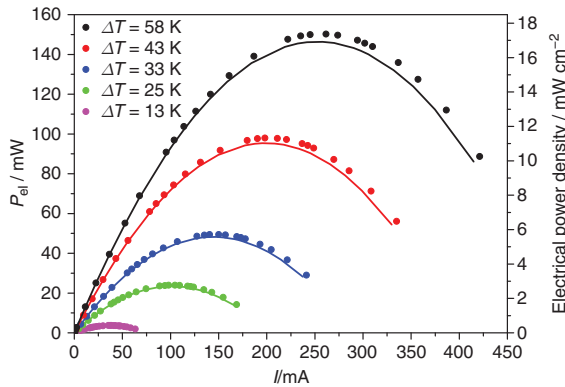


Figure 7: Comparison of measured (dots) power characteristics and simulated (lines) parameters in terms of load resistance R_L and temperature difference ΔT .

the vectors refer to the local value of the density of the transported quantity, which is indicated in the legend. The flux densities of thermal energy $\vec{j}_{E,th}$ and electric charge \vec{j}_q depend on the material of the TEG's components and on the local potential gradients according to the potential distributions of Figure 9. The Al_2O_3 cover plates are not displayed but the flux densities at their location are. From Figure 8(a), it is clear that the thermal power density $\vec{j}_{E,th}$ is distinctly smaller in the region of the Al_2O_3 cover plates ($4W/m^2$) than in the copper connectors ($2 - 4 \cdot 10^4W/m^2$) or the thermoelectric $Bi_{2-x}Sb_xTe_3$ legs ($4 - 5 \cdot 10^4W/m^2$). Due to the extremely high electric resistivity of the Al_2O_3 cover plates (see Table 1), the electric current density \vec{j}_q vanishes at their location. In the copper connectors, it amounts to $\vec{j}_q = 1 \cdot 10^{-17} - 2 \cdot 10^5A/m^2$ with strong local variation, and it is highest in the thermoelectric legs

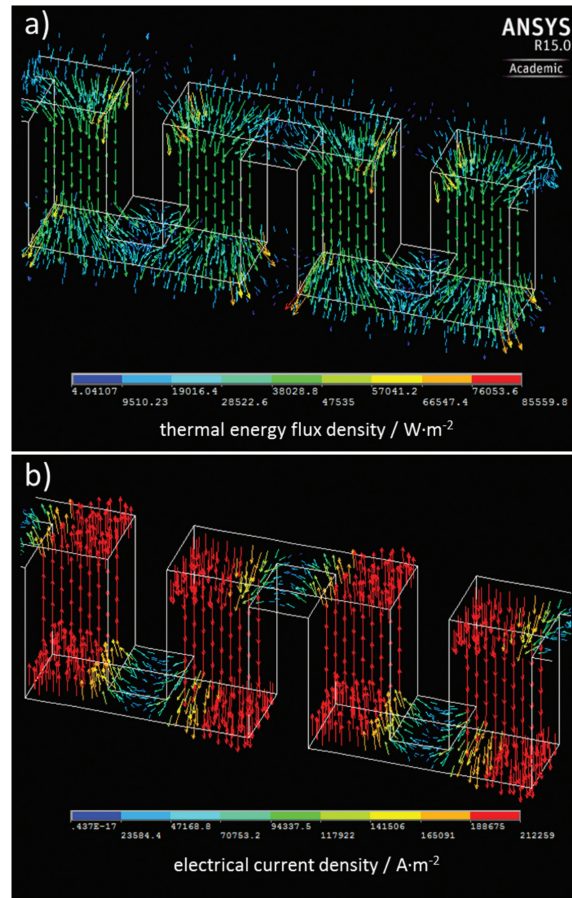


Figure 8: Flux densities of transported quantities with an established temperature difference of 58 K for conditions of maximum electric power output. (a) thermal energy flux density $\vec{j}_{E,th}$, (b) electric flux density \vec{j}_q .

($2 \cdot 10^5A/m^2$). Note that fluxes of thermal energy and electric charge are co-aligned in the case of p-type legs and counter-aligned in the case of n-type legs.

Figure 9(a) shows the distribution of the entropy potential T , obtained from the FEM simulation and a cross-section of the TEG at maximum electric power output for a potential drop of $\Delta T = 58K$. Figure 9(b) shows the respective distribution of the electric potential $U = \Delta\varphi$ along the electric serial connection of the assembled thermoelectric legs and copper connectors inside the module. When the potential at the electric input is at ground (i.e. $\varphi = 0$), it continuously increases along the chain to be $\varphi = 571mV$ at the electric output. Note that this value is identical to the voltage at the electric power maximum (from Figure 7) in Figure 6 for the same temperature drop. The modeling of TEGs using

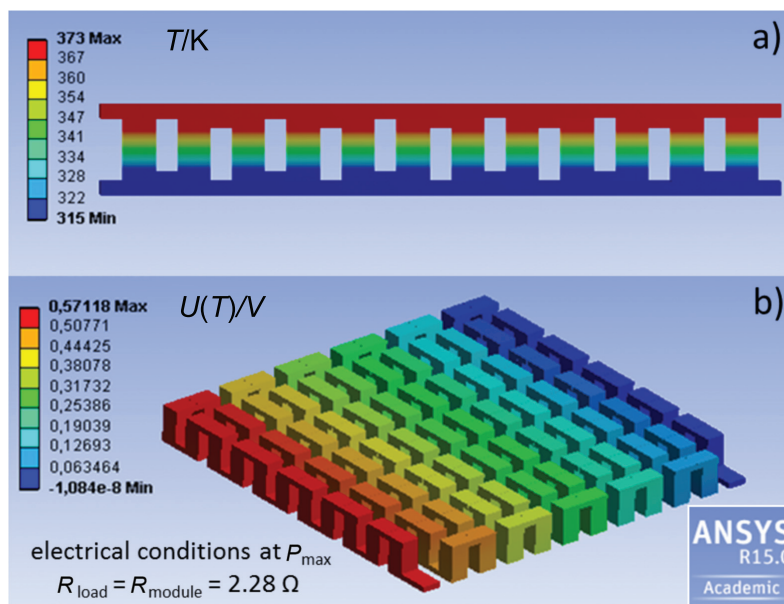


Figure 9: Potential distributions in the TEG at the electric power maximum and referring to the temperature difference of 58 K as obtained from the finite-element simulation: (a) temperature distribution referring to the local entropy potential, (b) established electric potential.

the FEM method has the advantage of providing deep insight into the distribution of all relevant quantities throughout the entire module.

The results from the finite-element simulation illustrate the relation between the entropy potential T and electric potential φ , which is given algebraically in eq. [3] by the respective gradients, and the obtained flux densities $\vec{j}_{E,th}$ (see eq. [1]) and \vec{j}_q .

Conclusions

The model thermoelectric system created from the finite-element simulation provides results with acceptable accuracy. The latter is estimated from the good agreement between simulation and experimental data in the case of voltage–electric current ($U - I$) curves and electric power–electric current ($P_{el} - I$) curves for different temperature situations. Deep insights into the local variations of the relevant thermoelectric parameters can be obtained from this type of modeling. Overall, the developed model system can predict the thermoelectric properties of a certain TEG quite well if the proper parameters for feeding the simulation tool are selected. Work on thermoelectric materials and systems benefits from the use of FEM simulations to check the properties before constructing a device. The properties of the regarded

systems can be varied very easily, thus making FEM tools a very flexible possibility for predicting the power characteristics of a thermoelectric device in terms of the requirements for its application.

References

- Falk, G., F. Herrmann, and G. Schmid. 1983. “Energy Forms or Energy Carriers?” *American Journal of Physics* 51: 1074–77.
- Feldhoff, A. 2015. “Thermoelectric material tensor derived from the Onsager – de Groot – Callen model.” *Energy Harvesting and Systems* 2 (1): 5–13.
- Feldhoff, A., and B. Geppert. 2014a. “Erratum to EHS 1 (1–2), 69–78 (2014): A High-Temperature Thermoelectric Generator Based on Oxides.” *Energy Harvesting and Systems* 1 (3–4): 251.
- Feldhoff, A., and B. Geppert. 2014b. “A High-Temperature Thermoelectric Generator Based on Oxides.” *Energy Harvesting and Systems* 1 (1–2): 69–78.
- Fleurial, J., L. Gailliard, R. Triboulet, H. Scherrer, and S. Scherrer. 1988. “Thermal Properties of High Quality Single Crystals of Bismuth Telluride – Part I: Experimental Characterization.” *Journal of Physics and Chemistry of Solids* 49: 1237–47.
- Fuchs, H. 2010. *The Dynamics of Heat – A Unified Approach to Thermodynamics and Heat Transfer*. 2nd edition. Graduate Texts in Physics. New York, NY: Springer.
- Fuchs, H. 2014. “A Direct Entropic Approach to Uniform and Spatially Continuous Dynamical Models of Thermoelectric Devices.” *Energy Harvesting and Systems* 2: 1–13.

- Hejtmanek, J., K. Knizek, V. Svejda, P. Horna, and M. Sikora. 2014. "Test System for Thermoelectric Modules and Materials." *Journal of Electronic Materials* 43: 3726–32.
- Ioffe, A. 1957. *Semiconductor Thermoelements and Thermoelectric Cooling*. 1st edition. London: Infosearch Ltd.
- Kim, C., D. H. Kim, H. Kim, and J. S. Chung. 2012. "Significant Enhancement in the Thermoelectric Performance of Bismuth Telluride Nanocompound Through Brief Fabrication Procedures." *ASC Applied Materials and Interfaces* 4: 2949–54.
- Kouhkarenko, E., N. Frety, V. G. Shepelevich, and J. C. Tedenac. 2001. "Electrical Properties of $\text{Bi}_{2-x}\text{Sb}_x\text{Te}_3$ Materials Obtained by Ultrarapid Quenching." *Journal of Alloys and Compounds* 327: 1–4.
- Kuznetsov, V. L., L. A. Kuznetsova, A. E. Kaliazin, and D. M. Rowe. 2002. "High Performance Functionally Graded and Segmented Bi_2Te_3 -Based Materials for Thermoelectric Power Generation." *Journal of Materials Science* 37: 2893–97.
- Lide, D. 2008. *CRC Handbook of Chemistry and Physics*. 89th edition. Internet Version 2009. Boca Raton, FL: CRC Press.
- Poudel, B., Q. Hao, Y. Ma, Y. Lan, A. Minnich, B. Yu, X. Yan, D. Wang, A. Muto, D. Vashaee, et al. 2008. "High-Thermoelectric Performance of Nanostructured Bismuth Antimony Telluride Bulk Alloys." *Science* 320: 634–38.
- Schneider, C., A. Rasband, and K. Eliceiri. 2012. "NIH to ImageJ: 25 Years of Image Analysis." *Nature Methods* 9: 671–75.
- Shannon, R. 1976. "Revised Effective Ionic Radii and Systematic Studies of Interatomic Distances in Halides and Chalcogenides." *Acta Crystallographica A* 32: 751–67.
- Young, R. 1993. *Introduction to the Rietveld Method*. IUCr Book series. Oxford: Oxford University Press.

3.5 Experimental Characterisation and Finite-Element Simulations of a Thermoelectric Generator with Ceramic p-type $\text{Ca}_3\text{Co}_4\text{O}_9$ and Metallic $\text{Cu}_{0.57}\text{Ni}_{0.42}\text{Mn}_{0.01}$ legs

Benjamin Geppert, Dennis Groeneveld, Michael Bittner

and Armin Feldhoff

Journal of Energy Harvesting and Systems, submitted, (2016)

Experimental Characterisation and Finite-Element Simulations of a Thermoelectric Generator with Ceramic p-type $\text{Ca}_3\text{Co}_4\text{O}_9$ and Metallic n-type $\text{Cu}_{0.57}\text{Ni}_{0.42}\text{Mn}_{0.01}$ legs

Benjamin Geppert, Dennis Groeneveld, Michael Bittner and Armin Feldhoff

This study presents the characterisation of a prototype thermoelectric generator including ceramic $\text{Ca}_3\text{Co}_4\text{O}_9$ p-type and metallic $\text{Cu}_{0.57}\text{Ni}_{0.42}\text{Mn}_{0.01}$ n-type legs. The generator was constructed applying the conventional rigid chessboard design, which provides an electrical series connection of the thermoelectrically active materials in between of two electrical isolating cover plates made of alumina. Ag-epoxy resin was used for electric connectors which were directly bonded to the thermoelectrically active materials. The generator was rebuild in the framework of a finite-element model to simulate the generator's transport characteristics using the physical data of the single materials as input parameters for the simulation tool. The simulation results give a view to the distributions of temperature and electric potential as well as vector plots showing the generated current density of charge inside the regarded materials. The finite-element simulation tool was used to consider the electrical contact resistivities between the thermoelectric legs and the connector material. The input parameter for the specific isothermal electric resistivity of the Ag-epoxy connectors were varied by including the electrical contact resistances to match the simulated to the measured data in order to receive the correct electric current densities in the modeled device.

Introduction

The development and application of thermoelectric materials, for example, for harvesting electrical power from waste heat sources, is a current field of study that requires interdisciplinary investigations. The implementation of newly developed thermoelectric materials into thermoelectric generators (TEGs) benefits from modeling the thermoelectric properties of the generators with respect to the individual properties of the employed materials. A TEG is a device that transfers energy from thermal (entropy) current to electric current¹⁻³. The concept of energy carriers⁴ enables an elegant description of a thermoelectric device, which relies on considering the flux densities of the aforementioned fluid-like quantities entropy S and electric charge q and their linkage to the conjugated potentials, which are the absolute temperature T and the electric potential φ , respectively. The currents of thermal energy (heat) and electric energy are then obtained as already shown^{2,3,5,6}. Taking the cross-sectional areas A_{leg} and the length L_{leg} of the thermoelectric material samples into account, the currents of entropy I_S and electric charge I_q in a thermoelectric material, that is subjected to differences of thermal potential ΔT and electric potential $\Delta\varphi$, can be easily obtained if a thermoelectric material tensor is considered³:

$$\begin{pmatrix} I_S \\ I_q \end{pmatrix} = -\frac{A_{leg}}{L_{leg}} \cdot \begin{pmatrix} \sigma \cdot \alpha^2 + \Lambda & \sigma \cdot \alpha \\ \sigma \cdot \alpha & \sigma \end{pmatrix} \cdot \begin{pmatrix} \Delta T \\ \Delta\varphi \end{pmatrix} \quad (1)$$

The thermoelectric tensor consists of three tensorial quantities, the specific electrical conductivity σ under isothermal conditions (i.e., $\nabla T = 0$), the specific entropy conductivity Λ under electric open-circuited conditions (i.e., $I_q = 0$) and the Seebeck coefficient α . Special cases that can be received under certain conditions of Equation 1 were elucidated^{2,3,5,6}.

The basic unit of a thermoelectric generator can be constructed by connecting two materials with different algebraic signs for the Seebeck coefficient α thermally in parallel and electrically in series. For $\alpha < 0$, the motions of thermal and electrical fluxes are directed in the same way. In contrast, for $\alpha > 0$, the thermal and electrical fluxes are directed in opposite directions⁵. By additively connecting several of these basic units thermally in parallel and electrically in series, the electric potential φ can be increased over the device³ for illustration. The choice of the thermoelectric materials that comprise the TEG depends on the conditions under which the energy conversion is to be performed.

Among the various thermoelectric materials, semiconductors exhibit the best thermoelectric conversion efficiency because of their moderate charge carrier concentration, and they provide a

good balance between specific electric conductivity σ , the Seebeck coefficient α and the thermal conductivity⁷. Alloys provide high values of the so-called power factor $\sigma \cdot \alpha^2$, which is the charge-coupled entropy conductivity and occurs as part of the thermoelectric tensor in Equation 1. Consequently, alloys and semiconductors are chosen as thermoelectrically active materials. To obtain a good TEG performance, the combination of n- and p-type materials and a low-resistance electrical connection between them realized by metals or alloys is preferred. In case of the present study, a composite connector material, Ag-epoxy resin, was used.

Additionally, the geometric properties of the materials that are combined to form the complete device have to be optimized for every system. Finite-element method (FEM) simulations are useful for calculating the thermoelectric performance in terms of the used materials and their geometric properties without constructing a real TEG. The thermoelectric properties can be measured for each individual material. Afterwards, the materials can be combined in a simulated TEG system with a specific geometry. The absolute currents I are correlated to the current densities j considering the cross-sectional areas of the thermoelectric material legs A_{leg} , as shown in Equation 2 and 3.

$$I_S = A_{leg} \cdot j_S \quad (2)$$

$$I_q = A_{leg} \cdot j_q \quad (3)$$

Under electric open-circuit conditions, Equation 1 yields the entropy current I_S through the thermoelectric material by Fourier's law:

$$I_S = -\frac{A_{leg}}{L_{leg}} \cdot \Lambda \cdot \Delta T \quad (4)$$

The specific entropy conductivity Λ is related to the specific heat conductivity λ by the absolute working temperature T ¹⁻³.

$$\lambda = T \cdot \Lambda \quad (5)$$

Under isothermal conditions, Equation 1 yields the electric current I_q through the thermoelectric material by Ohm's law:

$$I_q = -\frac{A_{leg}}{L_{leg}} \cdot \sigma \cdot \Delta\phi \quad (6)$$

Experimental

Thermoelectric measurement setup

To characterise the thermoelectric properties of the materials, the temperature-dependent isothermal specific electric resistivity and the Seebeck coefficient, as estimated from the thermovoltage, were measured. A precision vertical diamond wire-saw model 3242 from O'WELL was used for sample preparation. Thermoelectric properties were measured using a measurement cell constructed in-house. The sample was clamped between two platinum electrodes to close the electric circuit in a pseudo-four-point measurement. The applied furnace was an ELITE thermal system. The Seebeck coefficient was measured using a NORECS Probatat

measurement system. The electronic parameters were measured with KEITHLEY 2100 6½ digit multimeters. The measured data were converted using LAB VIEW software.

To estimate the thermoelectric characteristics of the constructed TEG, it was placed between a heat source (ceramic hot-plate) and a heat sink (passive cooler). A photomicrograph of the measurement setup is shown in Figure 1.

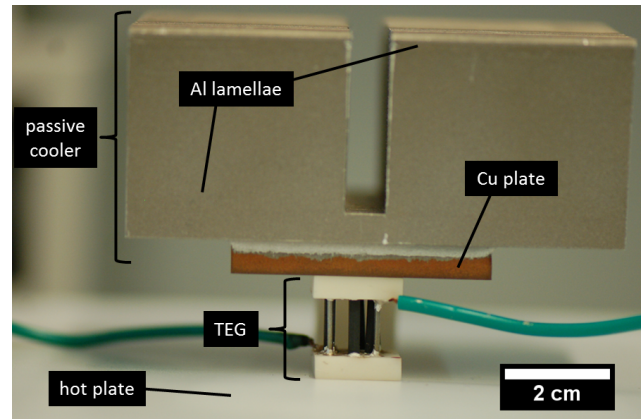


Fig. 1 Photomicrograph of the measurement setup for determination of the thermoelectric characteristics of the constructed TEG. Note that the p-type ceramic material is integrated as rectangular bars while the n-type wire material exhibits the form of a cylinder.

The temperature data were collected using thermocouples. The voltage $\Delta\phi$ was measured as the drop of the electric potential on the external load R_{load} . The electric output power P_{el} was estimated according to:

$$P_{el} = I_q \cdot \Delta\phi \quad (7)$$

The resistivity of the thermoelectric generator was estimated by analysing the electric current-voltage characteristics using Ohm's law for the entire device (see Equation 6 for the corresponding relation for single materials).

$$\Delta\phi = R_{TEG} \cdot I_q \quad (8)$$

Microstructure analysis

The phase composition of the metallic n-type and ceramic p-type materials was analyzed by X-ray diffraction (XRD) using a Bruker D8 Advance with Cu-K α radiation. The thermoelectric bulk materials were polished using diamond-lapping films (Allied High Tech Multiprep) for field-emission scanning electron microscopy (FE-SEM) investigations using a JEOL JSM-6700F, which was equipped with an Oxford Instruments INCA 300 energy-dispersive X-ray spectrometer (EDXS) for elemental analysis.

Materials choice

The p-type leg material was realized by applying ceramic Ca₃Co₄O₉. This layered cobaltite phase exhibits an incommensurate structure and provides attractive thermoelectric properties⁸. Measured thermoelectric parameters for polycrystalline samples

3.5 Experimental Characterisation and Finite-Element Simulations of a Thermoelectric Generator with Ceramic p-type $\text{Ca}_3\text{Co}_4\text{O}_9$ and Metallic $\text{Cu}_{0.57}\text{Ni}_{0.42}\text{Mn}_{0.01}$ legs

from various laboratories were assembled⁹. Single crystals of $\text{Ca}_3\text{Co}_4\text{O}_9$ exhibit a figure of merit $ZT = 0.83$ at 973 K ¹⁰. The high charge carrier density around room temperature makes the $\text{Ca}_3\text{Co}_4\text{O}_9$ ceramic also usable as thermoelectric material for low- and intermediate-temperature devices.

As n-type material a Cu-Ni based alloy was used. For energy conversion in the intermediate temperature range such metallic compounds show useful properties. The electric resistance is very low and the value for the Seebeck coefficient is acceptable. That makes such alloys the material class reaching highest values of the power factor. We already used this material combination for the construction of flexible thermoelectric generators¹¹. Measured thermoelectric properties were summarized in round-robin measurements and reported^{12,13}.

The series connection of n- and p-type legs of the generator was realized using Ag-epoxy resin as electrical conductive glue. The bulk resistivity was reported with a value of $0.9\text{ m}\Omega\text{ cm}^{-1}$.

For the cover plates, commonly used Al_2O_3 was applied.

Finite-element simulations

In this work, a prototype thermoelectric generator was constructed and rebuilt in the FEM tool using ANSYS Mechanical APDL version 15.0 academic. The specific resistivity of the Ag-epoxy resin was adapted in the simulation to match the measured transport properties and to obtain the correct electric currents in the modeled device. The model consists of 14268 elements. Each thermoelectric p-type leg is build up from 48 elements (total number of p-type material elements for the thermoelectric legs is 192) while the total number of elements for the electrical Ag-epoxy connectors is 2964. Each alumina cover plate consists of 1482 elements. The non-linear solution converged after 5 equilibrium iteration. The constructed and modeled device is presented in Figure 2. The geometric parameters of applied materials, that are input parameters for the FEM tool, are listed in Table 1.

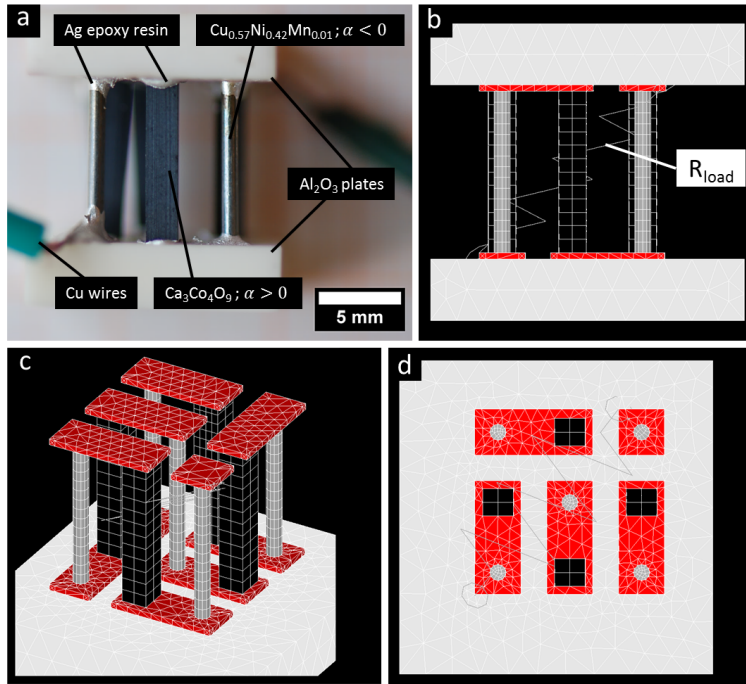


Fig. 2 View on the constructed and modeled thermoelectric device. a) Side-view of constructed TEG, b) Side-view of modeled device, c) Perspective view of modeled device, d) Top-view on modeled device.

Table 1 Measured geometric properties of the TEG's components: length L and cross-sectional area A of applied material. The fill-factor of the TEG exhibits a value of 7.5 %.

component	material	L / mm	A / mm ²	description
p-type leg	$\text{Ca}_3\text{Co}_4\text{O}_9$	10.0	3.23	house-made ceramic
n-type leg	$\text{Cu}_{0.57}\text{Ni}_{0.42}\text{Mn}_{0.01}$	10.0	0.79	commercial alloy
el. connector	Ag-epoxy resin	0.44	5.32	commercial composite
cover plates	Al_2O_3	3.8	225	commercial ceramic

Results and discussion

Microstructure of materials

The crystallographic phases of the sintered p-type $\text{Ca}_3\text{Co}_4\text{O}_9$ ceramic and the n-type $\text{Cu}_{0.57}\text{Ni}_{0.42}\text{Mn}_{0.01}$ alloy were confirmed by Rietveld refinement of measured X-ray diffractograms. The diffractograms (blue curves) of the thermoelectric materials are presented in Figure 3 together with the Rietveld fits (red curves).

$\text{Ca}_3\text{Co}_4\text{O}_9$ crystallizes in the monoclinic system and exhibits the Cm symmetry for both subsystems (b_1, b_2). $\text{Cu}_{0.57}\text{Ni}_{0.42}\text{Mn}_{0.01}$ crystallizes in the cubic system exhibiting the spacegroup $Fm\bar{3}m$. The p-type $\text{Ca}_3\text{Co}_4\text{O}_9$ ceramic was vibration-polished to estimate the arrangement of plate-like grains inside the bulk material. In Figure 4, a secondary electron micrograph of the ceramic material is presented. The black areas are internal pores.

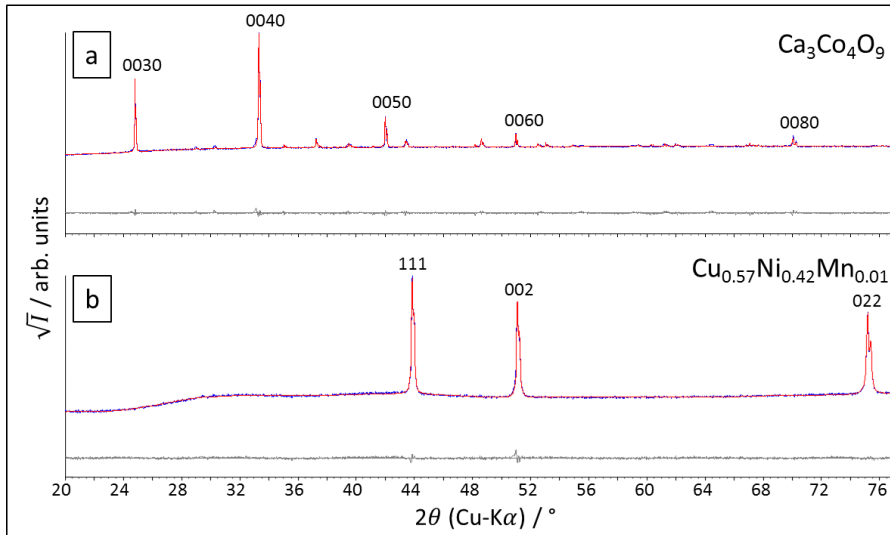


Fig. 3 Measured X-ray diffractograms (blue curves) with Rietveld fits (red curves) and differential curve (grey curves). a) p-type $\text{Ca}_3\text{Co}_4\text{O}_9$ ceramic, b) n-type $\text{Cu}_{0.57}\text{Ni}_{0.42}\text{Mn}_{0.01}$ alloy. The counts are presented as square-root values.

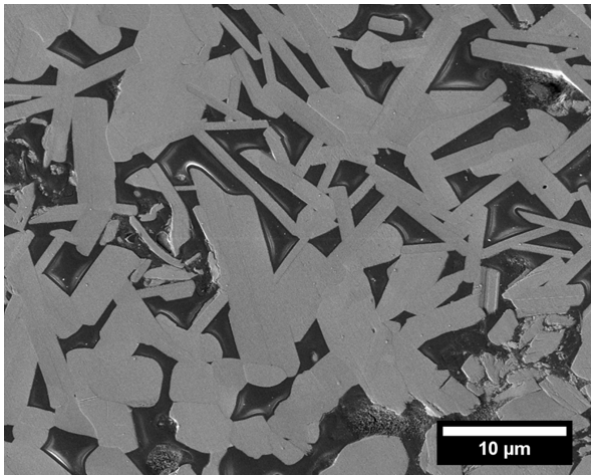


Fig. 4 Secondary electron micrograph of the vibration-polished p-type $\text{Ca}_3\text{Co}_4\text{O}_9$ ceramic material.

3.5 Experimental Characterisation and Finite-Element Simulations of a Thermoelectric Generator with Ceramic p-type $\text{Ca}_3\text{Co}_4\text{O}_9$ and Metallic $\text{Cu}_{0.57}\text{Ni}_{0.42}\text{Mn}_{0.01}$ legs

Thermoelectric investigations

Table 2 lists measured or reported values for the transport properties of each material that was applied in the generator. The electronic and thermal quantities for the Al_2O_3 plates and for the Ag-epoxy resin were taken from manufacturers data. To estimate the thermoelectric properties of the TEG, the device was characterized in the setup shown in Figure 1. The temperature-dependent resistivity of the entire device R_{TEG} was estimated by applying Ohm's law (Equation 8) to the TEG's measurement data. In Table 3 the values for the determined contact resistances are listed together with the maximum electric current $I_{q,SC}$ under electric short-circuit conditions (i.e. $\Delta\phi = 0$), the open-circuit voltage $\Delta\phi_{OC}$ (i.e. $I_q = 0$) and the maximum electric output power $P_{el,max}$. All quantities are related to the established temperature drops ΔT and the median temperature of the device T_{median} .

The FEM simulation resulted in accurate values for the open-circuit voltage $\Delta\phi_{OC}$ (device Seebeck-voltage) but in too high values for the short-circuit electric current $I_{q,SC}$. This makes the calculated values for the resistivity of the generator too low and the electric output power too high. The reason for the FEM solutions to be inaccurate is seen in contact resistivities between the Ag-epoxy resin and the thermoelectrically active materials.

Table 2 Determined or reported thermoelectrical parameters of applied materials. Simulation A assumes vanishing contact resistances and Simulation B accounts for non-vanishing contact resistances by considering them by varying the effective resistance ρ of the connector material.

material	T / K	ρ / $\text{m}\Omega \cdot \text{cm}$	α / $\mu\text{V} \cdot \text{K}^{-1}$	λ / $\text{W} \cdot \text{m}^{-1} \cdot \text{K}^{-1}$	Λ / $\text{W} \cdot \text{m}^{-1} \cdot \text{K}^{-2}$
$\text{Ca}_3\text{Co}_4\text{O}_9$	363	59.21	147.39	0.62	$1.7 \cdot 10^{-3}$
	403	49.93	154.95	0.59	$1.5 \cdot 10^{-3}$
	443	36.58	162.53	0.57	$1.3 \cdot 10^{-3}$
	478	32.66	169.12	0.57	$1.2 \cdot 10^{-3}$
$\text{Cu}_{0.57}\text{Ni}_{0.42}\text{Mn}_{0.01}$	300-500	$4.7 \cdot 10^{-2}$	-40	23	$7.7 \cdot 10^{-2}$
Al_2O_3 plates	300	$1 \cdot 10^{17}$	n.a.	30	$1 \cdot 10^{-1}$
Ag-epoxy resin (Simulation A)	300	0.9	n.a.	1	$3.3 \cdot 10^{-3}$
Ag-epoxy resin (Simulation B)	363	$2.55 \cdot 10^3$	n.a.	1	$2.8 \cdot 10^{-3}$
	403	$1.65 \cdot 10^3$	n.a.	1	$2.5 \cdot 10^{-3}$
	443	$5.10 \cdot 10^2$	n.a.	1	$2.3 \cdot 10^{-3}$
	478	$4.30 \cdot 10^2$	n.a.	1	$2.1 \cdot 10^{-3}$

Table 3 Estimated thermoelectric parameters of the constructed TEG for different temperature conditions.

T_{hot} / K	ΔT / K	T_{median} / K	R_{TEG} / Ω	$P_{el,max}$ / μW	$\Delta\phi_{OC}$ / mV	$I_{q,SC}$ / mA	$R_{contact}$ / Ω per contact
389	60	363	415.24	0.93	39.4	0.09	22.66
441	80	403	250.36	2.90	53.9	0.22	19.12
492	100	443	74.50	16.54	70.2	0.94	3.89
536	120	478	63.93	32.52	91.2	1.43	3.33

In order to match the characteristics of the real constructed TEG to the modeled device in the FEM tool, the specific electric resistivity of the Ag-epoxy resin was refined by the implementation of the magnitude of the contact resistances into the values of the specific resistivity of the connector material. The values of the resistivity of the electric connector material was varied until the Ohm-lines of the FEM simulation fitted the measurement data points. In the framework of thermoelectric generator fabrication the formation of contact resistances is a major concern and effect the thermoelectric properties of a certain device on a large scale. The modification of interfaces in thermoelectric generators is an extensive field of study. Material and generator efficiency were compared and it was shown, that the efficiency can decrease up to 59 % comparing the single thermoelectric materials and the entire assembled systems¹⁴. The $\text{Ca}_3\text{Co}_4\text{O}_9$ -related oxide-metal interfaces were studied¹⁵. Figure 5a shows $\Delta\phi - I_q$ curves with bad agreement of the FEM Simulation A, that do not consider the electrical contact resistances (dotted lines), and good agreement of the FEM Simulation B, that do consider the electrical contact resistances (solid lines) with the measurement (data points) for all temperature conditions. Note, that the slope of the lines refers to the internal resistance R_{TEG} , as indicated in Table 3 and 4. The electric output power P_{el} was estimated in terms of different load resistivities R_{load} . The electrical contact resistances limit the magnitude of the electric current inside the device and therefore the electric power output. The power characteristics of measured data and FEM results of simulation B are displayed in Figure 5b.

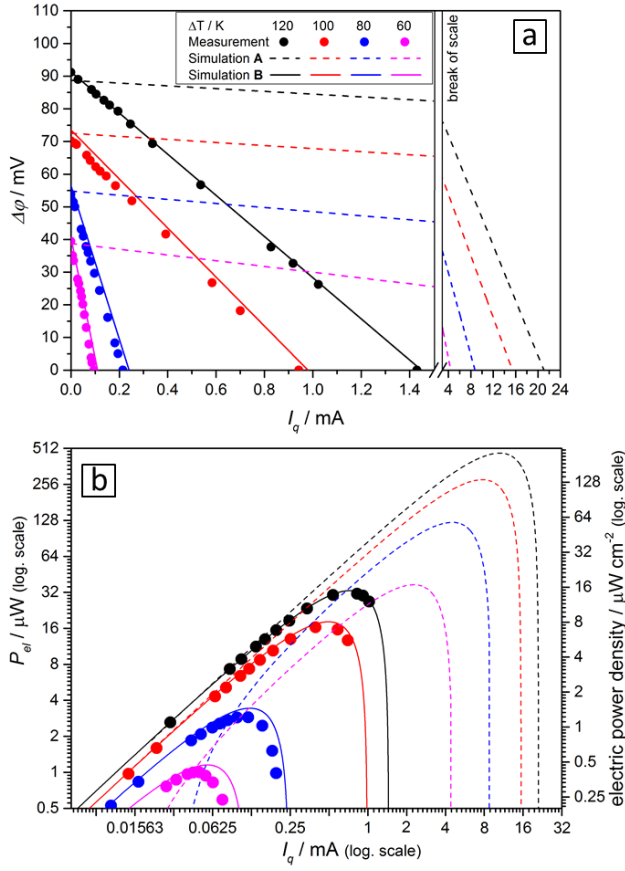


Fig. 5 Measured (dots) and simulated (lines) results for the thermoelectric characteristics of the constructed TEG. a) Electric voltage-current $\Delta\phi$ - I_q characteristics of the measured data and the FEM simulation A (dashed lines) and simulation B (solid lines), b) Electric power-current P_{el} - I_q characteristics for measured data and the FEM simulation A and B. For better comparison, the values are plotted logarithmically.

The simulation results are presented as contour-plots for the potential distributions and as vectorial plots that refer to the density of electric current j_q in simulation A and simulation B. The colors of the vectors refer to the local value of the flux density of the transported quantity, which is indicated in the legend. Figure 6a shows the distribution of the entropy potential T , obtained from the FEM simulation and a perspective view of the TEG at maximum electric power output for a potential drop of $\Delta T = 120$ K. The situation of temperature distribution is equal for simulations A and B. Figure 6b shows the respective distribution of the electric potential $\Delta\phi$ along the electrical serial connection of the assembled thermoelectric legs and electric connectors (Ag-epoxy resin) inside the thermoelectric generator. The displayed simulation results of the TEG are related to the conditions of electric power maximum (from Figure 5b) for a temperature drop of 120 K. The flux density of electric charge j_q depends on the material of the TEG's components and on the local potential gradients according to the potential distributions shown in Figure 6a,b. The modeling of TEGs using the FEM method has the advantage of providing deep insight into the distribution of all relevant quantities throughout the entire device. From Figure 6c,d, it is obvious that the electric current density j_q inside the entire arrangement of materials is much smaller than predicted by simulation A. Therefore, the electric power output predicted by simulation A is more than 10 times higher compared to the electric power received by simulation B and the experiment. In the metallic $\text{Cu}_{0.57}\text{Ni}_{0.42}\text{Mn}_{0.01}$ legs the electric current density is more than 3 times lower in simulation B compared to the results of simulation A. Varying the specific electric resistivity of the electric connector Ag-epoxy resin, by taking the contact resistances into account, results in the correct densities of electric current inside each material. The contact region of the Ag-epoxy resin and the thermoelectric materials limit the electric current density inside the entire generator because electric contact resistances between the connector material and the thermoelectric legs are formed. The results from the finite-element simulation illustrate the relation between the entropy potential T and electric potential ϕ , which is given algebraically in Equation 1 by the respective distribution of potentials, and the obtained electric current I_q .

Table 4 Thermolectric parameters of the modeled TEG for Simulation A and Simulation B.

			Simulation A				Simulation B			
T_{hot}	ΔT	T_{median}	R_{TEG}	$P_{\text{el,max}}$	$\Delta\phi_{\text{OC}}$	$I_{q,\text{SC}}$	R_{TEG}	$P_{\text{el,max}}$	$\Delta\phi_{\text{OC}}$	$I_{q,\text{SC}}$
/ K	/ K	/ K	/ Ω	/ μW	/ mV	/ mA	/ Ω	/ μW	/ mV	/ mA
389	60	363	7.33	37.01	40.4	5.32	355.85	1.15	40.5	0.11
441	80	403	6.11	123.31	53.9	8.82	231.66	3.43	56.4	0.24
492	100	443	4.53	280.01	73.3	15.3	74.31	18.17	73.5	0.98
536	120	478	4.04	467.13	91.0	21.1	62.89	33.12	91.3	1.45

3.5 Experimental Characterisation and Finite-Element Simulations of a Thermoelectric Generator with Ceramic p-type $\text{Ca}_3\text{Co}_4\text{O}_9$ and Metallic $\text{Cu}_{0.57}\text{Ni}_{0.42}\text{Mn}_{0.01}$ legs

Conclusions

The model thermoelectric system created from the finite-element simulation provides results with acceptable accuracy in terms of the values for the open-circuit voltages. The simulation for the current densities and therefore for the electric power output of the generator was predicted with too high values. The overestimation of the electric current density is based on the formation of contact resistivities that were formed at the material boundaries of the Ag-epoxy resin as electric connector and the thermoelectrically active materials. Those contacts in TEG devices can be realized by different materials.

The Ag-epoxy resin exhibits good properties in terms of processibility and mechanical fixation. The adhesive is more heat proved than Sn-Pb based solders. However, the contact resistances in thermoelectric generators are an important concern. Using the finite-element simulation tool, the quantitative electrical contact resistances could be determined. Work on thermoelectric materials and systems benefits from the use of FEM simulations to compare the properties of the modeled and the measured device to gain knowledge on the factors that limit the electric power output of a certain thermoelectric generator.

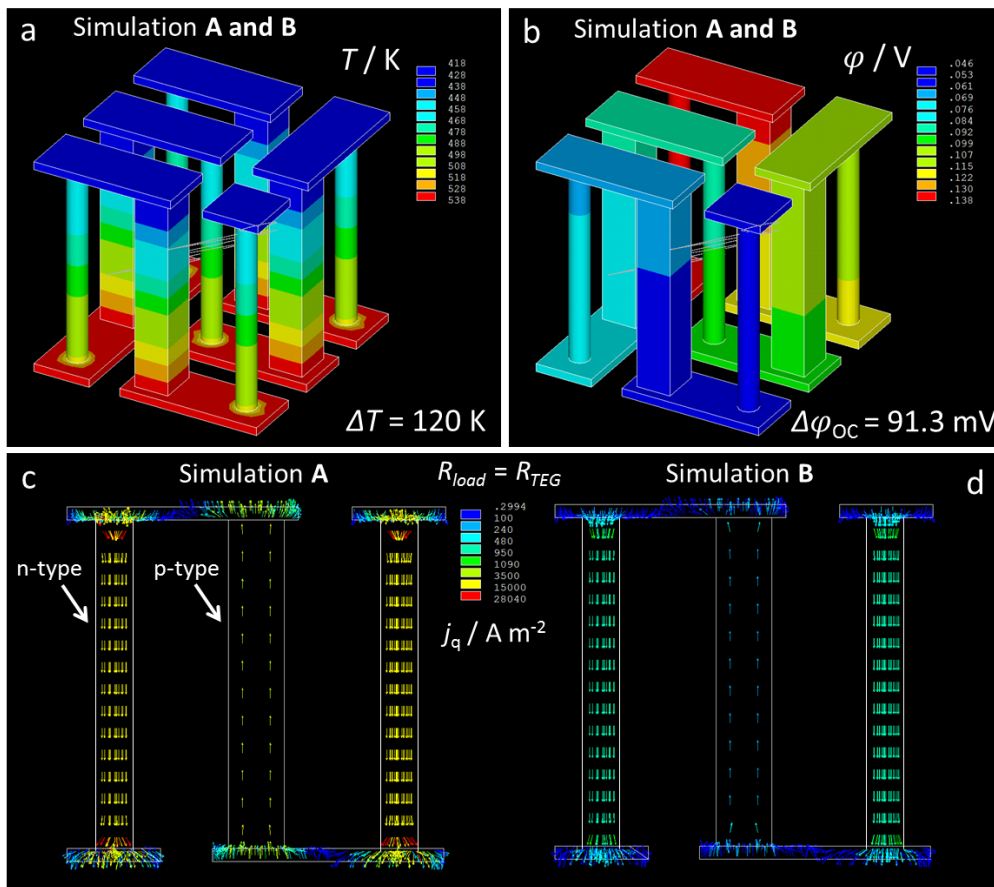


Fig. 6 Simulated results for the thermoelectric characteristics of the constructed TEG. a) Temperature distribution for $\Delta T = 120\text{ K}$ for simulation A and B, b) distribution of electric potential along the electric series connection of TE legs for electric open-circuit conditions (nearly equal values for simulation A and B), c) electric current density j_q for simulation A, d) electric current density j_q for simulation B. Note that the current densities for simulation A and simulation B are correlated to the same color-related legend and refer to electric maximum power condition. For comparison of temperature related quantities see Table 4.

After including the contact resistances into the electric resistivities of the connector material a good match of measured and simulated data were obtained. The Ag-epoxy resin was used as an alternative to soldering that can also exhibit high contact resistivities when ceramic materials are applied. The used thermoelectric materials are p-type $\text{Ca}_3\text{Co}_4\text{O}_9$ ceramic and n-type $\text{Cu}_{0.57}\text{Ni}_{0.42}\text{Mn}_{0.01}$ alloy. The FEM simulation was used to estimate the limiting factor in terms of electric power output. The theoretical maximum power was calculated to almost $500 \mu\text{W}$ with a temperature difference of $\Delta T = 120 \text{ K}$, while the measured maximum electric power output for the same temperature conditions was only $32.5 \mu\text{W}$. The FEM results show that a minimization of the contact resistances in TEG devices can dramatically increase the electric output power. At lower temperatures the $\text{Ca}_3\text{Co}_4\text{O}_9$ ceramic provides a charge carrier density that is usable also in devices for low-temperature applications. Deep insights into the local variations of the relevant thermoelectric parameters can be obtained from this type of FEM modeling. Overall, the developed model system can predict the thermoelectric properties of a certain TEG quite well if the proper parameters for feeding the simulation tool are selected.

References

- 1 H. Fuchs, *The Dynamics of Heat – A Unified Approach to Thermodynamics and Heat Transfer*, Springer, New York, 2nd edn, 2010, pp. 104 + 169 + 562.
- 2 H. Fuchs, *Energy Harvesting and Systems*, 2014, **2**, 1–13.
- 3 A. Feldhoff, *Energy Harvesting and Systems*, 2015, **2(1-2)**, 5–13.
- 4 G. Falk, F. Herrmann and G. Schmid, *Am. J. Phys.*, 1983, **51**, 1074–1077.
- 5 A. Feldhoff and B. Geppert, *Energy Harvesting and Systems*, 2014, **1(1-2)**, 69–78.
- 6 A. Feldhoff and B. Geppert, *Energy Harvesting and Systems*, 2014, **1(3-4)**, 251.
- 7 A. Ioffe, *Semiconductor Thermoelements and Thermoelectric Cooling*, Infosearch Ltd. London, 1st edn, 1957, p. 96.
- 8 S. Lambert, H. Leligny and D. Gebrille, *Journal of Solid State Chemistry*, 2001, **160**, 322–331.
- 9 J. Fergus, *Journal of the European Ceramic Society*, 2011, **32**, 525–540.
- 10 M. Shikano and R. Funahashi, *Applied Physics Letter*, 2003, **82(12)**, 1851–1851.
- 11 B. Geppert and A. Feldhoff, *Energy Harvesting and Systems*, 2015, **2**, 1–11.
- 12 Z. Q. J. Lu, N. D. Lowhorn, W. Wong-Ng, W. Zhang, Z. Q. Lu, M. Otani, E. Thomas, M. G. T. N. Tran, N. Dilly, S. Ghamaty, N. Elsner, T. Hogan, A. D. Downey, Q. Jie, Q. Li, H. Obara, J. Sharp, C. Caylor, R. Venkatasubramanian, R. Willigan, J. Yang, J. Martin, G. Nolas, B. Edwards and T. Tritt, *Journal of Research of the National Institute of Standards and Technology*, 2009, **114**, 37–55.
- 13 N. D. Lowhorn, W. Wong-Ng, W. Zhang, Z. Q. Lu, M. Otani, E. Thomas, M. G. T. N. Tran, N. Dilly, S. Ghamaty, N. Elsner, T. Hogan, A. D. Downey, Q. Jie, Q. Li, H. Obara, J. Sharp, C. Caylor, R. Venkatasubramanian, R. Willigan, J. Yang, J. Martin, G. Nolas, B. Edwards and T. Tritt, *Applied Physics A*, 2009, **94**, 231–234.
- 14 S. LeBlanc, *Sustainable Materials and Technologies*, 2014, **1-2**, 26–35.
- 15 T. Holgate, L. Han, N. Wu, E. Bojesen, M. Christensen, B. Iversen, N. Nong and N. Pryds, *Journal of Alloys and Compounds*, 2014, **585**, 827–833.

4 Conclusions

The presented studies range from solid state chemistry to fabrication engineering. In terms of thermoelectric material research high-conversion efficiency and high-power materials have to be regarded separately. The postulations worked out by Dario Narducci [14] were confirmed. The role of the thermal conductivity has to be set in a new light. The thermoelectric community is engaged to increase the figure of merit ZT and therefore the thermoelectric conversion efficiency of novel materials. Usually, it is attempt to minimize the thermal conductivity in order to reach higher ZT -values. But, considering infinite heat sources, the electric power output of a certain thermoelectric generator can be increased by decreasing the conversion efficiency. Instead of ZT , the power factor has to be maximized and the heat conductivity has to be adjusted at an optimized value. With such approaches in material creation a larger amount of electrical power can be harvested at lower conversion efficiency. Furthermore, composite materials were synthesised as a method alternative to doping. The theoretical description of thermoelectric composite properties were carried out. The equation contain the single-phase thermoelectric properties and the composite property concerning the percolation network.

The commercially available Bi-Sb-Te-based materials exhibit the best conversion efficiency but the electric output-power is limited by the low thermal conductivity. Furthermore, these telluride-materials are expensive and exhibit a low chemical and thermal stability at intermediate temperatures ($T > 500$ K). Metallic alloys and ceramic materials show advantageous properties for thermoelectric energy conversion at higher temperatures. But, also for temperatures around room-temperature, materials alternative to the expensive Bi-Sb-Te-compounds should be applied and improved. In general, the thermal conductivity of composite materials is expected to decrease compared to the single-phase materials. But the thermal transport properties have to be determined for each novel material.

I expect that the role of the thermal conductivity in the framework of thermoelectric materials will be set in a new light. The parameters to be adjusted depend on the intended application related to the temperature conditions at the place of installation.

The system research concerning entire thermoelectric devices revealed, that the major concern is contacting the thermoelectric materials electrically. Even if the single-phase properties are known, the created contacts show unidentified properties that have to be determined for each system. To decrease parasitic losses at the interfaces various electric connector material (Au paste, Sn-Pb solder and epoxy-based Ag-adhesive) were tested in terms of electrical and mechanical contact properties. The devices were constructed in the commonly used rigid chess-board design and as flex-

ible stripe-TEGs. For upscaling such devices, the flexible (coilable) system is seen as better design. Using oxide-materials as thermoelectrically active legs, the construction of generators for application in the high-temperature range ($T > 500$ K) is possible. The application of TEGs at high-temperatures is advantageous because of the increasing Carnot efficiency with increasing temperature. In general, the design of the generator exhibit a rigid form for high-temperature application due the thermal lability of flexible substrate materials.

For deep insights into the solid state physical transport in each material of the entire generator system, finite-element simulations were performed. That kind of simulation can identify the quantity of electric contact resistances, which are a major concern of entire thermoelectric system. To decrease the electrical contact resistances at the material boundaries inside a thermoelectric generator, the connector material as well as the thermoelectric materials have to be regarded. For the flexible TEGs, the contact resistances were heavily decreased by the additional Ag-phase inside the cobaltite matrix of the p-type material. The combination of Ag-containing p-type ceramic-based composite materials and the Ag-epoxy resin as electric connector exhibit very low resistivities of the entire TEGs. Hence, the available electric current can be increased by implementing the Ag-containing composite instead of the pure $\text{Ca}_3\text{Co}_4\text{O}_9$ material, though the generated electric potential decreases.

In my opinion, the supply of thermoelectric devices will be increased in the future. For local low-power energy conversion TEGs will be more suitable and can complement the market of decentralized electrical power supply, that is nowadays governed by photovoltaic devices.

Publications and Conferences

Publications included in this work (chronological order)

(1) Finite-Element Simulations of a Thermoelectric Generator and Their Experimental Validation

Benjamin Geppert, Dennis Groeneveld, Vera Loboda, Alexander Korotkov and Armin Feldhoff

Energy Harvesting and Systems, 2(1), 95-104, (2015)

(2) An Approach to a Flexible Thermoelectric Generator Fabricated using Bulk Materials

Benjamin Geppert and Armin Feldhoff

Energy Harvesting and Systems, 3(2), 161-171, (2015)

(3) Oxide-Based Thermoelectric Generator for High-Temperature Application Using p-Type $\text{Ca}_3\text{Co}_4\text{O}_9$ and n-Type $\text{Ca}_3\text{Co}_4\text{O}_9$ $\text{In}_{1.95}\text{Sn}_{0.05}\text{O}_3$ Legs

Michael Bittner, Benjamin Geppert, Nikola Kanas, Sathya Prakash Singh, Kjell Wiik and Armin Feldhoff

Energy Harvesting and Systems, 3(3), 213-222, (2016)

(4) Experimental and Theoretical Thermoelectric Investigations of n-Type Composite Oxide Materials

Benjamin Geppert and Armin Feldhoff

Journal of Electroceramics, (submitted 2016)

(5) Enhanced Flexible Thermoelectric Generators Based on Oxide-Metal Composite Materials

Benjamin Geppert, Artur Brittner, Lailah Helmich, Michael Bittner and Armin Feldhoff

Journal of Electronic Materials, (revised 2016)

(6) Experimental Characterisation and Finite-Element Simulations of a Thermoelectric Generator with Ceramic p-Type $\text{Ca}_3\text{Co}_4\text{O}_9$ and Metallic n-Type $\text{Cu}_{0.57}\text{Ni}_{0.42}\text{Mn}_{0.01}$ Legs

Benjamin Geppert, Dennis Groeneveld, Michael Bittner and Armin Feldhoff
Energy Harvesting and Systems, (submitted 2016)

Publications not included in this work

(7) A High-Temperature Thermoelectric Generator Based on Oxides

Armin Feldhoff, Benjamin Geppert
Energy Harvesting and Systems, 1(1-2), 69-78, (2014)

(8) Erratum to EHS 1 (1-2), 69-78 (2014), A High-Temperature Thermoelectric Generator Based on Oxides

Armin Feldhoff, Benjamin Geppert
Energy Harvesting and Systems, 1(3-4), 251, (2014)

(9) Inverted Fuel Cell: Room-Temperature Hydrogen Separation from an Exhaust Gas by Using a Commercial Short-Circuited PEM Fuel Cell without Applying any Electrical Voltage

Sebastian Friebe, Benjamin Geppert, Jürgen Caro
Angewandte Chemie, 54, 7790-7794, (2015)

(10) Effect of the B-Site Composition on the Oxygen Permeability and the CO_2 Stability of $\text{Pr}_{0.6}\text{Sr}_{0.4}\text{Co}_x\text{Fe}_{1-x}\text{O}_{3-\delta}$ ($0.0 \leq x \leq 1.0$) Membranes

Kaveh Partovi, Benjamin Geppert, Fangyi Liang, Claus H. Rüschler and Jürgen Caro
Chemistry of Materials, 27, 2911-2919, (2015)

Contributions to conferences

- (1) Oxide based thermoelectric high-temperature energy harvester

Benjamin Geppert and Armin Feldhoff

12th European Conference on Thermoelectrics (ECT), Bucharest (Romania), 16th-20th June (**2014**) (Talk)

- (2) Thermoelectric high-temperature energy harvester based on oxides

Armin Feldhoff and Benjamin Geppert

33th International Conference on Thermoelectrics (ICT), Nashville (USA), 16th-20th June (**2014**) (Poster)

- (3) Thermoelectric oxides for thermoelectric high-temperature energy harvesting

Armin Feldhoff, Olga Ravkina and Benjamin Geppert

33th International Conference on Thermoelectrics (ICT), Nashville (USA), 16th-20th June (**2014**) (Poster)

- (4) Thermoelectric generator for high-temperature application made from oxide ceramics

Armin Feldhoff and Benjamin Geppert

14th International Conference of European Ceramic Society (ECerS), Toledo (Spain), 21th-25th June (**2015**) (Talk)

- (5) A flexible thermoelectric generator fabricated using bulk materials

Benjamin Geppert and Armin Feldhoff

1st Workshop Energy Harvesting and Systems - FlexTEG 2015, Fraunhofer IWS Dresden (Germany), 25th-26th June (**2015**) (Talk)

- (6) Finite-element simulations of a thermoelectric generator and their experimental validation

Benjamin Geppert, Dennis Groeneveld and Armin Feldhoff

34th International Conference on Thermoelectrics (ICT) and 13th European Conference on Thermoelectrics (ECT), Dresden (Germany), 28th-2nd June-July (**2015**) (Talk)

(7) Nanostructured oxide thermoelectrics for high-temperature energy harvesting

Armin Feldhoff, Benjamin Geppert and Michael Bittner

Microscopy Conference - German Society for Electron Microscopy, Göttingen (Germany), 6th-11th September (**2015**) (Poster)

(8) Experimental and theoretical thermoelectric investigations of n-type composite materials

Benjamin Geppert and Armin Feldhoff

91st DKG Annual Conference & Symposium on High-Performance Ceramics, TU Bergakademie Freiberg (Germany), 7th-9th March (**2016**) (Talk)

(9) Flexible thermoelectric generator fabricated using bulk materials

Armin Feldhoff, Artur Brittner, Lailah Helmich, Michael Bittner and Benjamin Geppert

14th European Conference on Thermoelectrics (ECT), Lisbon (Portugal), 20th-23th September (**2016**) (Poster)

(10) Application of thermoelectric materials in flexible thermoelectric generator

Armin Feldhoff, Artur Brittner, Lailah Helmich, Michael Bittner and Benjamin Geppert

2nd Workshop Energy Harvesting Systems - FlexTEG, Fraunhofer IWS Dresden (Germany), 26th-27th September (**2016**) (Talk and Poster)